4 STORAGE RING SYSTEM

4.1 Storage Ring Magnets

4.1.1 Parameters and Tolerances

The DBA lattice (30 cells with a super periodicity of 15) consists of 60 dipole magnets with uniform magnetic field and a maximum field of 4 kiloGauss at 3.0 GeV. The ring quadrupoles consist of a total of 300 magnets with two different lengths: 25 and 40 cm. These quadrupoles have a maximum gradient strength of 22 T/m at 3.0 GeV. The quadrupoles are individually powered, but the current lattice design assumes eight families. There are also 300 sextupoles magnets with two different lengths: 20 and 25 cm. These magnets, together with the correction magnets and BPMs, are listed in Section 6.1.1 and in Table 6.1.4.

4.1.2 Preliminary Magnet Design

4.1.2.1 Storage Ring Lattice Magnet Considerations

The magnet lattice is designed with a 30-cell DBA (double bend achromat) structure for a machine with 3.0 GeV full-energy top-off injection. The 792 m storage ring will contain more than 900 magnets. This quantity is comprised of 60 bending dipoles, 300 quadrupoles, 300 sextupole magnets, and 242 corrector magnets. To ensure acceptable dynamic aperture for the electron beam, the required magnetic field quality and alignment tolerances are the two primary considerations in the design. All the dipole magnets are connected in series and are energized by a single power supply. Individual trim power supplies will be used to provide ±3% field adjustment. All quadrupoles will be individually powered and the sextupoles will be powered in nine families. Properties of the storage ring magnets are summarized in Table 4.1.1.

Table 4.1.1 Storage Ring Magnet Specifications at 3.0 GeV.

	Dipole					ID
	35 mm	90 mm	Quadrupole	Sextupole	Corrector	Corrector
Bending angle [deg]	6	6	0	0	±0.08	±0.01
Max. Clear bore aperture [mm]	35	90	66	68	150/100	35/80
Max. Dipole field [T]	0.4	0.4	0	0	0.04	**0.01
Field gradient [T/m]	0	0	22	0	*0.36	0
Max. Sextupole field [T/m^2]	0	0	0	500	0	0
Field quality in GFR - 20 x 40 [mm]	$1x10^{-4}$	$1x10^{-4}$	$2x10^{-4}$	$5x10^{-4}$	$1x10^{-3}$	$1x10^{-2}$
Nominal operating current [A]	360	360	108	190	20	20
Cooling type	water	water	water	water	air	air
Maximum temperature rise [°C]	10	10	10	10	20	20

*Skew quadrupole component, 30 each required

** at 100 Hz

In this section, we present designs of the individual magnets. Optimization and refinements will occur during the next phase of detailed design.

The following paragraphs in this section present a partial list of lattice magnet design considerations. For the preliminary design, these considerations are global in nature and will evolve into specific design parameters for the next phase of "reference" design.

- The average current density in the coil cross-section of the storage ring magnets was selected to be less than or equal to 2 A/mm^2, with typical current densities in the copper conductor of 3.5 to 4.5 A/mm^2.
- The temperature rise of cooling water across any magnet coil will be limited to about 10ºC, with a pressure drop across each magnet of less than 4 bar.
- The magnetic alignment requirements of the multipoles exceed tolerances achievable by the normal optical survey method. Therefore, these magnets are aligned magnetically and then fixed to a rigid girder for installation in the storage ring tunnel.
- The storage ring magnet reference designs are being developed to minimize fabrication costs, provide high operational reliability, and minimize the power consumption by individual components as well as overall magnet systems.
- The magnet supports are designed so as to reduce vibration amplification by maintaining the resonance frequency of the multipole support assembly above that of the girder.
- The reference design will address a low-cost yet reliable means to integrate the multipole magnets into a vibrating wire magnet-to-magnet alignment system and a means to transfer magnetic field center locations precisely to survey targets on the magnet girder.
- Handling and rigging safety issues for magnet testing and installation will be addressed, and the reference design will comply with BNL's Critical Lift Policy.
- Electrical and all other safety issues will be addressed in the next phase of detailed design. The design of the magnets, the power cabling, and the water cooling from the magnet-to-cable connections on the girders, as well as magnet instrumentation and controls, will be fully NEC and OSHA compliant.
- Magnetic lengths were optimized and drift space between the multipoles was increased to accommodate beam position monitors (BPMs) and corrector magnets without altering the lattice.
- Electrical, magnetic, and mechanical design optimization will be performed for the reference design of the relatively low-field-strength 0.4 T dipole magnet to assure high field quality requirements for the C-type magnet cross-section.
- Extensive 3D modeling and value engineering optimization is being performed for both the 22 T/m maximum quadrupole strength and the 500 T/m^2 maximum sextupole strength. The goals are to 1) assure high field quality and extremely critical alignment requirements for both multipoles, 2) accommodate the synchrotron's x-ray extraction lines and the vacuum chamber, and 3) minimize or eliminate the effects of crosstalk between neighboring magnets and correctors.

These preliminary designs and considerations will be refined by both the Laboratory and Industrial resources during the next phase of design, resulting in a "reference" design. The final magnet design will be developed by the magnet manufacturer, and reviewed and approved by the Laboratory prior to production. Extensive 2D and 3D magnetic modeling, mechanical design, and fabrication and assembly methods have been studied, resulting in the preliminary magnet designs that are described in the following sections.

4.1.2.2 Dipole Magnet Preliminary Design

4.1.2.2.1 Scope and Physics Design Parameters

A unique attribute of NSLS-II is the use of dipole magnets with apertures of two different sizes. This requirement is necessary to accommodate a significant and growing community of users who require lower

energy infrared and THz radiation. To serve this important community, a 90 mm aperture concept has been chosen, to allow the extraction of long-wavelength light from the dipole magnet [4.1.1, 4.1.2].

The NSLS-II storage ring will be equipped with six dipole magnets that have a gap of 90 mm, and 54 dipoles that have a gap of 35 mm. Each dipole will have a magnetic length of 2.62 m with a field 0.4 T at an electron energy of 3.0 GeV. The radius of curvature of the bending magnet is 25 m; it bends the electron beam 6.0° with a sagitta of 35 mm. The dipole magnets are C-type with a curved laminated flux return yoke (Figure 4.1.2).

A new extended pole ("nose") design (Figure 4.1.3) releases a significant amount of physical space (~190 mm per magnet) and minimizes the challenges associated with a tight lattice. In most iron-dominated magnets, the magnetic length is larger than the yoke length but smaller than the coil length. The proposed NSLS-II design takes advantage of the fact that the nominal operating field of 0.4 Tesla is well below iron saturation. This allows the axial length of the iron pole to become as long as the coil length, thus making the magnetic length longer than the coil length. The proposed design makes the magnetic length larger than both the yoke length and the magnet mechanical length (including ends of the coil). The width of the iron pole is 100 mm.

Calculations of the magnetic field were made to optimize the pole contours and the quality of the magnetic field, which for a dipole magnet must have field non-homogeneity of $\Delta B/B \leq \pm 0.01\%$ over a good-field region of 40 x 20 mm (Figure 4.1.2). All computed field harmonics in the entire range of operation (up to 0.48 T) are well below one part in 10^4 at 10 mm radius.

Investigations of beam dynamics have established that the good-field region accommodates the dynamic aperture. A list of the preliminary design dipole parameters is found in Table 4.1.2.

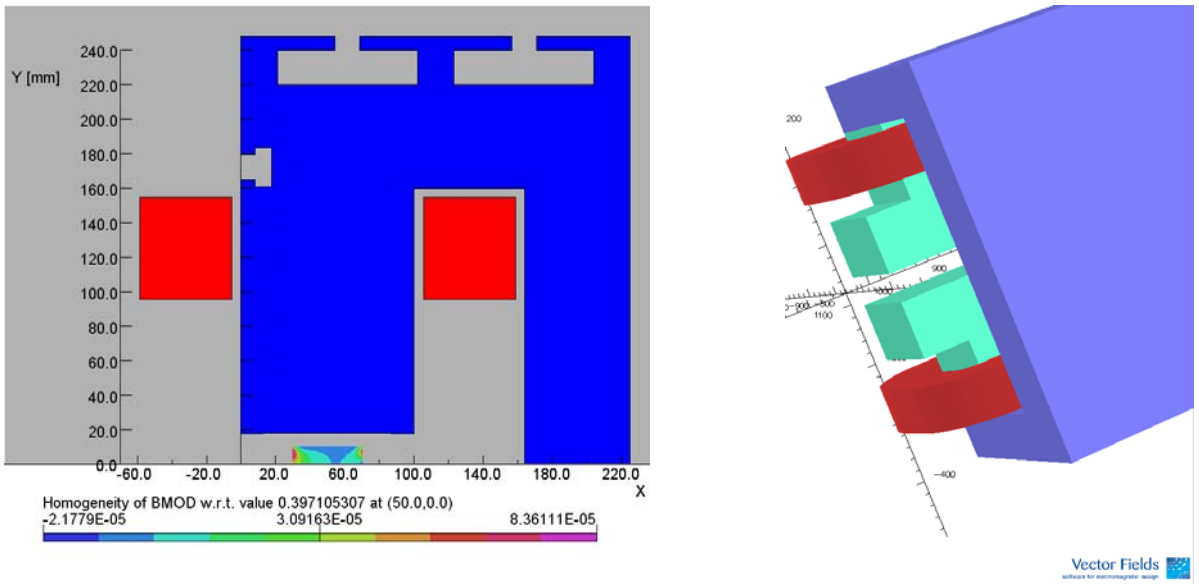

Figure 4.1.2 Magnetic model of the Ring Dipole. 2D model with relative field errors in good field aperture is shown on the left and 3D model with extended pole (nose) on the right. The proposed design makes the magnetic length of the magnet longer than the mechanical length (including coil ends), and frees significant space in a tight lattice.

The storage ring dipoles are designed so that both aperture magnets may be connected in series with a single power supply. Implementation of Decker distortion and minor differences between the two aperture magnets shall be corrected by independently powered trim coils located on each dipole The six large aperture

dipoles will be installed into the storage ring in pairs. Each pair shall comprise the adjacent bending magnets in a single cell, and there will be three cells equally distributed around the storage ring.

Table 4.1.2 Dipole Magnet Preliminary Baseline Design Parameters.

	35 mm Storage Ring Dipole	90 mm Storage Ring Dipole
Energy [GeV]	3.0	3.0
Bending angle [deg]	6	6
Clear bore aperture [mm]	35	90
Dipole field [T]	0.4	0.4
Field quality	$1x10^{-4}$	$1x10^{-4}$
Good-field region [mm]	40 x 20	40 x 20
Magnetic length [mm]	2,620	2,620
Nominal operating current [A]	360	360
Number of Ampere-turns	11,520	30,240
Number of turns / magnet	32	84
Total Inductance of the magnet [mH]	16	116
Current density in conductor [A/mm^2]	3.7	3.7
Max. temperature rise [°C]	10	10
Max. pressure drop [bar]	4.0	4.0
Voltage/magnet	11.4	32
Nom. power per magnet [kW]	4.2	11.5
Iron length Extended Pole/Return Yoke [mm]	2,585/2,415	2,530
Lamination thickness [mm]	1.5	1.5

4.1.2.2.2 Mechanical Design of the Dipole

Fabrication and assembly concepts have been studied, resulting in the preliminary magnet designs that are shown in Figures 4.1.3 and 4.1.4. The laminated magnet yokes are composed of 1.5 mm-thick dry film epoxy-coated AISI 1006 low-carbon steel sheet. The permeability of the core material deviates by about 5% from the production value. The laminations must be shuffled to ensure a uniform magnetic property. The 35 mm dipole will have a self-supporting yoke assembly.

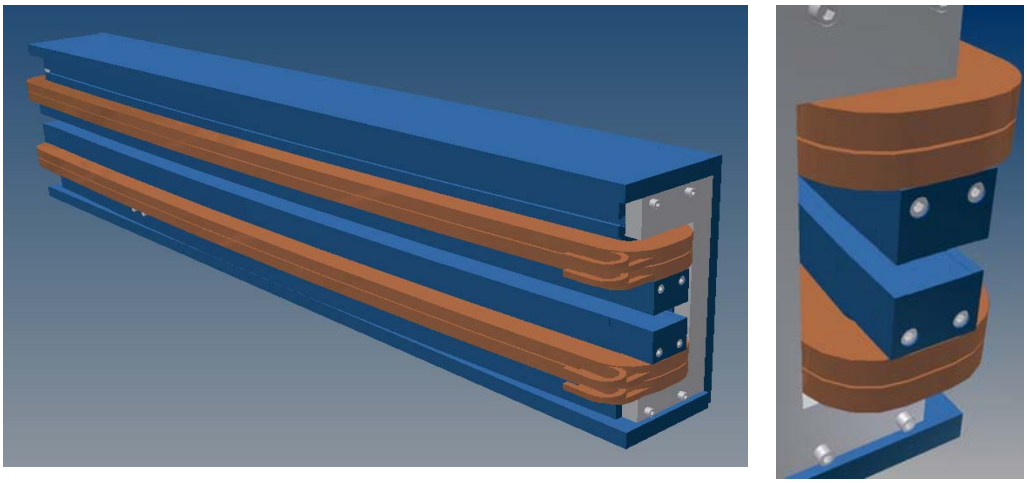

Figure 4.1.3 Views of the 35 mm storage ring dipole , with close-up of novel nose ends pinned and bolted in place.

A precision stacking fixture will be used to register all the laminations to the magnet gap. The base of the fixture will be curved to generate the 25 m nominal core radius. The dipole laminations will be stacked in parallel, and straight tie bars will be inserted through clearance slots in the laminations. Prefabricated end packs will be added to either end of the yoke assembly. The tie bars are tensioned and the yoke assembly is cured. Straight steel stiffening plates are bolted together around the top, bottom, and back of the curved laminated core. The stiffener plates are then welded to the core to form a rigid yoke assembly. The dipole end packs will be tapped and pinned in preparation for adding the nose piece.

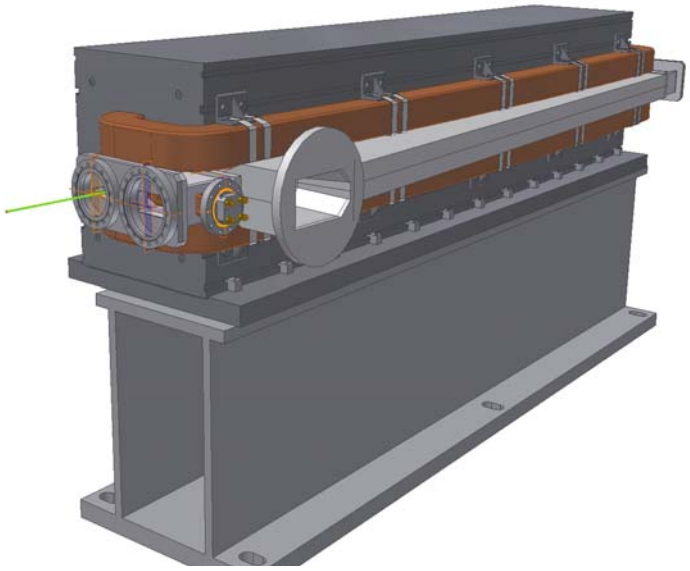

Figure 4.1.4 The 90 mm aperture dipole design concept with an IR beam extraction vacuum chamber installed.

The coils for the 35 mm dipoles are made up of square hollow copper conductors, 13 x 13 mm, with an interior diameter of 9 mm. The coils for the 90 mm dipoles are made of the same rectangular hollow copper conductors. The water channels of the hollow conductor coil "pancakes" are connected in parallel to provide cooling adequate to restrict the increase in coil temperature to less than 10°C, and in the case of the 90 mm dipoles, to reduce pressure drop in the seven-turn, six-layer coils.

Fiberglass that is vacuum impregnated with highly radiation-resistant epoxy greater than 1.0 mm thick will provide interstitial conductor insulation. An additional 1.5 mm (minimum) of vacuum-impregnated epoxy fiberglass will provide ground plane insulation. The magnet will be high-potted up to 5 kV to detect defects in the insulation.

After the coils are assembled through the gap of the 35 mm dipole and secured, the core's nose pieces will be precisely pinned and bolted to the laminated end packs at either end of the dipole yoke assemble. The nose pieces shape the dipole end fields to minimize end-field errors and to match the field profiles of the 90 mm dipole.

Dipoles of either aperture that are not used as IR sources will use a single dipole vacuum chamber design. The chamber will allow damping wiggler radiation to pass through. The larger aperture IR dipole vacuum chamber will have a minimum internal aperture of 70 mm.

The designed magnet cross-section will accommodate the vacuum chamber with a 2 mm clearance between the magnetic poles and either side of the vacuum chamber.

4.1.2.3 Quadrupole Magnet Preliminary Design

4.1.2.3.1 Scope and Physics Design Parameters

Within the 66 mm aperture of the storage ring quadrupole magnet, the field gradient homogeneity in a region 40 x 20 mm is required to be better than 0.02%. The design geometry of the quadrupole is highly constrained by several factors:

1. Field quality and magnet alignment requirements as shown in Table 4.1.3
2. The geometry of the multipole vacuum chamber, and the need to accommodate its antechamber
3. The requirement to produce a low-cost magnet with very high reliability

To provide a path for synchrotron radiation exiting insertion devices, the antechamber and extraction ports must extend beyond the horizontal mid-plane of the magnet yoke. To assure symmetry, the horizontal back leg on either side of the quadrupole has been removed to accommodate the antechamber of the vacuum chamber. Therefore, the top and bottom halves of the quadrupole are not connected with a flux-return yoke; each half is connected mechanically with nonmagnetic metallic spacers that accommodate that vacuum chamber. This figure-8 style quadrupole has been known [4.1.3] and used successfully in previous machines, such as APS and SPEAR-3; cost savings are inherent in the design.

The quality of the field gradient in the full magnet aperture has been examined through 2D and 3D modeling using the OPERA code. The poles, shims, and end chambers are optimized to produce a quadrupole field with higher order systematic multipole components that meet the requirements shown in Table 6.1.9. Further modeling will be performed to assess the effects of value engineering and structural design optimization. R&D prototype magnets will be fabricated and magnetic measurements performed, to assess the effects of fabrication errors that contribute to random and additional systematic high-order multipoles. To assure that the total multipole harmonic content of the as-built reference design will meet the requirements of Table 6.1.9, magnet pole end chamfers are being modeled and actual optimization will be performed with the prototype quadrupole laminated end packs. Table 4.1.3 lists the preliminary design parameters.

Table 4.1.3 Quadrupole Magnet Preliminary Design Parameters.

	25cm SR Quadrupole	40cm SR Quadrupole
Energy [GeV]	3.0	3.0
Clear bore aperture [mm]	55	55
Maximum field gradient at 3.0 GeV [T/m]	12.8 / 8.3	22
Field quality	2×10^{-4}	2×10^{-4}
Good field region [mm]	40 x 20	40 x 20
Magnetic length [mm]	300	400
Nominal operating current [A]	95/ 146	160
Max. Number of Ampere-turns/pole	3686 / 5778	11520
Number of turns / magnet pole	39	72
Total resistance of the magnet at 30°C [Ω]	0.0529	0.129
Total inductance of the magnet [mH]	27	135
Max. Current density in conductor [A/mm^2]	4.2	4.6
Number of parallel cooling circuits	4	4
Temperature rise [°C]	7	10
Pressure drop [bar]	4	4
Voltage / magnet [V]	5 / 7.7	19.8
Iron core length [mm]	217	367
Lamination thickness [mm]	1.5	1.5
Quadrupole alignment tolerance [μm]	30	30

3-D OPERA code modeling of the figure-8 quadrupole with chamfering of the laminated end packs is shown in Figure 4.1.5. Further modeling will ensure that the requirements for higher-order multipoles (Table 6.1.9) are met.

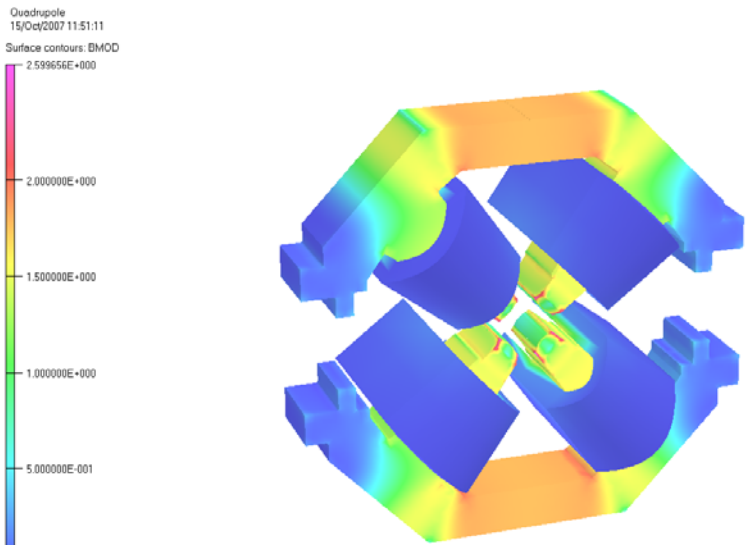

Figure 4.1.5 OPERA model of an NSLS-II storage ring quadrupole magnet cross-section, for studying the effects of pole edge chamfering.

4.1.2.3.2 Mechanical Design of the Quadrupole

Both halves of laminated iron yokes are composed of a single stamped and fine blanking lamination. The laminated magnet cores are made of low-carbon AISI 1006 steel sheet, 1.5 mm thick. A thin film of "B" staged (dry) heat-activated epoxy is applied to the lamination steel before blanking. The yoke is designed to allow the laminations to be shuffled.

End packs each having 12 laminations epoxied together are made using the Quadrupole yoke stacking fixture. The end pack stacking fixture is placed into an oven and heated until the lamination is full cured. Chamfers are precisely machined into the poles of these end packs.

The body of the quadrupole yokes are assembled using the same stacking fixture in shuffled packs about 18 mm thick. The packs are stacked with every other pack flipped in the stacking fixture. The chamfered end packs are secured to either end the center yoke section. While they are in the stacking fixture, a TIG weld bead is added to the outside of the iron to fix the packs together. The stacking fixture is compressed to a stop and heated until the epoxy between the laminations is fully cured.

The coils are wound on custom winding mandrills. Each coil has two layers of windings. For the majority of the quadrupoles, a single coil per pole is required. The conductor is a hollow square copper conductor 7.0 x 7.0 mm with a 4 mm diameter water channel and is wrapped with fiberglass.

The coil is wound in a manner that the first turn starts near the center of the length of conductor that is being wound. All NSLS-II coils are free from internal splices.

Vacuum impregnation is performed using an alumina-filled, high-radiation-resistant epoxy with a minimum thickness of 1.0 mm to provide interstitial conductor insulation. An additional 1.5 mm of alumina-filled epoxy fiberglass is applied to the outside of the coil to provide coil-to-ground plane insulation. The magnet coils will be high potted up to 5 kv to detect defects in the coil insulation system.

Value engineering of the quadrupole design to conform to lattice requirements has yielded three styles of coils. Most of the quadrupoles have four double-layer coils with four parallel water paths. Higher-field quads will have either a longer coil or additional coils per pole. Each coil shall represent an additional parallel water circuit. The increase in water temperature across any quadrupole magnet will be <1°C. Figure 4.1.6 presents the mechanical design.

The quadrupoles will be supported from near the mid-plane so thermally induced strain in the magnet's iron poles and yoke will tend to act about the magnet's axis, maintaining its pre-surveyed location to ≤10 μm over its full range of excitation. A minimum clearance of 2.0 mm is maintained between the magnet poles and vacuum chamber to effect thermal and vibrating isolation between the two devices.

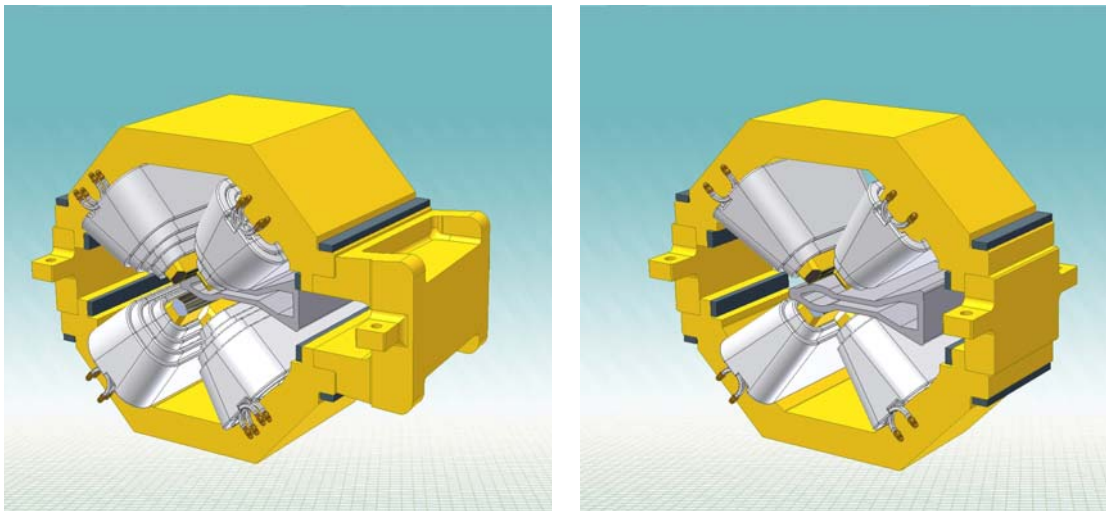

Figure 4.1.6 Preliminary designs the for NSLS-II storage ring quadrupole magnet. **Left**: A high-field quadrupole with an antechamber clearance. **Right**: a symmetric low-to-moderate field quadrupole.

4.1.2.4 Sextupole Magnet Preliminary Design

4.1.2.4.1 Scope and Physics Design Parameters

The storage ring is equipped with 300 sextupole magnets. The sextupole field homogeneity in a region 40 mm x 20 mm is required to be better than 0.05%. The geometry of the vacuum chamber determines the bore radius of the sextupole magnet. The design of the sextupole magnet is constrained by the need to accommodate a vacuum chamber's antechamber.

The poles and shims are optimized with a 2D approximation. Additional 3D modeling was performed to ensure that the requirements for higher-order multipoles (Table 6.1.9) are met.

The field quality is optimized for standard and extended sextupole models (Figure 4.1.7). The field quality is consistent with the specified sextupole field throughout the required transverse region, and all harmonics below two parts in 10^4 at 45 mm reference radius, in the entire range of operation. The bore diameter of 68 mm was determined by specifications of field quality and the spatial constraint between the vacuum chamber and the poles and coil geometry. The base of the pole is widened to prevent saturation in that area at high field excitations. In a wide-aperture sextupole, the ideal symmetry is partially broken due to nonperfect return yoke geometry, and semi-allowed harmonics (b_0, b_5, b_7, etc.) are created. We have developed a new design method that minimizes these harmonics by moving up the pole located at 90 degrees by about ~35 microns. Table 4.1.4 lists the preliminary design parameters for the sextupole magnets.

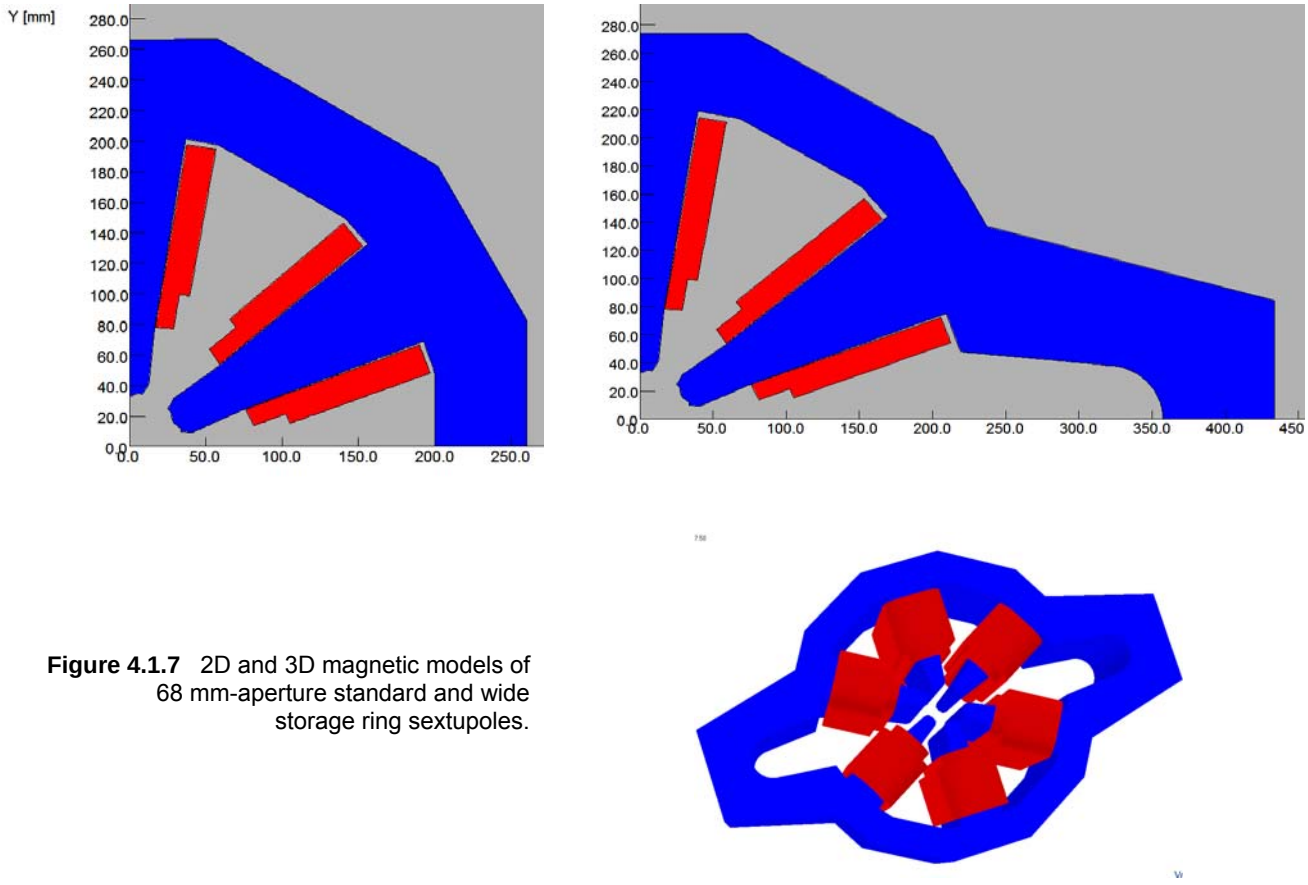

Figure 4.1.7 2D and 3D magnetic models of 68 mm-aperture standard and wide storage ring sextupoles.

Table 4.1.4 Sextupole Magnet Preliminary Design Parameters.

	20cm Sextupole	25cm Sextupole
Clear bore aperture [mm]	68	68
Sextupole field [T/m^2]	300 / 400	400
Field quality	5 x 10^{-4}	5 x 10^{-4}
Good-field region [mm]	40 x 20	40 x 20
Magnetic length[mm]	200	250
Maximum operating current [A]	123 / 164	164
Max. Number of Ampere-turns/pole	3192 / 4255	4255
Number of turns / pole	26	26
Total resistance of the magnet at 30°C [Ω]	0.0293	0.0346
Total inductance of the magnet [mH]	8.8	11.0
Temperature rise [°C]	7.5	5.1
Pressure drop [bar]	4	4
Voltage / magnet	3.3 / 4.4	5.2
Iron length [mm]	179	228
Laminae thickness [mm]	1.5	1.5
Sextupole alignment tolerance [μm]	30	30

4.1.2.4.2 Mechanical Design of the Sextupole

The sextupole magnets for the storage ring come in two lengths. Most of the sextupoles have a magnetic length of 0.2 m. The mid-cell sextupole has a magnetic length of 0.25 m.

To maintain high field quality, minimize random errors, assure the long-term mechanical stability, and not eliminate the possibility of adding steering and skew quadrupole trims in the future, the mechanical design is based on a mid-plane parting surface. To perform magnet assembly, it was determined that a removable 90-degree center pole in each magnet half is feasible (Figure 4.1.8).

A minimum clearance of >1.5 mm between the vacuum chamber and adjacent poles to maintain thermal and vibration isolation is maintained. The magnet cores are made from AISI 1006 low-carbon steel sheet. The laminations are coated with a thin film of "B" staged (dry) heat-activated epoxy. The yoke is designed to allow shuffling of laminations. The shuffled laminations are assembled in packs of ten laminations. Precision stacking fixtures are used to fabricate a series of end packs for both the two pole yoke and center-pole yoke subassemblies. After the end packs are oven cured, pin holes and chamfers are precisely machined into the pole tips. The body of the sextupole is composed of packs of shuffled laminations cured together inside a precision stacking fixture. The machined end packs are added to the mid yoke blocks in the stacking fixture. While in the stacking fixture, Tig weld beads are added to the yoke to secure the relative position of the packs.

Coils are composed of a double-layer stack of square copper conductor, 8.5 x 8.5 mm, with a 4.5 mm diameter water channel. The conductor is insulated with fiberglass. The coil is wound so the first turn starts the coil near the center of the length of conductor being wound. Vacuum impregnation is performed using alumina-filled high-radiation-resistant epoxy with a minimum interstitial conductor thickness of 1.0 mm. An additional 1.5 mm of alumina-filled fiberglass epoxy forms the ground plane insulation. The coils are high potted to 5 kv to detect defects in the insulation system. A coil center-pole subassembly is produced. A coil secured to the center-pole assembly is assembled in the yoke stacking fixture. Precision yoke end rings are assembled at either end of the sextupole core halves, and stainless steel rods with threaded ends are used to compress the yoke and end rings to precisely control yoke geometry. The end rings are used to position the center-pole relative to the two adjacent poles.

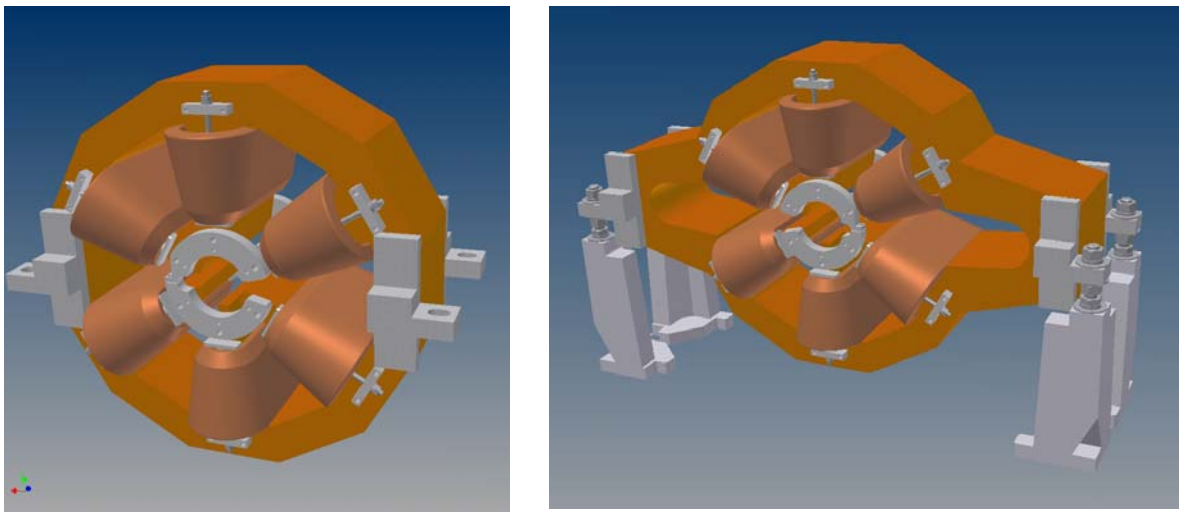

Figure 4.1.8 Preliminary design of 68 mm aperture standard and wide storage ring sextupoles.

Brackets are pinned and bolted to the yoke back legs at the mid-plane, the yokes are assembled, and the end rings are used to locate the two halves of the poles about a common center. Studs are used in the brackets to secure the core halves together. At least three parallel water circuits are used to maintain ≤10°C temperature rise in the cooling water across the magnet.

4.1.2.5 Correction Magnet Preliminary Design

In addition to the primary lattice magnets, the NSLS-II storage ring has corrector magnets. The correctors will be used to adjust the beam orbit and to correct for alignment errors. The correctors will also be used as part of both global and local feedback systems. The preliminary design calls for 242 correctors to be installed at the start of operation. Unlike other light sources where steering correction can be integrated into combined-function lattice sextupoles, the precise alignment and field quality requirements of the NSLS-II sextupoles largely prevent the use of combined-function sextupoles, making discrete correctors necessary.

There will be three types of corrector magnets. One type of global corrector will produce vertical and horizontal DC steering fields of up to 320 Gauss for ±0.8 mrad vertical and horizontal steering of the 3.0 GeV electron beam. There will be 120 of these correctors located around the stainless steel bellows assemblies at either end of the lattice dipole magnets. These correctors will produce an oscillating field component from DC to less than 100 Hz for up to ±0.1 mrad of vertical and horizontal dynamic steering. Another type of corrector, of similar design but with a smaller aperture, will be located around the aluminum vacuum chamber. A minimum of 60 of these correctors will produce both DC and an oscillating field component of greater than 5 Hz. The maximum operational frequency of these correctors will be determined as part of the NSLS-II R&D program, as we study and optimize the correctors' field interaction with the aluminum vacuum chamber. Thirty of these correctors will possess skew quadrupole windings to deliver a maximum DC field gradient of 0.36 T/m. 2D and 3D modeling studies of these correctors have been performed (Figure 4.1.9).

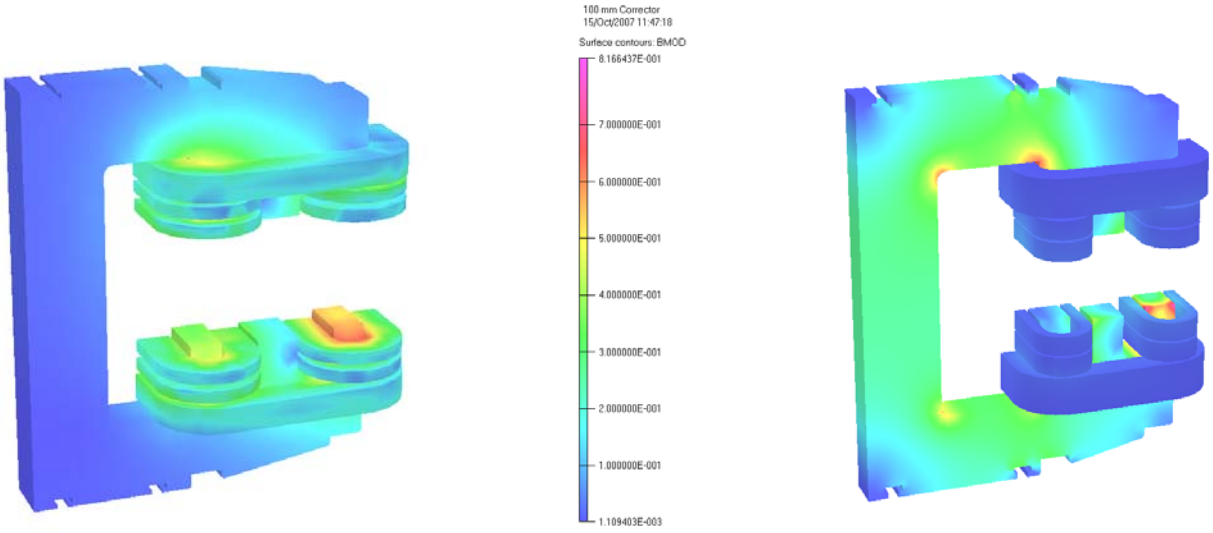

Figure 4.1.9 OPERA models of NSLS-II storage ring corrector magnets.
Left: Fast 156 mm aperture corrector. **Right**: Slow 100 mm aperture corrector.

A third type will be fast correctors, which will provide a maximum field of 100 Gauss at a frequency up to or exceeding 100 Hz. Twenty fast correctors will be used for local feedback. They will be located around stainless steel bellows or sections of stainless steel vacuum chamber at either end of an insertion device, such as an undulator. Silicon steel laminations 0.5 mm thick were selected for use in the corrector magnet flux return, to suit the charging rate. Table 4.1.5 lists the preliminary design parameters for the corrector magnets.

Many factors must be considered in the corrector magnet design. The design of a corrector magnet will be specific to its required function, the space constraints of the specific locations in the lattice, and how the corrector accommodates and interacts with the vacuum chamber design at its required location. Design options such as APS-style correctors are compact in size but tend to be rich in harmonics. Box-style correctors around the vacuum chamber have good field quality but tend not to use available space as efficiently and have larger stray fields. Analytical modeling of the C-shaped correctors revealed viable solutions for each corrector location.

Table 4.1.5 Corrector Magnet Preliminary Design Parameters.

	Fast Corrector	Slow Corrector	ID Corrector
Aperture [mm]	156	100	35/80
magnetic length [mm]	300	200	60/105
Iron core length [mm]	150	100	25
Max current at 3.0GeV	15	15	2
Max. DC voltage [V]	7.1/7.3 avg.	5.1/4.4 avg.	0.8/1.6
central field [T]	.028	0.04	0.0042
Max. NI/pole	2429/4188 avg.	2292/3360 avg.	180/360
J in copper [Amps./mm^2]	.35/1.4	.5./1.5	1.3

4.1.2.5.1 Mechanical Design of the Corrector Magnets

The connector magnets are composed of $\leq$0.5 mm, track-insulated, silicon steel (M36) sheet. The laminations are stacked and glued together in a precision stacking fixture. A single C-style lamination is used to simplify the design and minimize cost. The yokes are oven cured and then the pole tips are machined to assure precise gap spacing. The mechanical design of the six-coil baseline 156 mm-aperture fast corrector and a four-coil alternative design are shown in Figure 4.1.10.

Coils are composed of solid Pyra ML-coated rectangular, solid conductors. The coils are vacuum impregnated with alumina-filled radiation-resistant epoxy. Aluminum chill plates are added between the coils. This technique is used to eliminate water-cooled conductor and the water-to-conductor electrical isolator relying on ground plane insulation to isolate the coils from the water cooling loop. The corrector produces both vertical and horizontal fields simultaneously. The vertical field (horizontal bending) is essentially air cooled, and the horizontal field is water cooled, via inter-coil chill plates. Coils are assembled onto the yoke through the core aperture. Threaded holes in the chill plates molded into the horizontal field coils are used to secure the coil package, via long screws, to brackets on the top and bottom of the magnet yokes.

The correctors come in two apertures: 156 mm and 100 mm. Screw quadrupole excitation coils with a molded-in, water-cooled chill plate can be added to the aperture of the 100 mm corrector and can be secured to the magnet aperture in a manner similar to that of the vertical and horizontal field coils. Skew quad trim coils can also be added to the sextupole at one location per superperiod.

Tee-slotted keyways in the magnet yoke are used to secure the corrector to a wedge-style spacer between it and the top of the girder.

Injection magnets such as septum and kicker magnets are discussed in Section 5.9.

References

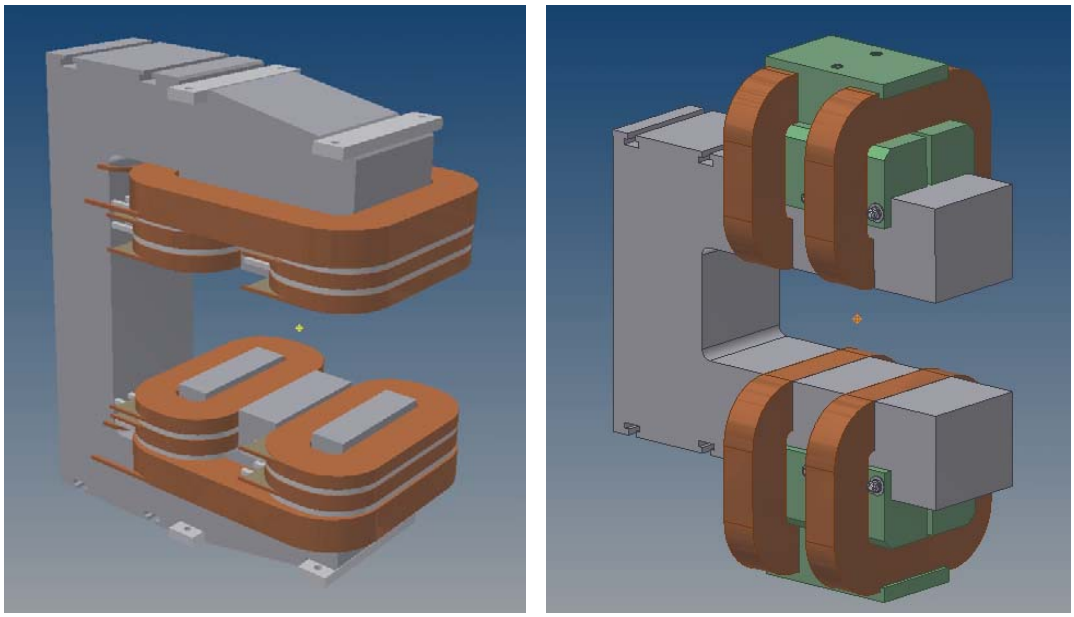

Figure 4.1.10 Preliminary designs of 156 mm aperture baseline (**left**) and alternative (**right**) corrector magnet.

[4.1.1] Creagh, D., et al., "An Infrared Beam-line at the Australian Synchrotron," SRI-2006.

[4.1.2] Katoh, M., et al., "Coherent Terahertz Radiation at UVSOR-II," SRI-2006.

[4.1.3] Danby, G.T., Jackson, J.W., IEEE Transactions in Nuclear Science, June, 1967.

4.2.3 Storage Ring Power Supplies

These power supplies are designed to stay at a fixed current except for the fast dipole correctors. The power supplies will be able to do simple ramps that will take 5 to 60 seconds from zero current to maximum current. These ramps can be software or hardware generated. The fast dipole correctors will be part of a beam-based feedback system. All power supplies will be located above the magnets in the equipment area. All power supplies will have at least a 20% margin in operating current. Listed below are the planned maximum numbers of power supplies that the storage ring will require. Some of the power supplies may have reduced quantities for day-one operation.

SR-MainDipole-PS	60 dipole magnets in a series circuit (54 small-aperture and 6 large-aperture magnets)
SR-LATrimDipole-PS	One shunt circuit to adjust current between large-aperture and small-aperture dipole magnets
SR-Quad-A-PS	150 individually powered quadrupole magnet circuits
SR-Quad-B-PS	60 individually powered quadrupole magnet circuits
SR-Quad-C-PS	90 individually powered quadrupole magnet circuits
SR-Sext-A-PS	35 pentant wide sextupole magnet circuits (7 of the 9 sextupole families)
SR-Sext-B-PS	10 pentant wide sextupole magnet circuits (2 of the 9 sextupole families)
SR-DipoleTrim-PS	60 dipole trim coil circuits – 30 planned for day-one operation
SR-SKQ-PS	30 skew quadrupole magnets circuits.
SR-BH-PS	60 intermediate speed horizontal dipole corrector magnet circuits
SR-BV-PS	60 intermediate speed vertical dipole corrector magnet circuits
SR-FGBH-PS	120 fast global horizontal correction dipole circuits
SR-FGBV-PS	120 fast global vertical correction dipole circuits
SR-FIBH-PS	120 fast insertion horizontal correction dipole circuits, 32 planned for day-one operation
SR-FIBV-PS	120 fast insertion vertical correction dipole circuits, 32 planned for day-one operation
Total slow power supplies	437 (407 planned for day-one operation)
Total intermediate-speed power supplies	120
Total fast power supplies	480 (304 planned for day-one operation)

4.2.3.1 B PS – Main Dipole Power Supply

This circuit consists of 54 small-aperture dipole magnets and 6 large-aperture dipole magnets, for a total of 60 magnets (Figure 4.2.1). The small-aperture magnets are 0.032 Ω and 16 mH. The large-aperture magnets are 0.089 Ω and 116 mH. The operating current for both magnets is ~360 A for 3.0 GeV. The cabling between magnets and the return will use 650 MCM flexible copper cables with a resistance of 0.142 Ω and inductance of 1.4 mH. The power supply load is 2.404 Ω and 1.561 H (Figure 4.2.2).

The main dipole power supply is a unipolar, two-quadrant, current-regulated supply. It will use two 12-pulse SCR converters in series with the center point connected to ground. This configuration will reduce the voltage to ground at the magnet load and reduce the voltage rating on various converter components. Each converter will have a two-stage LCRL passive filter and a series pass active filter. This is required to reduce the ripple current to low levels (Figure 4.2.2). The power supply will be able run in the invert mode while ramping down. This produces a negative voltage.

A combined digital and analog control system will control the operation of the power supply. The power supply will have a precision current regulator using a Direct Current Current Transformer as the current feedback device. The digital controls will use a feed-forward system to improve overall reproducibility. A PLC will be used for state control (on/off commands and interlocks).

The large-aperture trim dipole power supply is used to adjust the current between the large- and small-aperture dipole magnets. The purpose of the power supply is to compensate for any systematic differences between the magnetic lengths of the two different dipole magnets. The current trim is done by having a shunt circuit connected across all the large-aperture magnets (Figure 4.2.2). This power supply will be designed to float off ground. It will use the same basic controls as the quadrupole power supplies except for needed control circuit isolation.

Main Dipole Power Supply Specifications

AC input power	3-phase 460 VAC ~683 AAC
DC maximum output current – Imax	450 ADC
DC minimum output current – Imin	~1 ADC
DC output voltage	1200 VDC
operating quadrants	2: (V+, I+) & (V-, I+)
small-signal – 3 db bandwidth	500 Hz
stability (8 h–10 s) – referred to Imax	25 ppm
stability (10 s–300 ms) – referred to Imax	15 ppm
stability (300 ms–0 ms) – referred to Imax	10 ppm
absolute accuracy – referred to Imax	100 ppm
reproducability long term – referred to Imax	25 ppm
current ripple – referred to Imax	5 ppm 60 Hz and greater
resolution of reference current	18-bit ±1 LSB
resolution of current measured – fast sampling	16-bit ±1 LSB at 200 μsec
resolution of current measured – slow sampling	22-bit ±1 LSB at 16.67 msec

Large-Aperture Trim Dipole Power Supply Specifications

AC input power	3-phase 208 Vac ~ 12 AAC
DC maximum output current – Imax	13 ADC
DC minimum output current – Imin	~1 ADC
DC output voltage	300 VDC
operating quadrants	1: (V+, I+)
small-signal – 3 db bandwidth	100 Hz
stability (8 h–10 s) – referred to Imax	100 ppm
stability (10 s–300 ms) – referred to Imax	100 ppm
stability (300 ms–0 ms) – referred to Imax	50 ppm
absolute accuracy – referred to Imax	100 ppm
reproducibility long term – referred to Imax	100 ppm
current ripple – referred to Imax	10 ppm 60 Hz and greater
resolution of reference current	16-bit ±1 LSB
resolution of current measured – fast sampling	16-bit ±1 LSB at 200 μsec
resolution of current measured – slow sampling	22-bit ±1 LSB at 16.67 msec

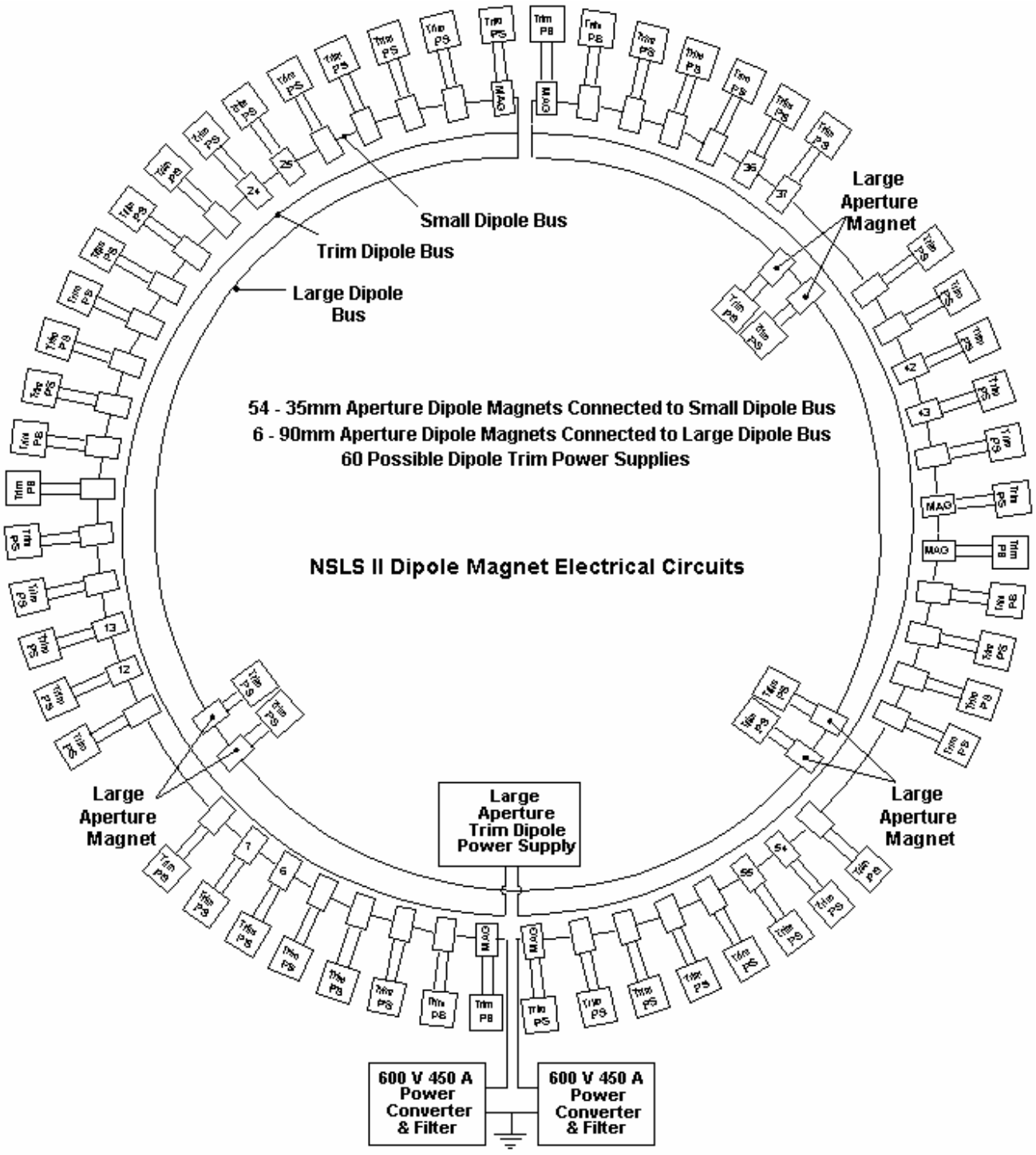

Figure 4.2.1 Storage ring dipole magnet circuit.

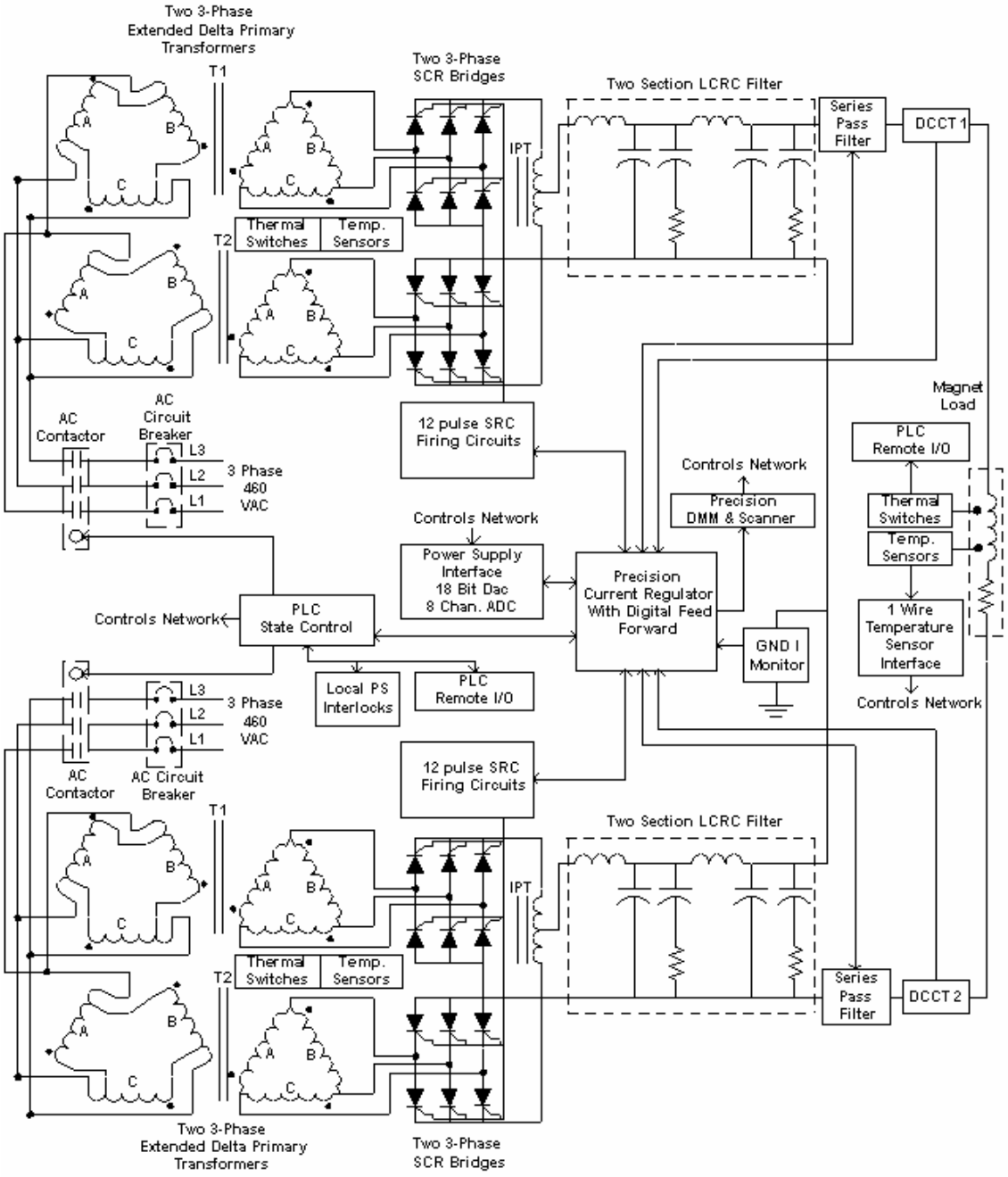

Figure 4.2.2 Dipole power supply block diagram.

4.2.2 SR-Quad-A-PS, SR-Quad-B-PS, and SR-Quad-C-PS – Quadrupole Power Supplies

These circuits will use one power supply for each magnet. The quadrupole magnet load parameters require three power supplies for the different quadrupole magnet types. There are a total of 300 magnet circuits. The following table shows which power supply is used for each type of magnet and what are the power supply loads.

PS Type	Magnet	Operating Current	Load resistance	Load Inductance	Output Cable
Quad-A	Q1L,Q3L,QF,Q3H	146 A	0.058 Ω	0.027 H	250 MCM
Quad-B	Q2L,Q2H	160 A	0.129 Ω	0.135 H	250 MCM
Quad-C	QD,Q1H	95 A	0.058 Ω	0.027 H	4/0 AWG

The cabling between the magnets and power supply will use flexible copper cables.

The power supply is a unipolar, single-quadrant, current-regulated switch-mode design. The power section is a commercial, voltage-controlled, switch-mode-programmable power supply with high output bandwidth (~0.5 kHz). These supplies have 3, 6.6, and 1.2 kW output power ratings. They fit in a standard 19-in. electronics rack and are only 3.5 and 1.75 inches high. These power supplies are air-cooled. A precision analog regulator to control the current will be developed in-house. The power supply will use a DCCT as the current feedback device. To minimize current ripple, an additional output filter can be used. An AC input module will turn the power supply on and off. A microcontroller will be used for state control (on/off commands and interlocks). See Figure 4.2.3 for a block diagram of the Quad power supply.

Quadrupole Power Supply Specifications

AC Input

PS Type	Voltage	Current	Phase
Quad-A	208 VAC	~ 11 AAC	3
Quad-B	208 VAC	~ 23 AAC	3
Quad-C	120 VAC	~ 14 AAC	1

DC Output

PS Type	Voltage	Current	Power
Quad-A	16 VDC	185 ADC	3.0 kW
Quad-B	30 VDC	220 ADC	6.6 kW
Quad-C	10 VDC	120 ADC	1.2 kW

Quadrupole Power Supply Specifications (cont.)

DC minimum output current – Imin	~0.5 ADC
operating quadrants	1: (V+, I+)
small-signal – 3 db bandwidth	100 Hz
stability (8 h–10 s) – referred to Imax	100 ppm
stability (10 s–300 ms) – referred to Imax	100 ppm
stability (300 ms–0 ms) – referred to Imax	500 ppm
absolute accuracy – referred to Imax	100 ppm
reproducibility long term – referred to Imax	100 ppm
current ripple – referred to Imax	15 ppm 60 Hz and greater
resolution of reference current	18-bit ±1 LSB
resolution of current measured – fast sampling	16-bit ±1 LSB at 200 µsec
resolution of current measured – slow sampling	22-bit ±1 LSB at 16.67 msec

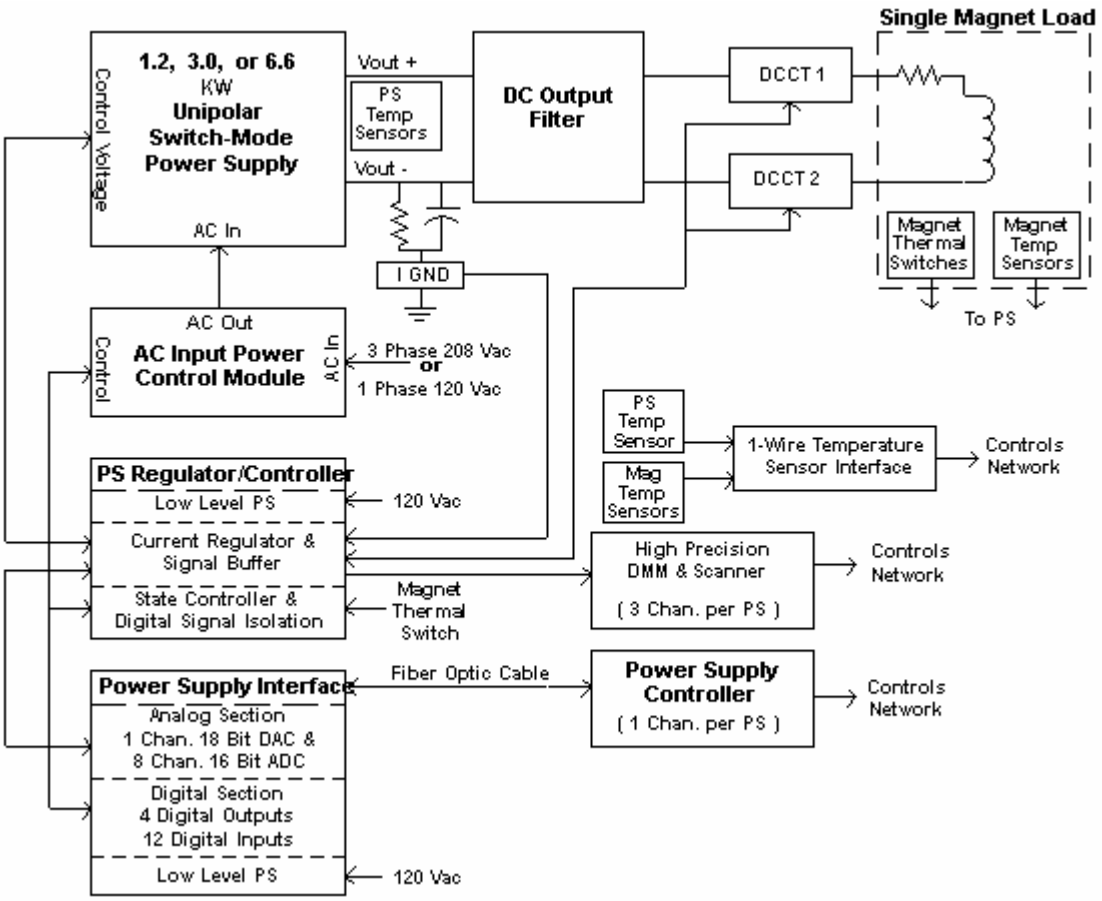

Figure 4.2.3 Quadrupole power supply block diagram.

4.2.3 SR-Sext-A-PS and SR-Sext-B-PS – Sextupole Power Supplies

These circuits will use one power supply for each family of sextupole magnets in each pentant. There are nine families in each of the five pentants. There are a total of 45 magnet circuits. The sextupole magnet load parameters require two power supply types for the different sextupole magnet families. The following table shows which power supply is used for each sextupole families and what are the power supply loads.

PS Type	Sextupole Family	Operating Current	Load resistance	Load Inductance	Output Cable
Sext-A	SL1, SL2, SL3, SL4 SH1, SH2, SH3	123 A	0.246 Ω	0.053H	250 MCM
Sext-B	SD	164 A	0.431 Ω	0.106 H	250 MCM
Sext-B	SF	164 A	0.285 Ω	0.066 H	250 MCM

The cabling between the magnets and power supply will be 250 MCM flexible copper cables. See Figure 4.2.5 for a connection diagram of sextupole families.

The supply is a unipolar, current-regulated switch-mode design, similar to that for the quadrupoles. The power section is a commercial, voltage-controlled, switch-mode-programmable power supply with high output bandwidth (~0.5 kHz). These air-cooled power supplies have an output power rating of 10 kW or 20 kW. They fit in a standard 19-in. electronics rack and are only 5.25 inches high for 10 kW and 10.5 inches high for 20 kW. A precision analog regulator to control the current will be developed in-house. The power supply will use a DCCT as the current feedback device. To minimize current ripple, an additional output filter will be used. An AC input module will turn the power supply on and off. A microcontroller will be used for state control (on/off commands and interlocks). See Figure 4.2.6 for a block diagram of the sextupole power supply.

Sextupole Power Supply Specifications

AC input

PS Type	Voltage	Current	Phase
Sext-A	208 VAC	~ 34 AAC	3
Sext-B	208 VAC	~ 68 AAC	3

DC output

PS Type	Voltage	Current	Power
Sext-A	60 VDC	167 ADC	10.0 kW
Sext-B	100 VDC	200 ADC	20.0 kW

Sextupole Power Supply Specifications (cont.)

DC minimum output current – Imin	~0.5 ADC
DC output voltage	12 VDC
operating quadrants	1: (V+, I+)
small-signal – 3 db bandwidth	100 Hz
stability (8 h–10 s) – referred to Imax	100 ppm
stability (10 s–300 ms) – referred to Imax	100 ppm
stability (300 ms–0 ms) – referred to Imax	50 ppm
absolute accuracy – referred to Imax	100 ppm
reproducibility long term – referred to Imax	100 ppm
current ripple – referred to Imax	15 ppm 60 Hz and greater
resolution of reference current	16-bit ±1 LSB
resolution of current measured – fast sampling	16-bit ±1 LSB at 200 μsec
resolution of current measured – slow sampling	22-bit ±1 LSB at 16.67 msec

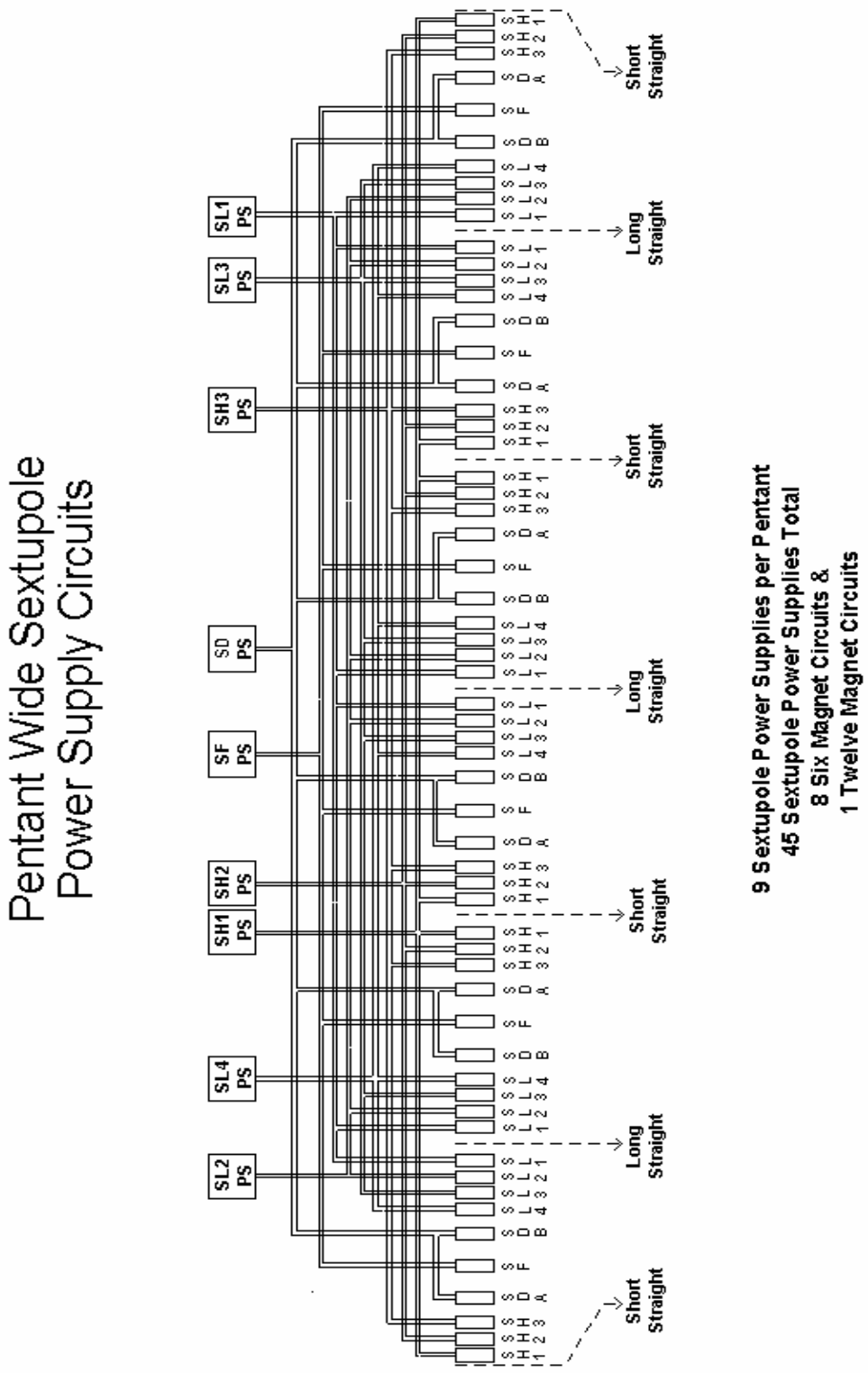

Figure 4.2.5 Connection diagram of sextupole families.

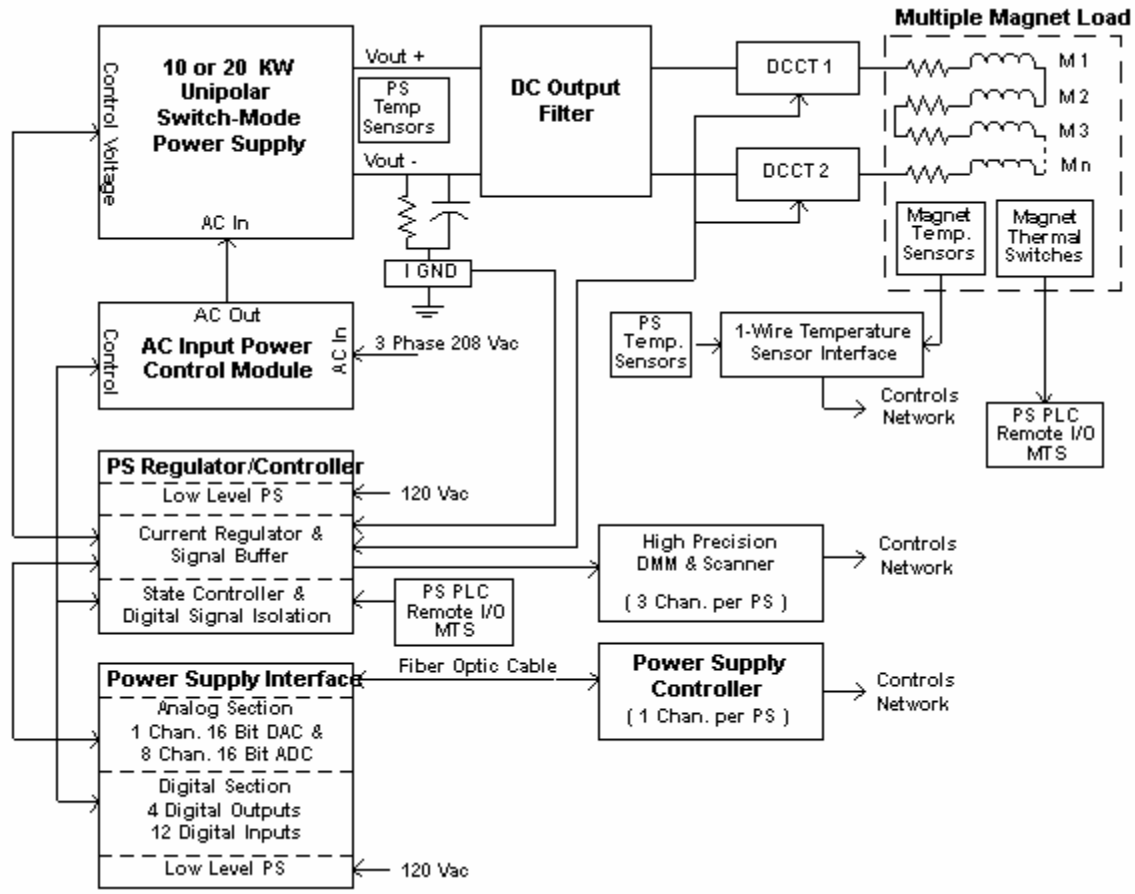

Figure 4.2.6 Sextupole power supply block diagram.

4.2.4 SR-Dipole Trim-PS and SR-SKQ-PS – Dipole Trim Coil and Skew Quadrupole Power Supplies

The Dipole Trim PS circuit consists of the trim coil sets located in the dipole magnets. The coil set is 3.11 Ω and 26 mH for small-aperture dipole and 8.67 Ω and ~90 mH. The SKQ power supply circuit consists of a corrector coil that is still to be placed in the lattice; this coil is estimated at 3.0 Ω and 5 mH. The operating current for these power supplies is ~2 A for 3.0 GeV. The cabling from the coil set to the power supply will be # 10 AWG flexible copper, routed through the tunnel ceiling into the equipment area above the main tunnel. The cabling has a resistance of 0.153 Ω and an inductance of 0.1 mH. The worst-case power supply load is 8.82 Ω and ~ 0.09 H.

The bipolar, 4-quadrant, current-regulated linear power supply fits in a standard 19-in. electronics rack and is 5.25 inches high. A precision analog regulator to control the current will be used. The power supply will use a DCCT as the current feedback device. A microcontroller will be used for state control (on/off commands and interlocks).

B1 Trim PS and SKQ PS Power Supply Specifications

AC input power	1-phase 120 VAC ~2.4 AAC
DC maximum output current – Imax	+5 ADC
DC minimum output current – Imin	–5 ADC
DC output voltage	±20 VDC
operating quadrants	4: (V+, I+), (V–, I+) , (V–, I-) & (V+, I–)
small-signal – 3 db bandwidth	10 kHz
large-signal bandwidth	~5 Hz
stability (8 h–10s) – referred to Imax	100 ppm
stability (10 s–300 ms) – referred to Imax	100 ppm
stability (300 ms–0 ms) – referred to Imax	50 ppm
absolute accuracy – referred to Imax	100 ppm
reproducibility long term – referred to Imax	100 ppm
current ripple – referred to Imax	10 ppm 60 Hz and greater
resolution of reference current	16-bit ±1LSB
resolution of current measured – fast sampling	16-bit ±1 LSB at 200 μsec
resolution of current measured – slow sampling	22-bit ±1 LSB at 16.67 msec

4.2.5 SR-BH-PS and SR-BV-PS – Intermediate Speed Horizontal and Vertical Corrector Coil Power Supplies

The BH and BV Corrector PS circuits consist of the corrector coil set located in an HVC magnet. Each coil set is ~0.34 Ω and ~25 mH. This coil set is estimated at 3.0 Ω and 1 mH. The operating current for both power supplies is ~15 A for 3.0 GeV. The cabling from the coil sets to the power supplies will be # 10 AWG flexible copper cables, routed through the tunnel ceiling into the equipment area above the main tunnel. The cabling has a resistance of 0.148 Ω and an inductance of 0.1 mH. The worst-case power supply load is 0.488 Ω and ~25 mH.

The BH and BV power supplies are bipolar, 4-quadrant, current-regulated linear PS that fit in a standard 19-in. electronics rack and are 5.25 inches high. A precision analog regulator to control the current will be used. The power supply will use a DCCT as the current feedback device. These corrector power supplies are part of an intermediate-speed beam position feedback system. A microcontroller will be used for state control (on/off commands and interlocks).

Corrector Coil Set Power Supply Specifications

AC input power	1-phase 120 VAC ~7.3 AAC
DC maximum output current – Imax	+ 24 ADC
DC minimum output current – Imin	– 24 ADC
DC output voltage	±25 VDC
operating quadrants	4: (V+, I+) , (V–, I+), (V–, I–) & (V+, I–)
small-signal – 3 db bandwidth	1 kHz
large signal – bandwidth	~5 Hz
stability (8 h–10 s) – referred to Imax	100 ppm
stability (10 s–300 ms) – referred to Imax	50 ppm
stability (300 ms–0 ms) – referred to Imax	25 ppm
absolute accuracy – referred to Imax	100 ppm
reproducibility long term – referred to Imax	100 ppm
current ripple – referred to Imax	5 ppm 60 Hz and greater
resolution of reference current	18-bit ±1 LSB
resolution of current measured – fast sampling	16-bit ±1 LSB at 200 μsec
resolution of current measured – slow sampling	22-bit ±1 LSB at 16.67 msec

4.2.6 SR-FIBH-PS and SR-FIBV- PS Fast Insertion Horizontal and Vertical Corrector Power Supplies

The FIBH and FIBV fast insertion corrector power supply circuits consist of the corrector coil set located in a fast insertion HVC magnet. These magnets are located in the insertion region on either side of an insertion device. Each coil set is estimated at ~0.8 Ω and ~ 10 mH. The operating current for the power supplies is ~2 A for 3.0 GeV. The cabling from the coil sets to the power supply will be # 10 AWG flexible copper, routed through the tunnel ceiling into the equipment area above the main tunnel. The cabling has a resistance of 0.152 Ω and inductance of 0.1 mH. The worst-case power supply load is ~0.95 Ω and 0.010 H.

The FIBH and FIBV power supplies are bipolar, 4-quadrant, current-regulated linear power supplies that fit in a standard 19-in.electronics rack and are 5.25 inches high. A precision analog regulator to control the current will be used. The power supply will use a DCCT as the current feedback device. These corrector power supplies are part of a fast beam position feedback system. A microcontroller will be used for state control (on/off commands and interlocks).

Fast Insertion Corrector Power Supply Specifications

AC input power	1-phase 208 Vac ~2.6 AAC
DC maximum output current – Imax	+ 5 ADC
DC minimum output current – Imin	- 5 ADC
DC output voltage	± 20 VDC
operating quadrants	4: (V+, I+) , (V–, I+), (V–, I–), & (V+, I–)
small-signal – 3 db bandwidth	10 kHz
large signal – bandwidth	100 Hz
stability (8 h–10 s) – referred to Imax	100 ppm
stability (10 s–300 ms) – referred to Imax	50 ppm
stability (300 ms–0 ms) – referred to Imax	25 ppm
absolute accuracy – referred to Imax	100 ppm
reproducibility long term – referred to Imax	100 ppm
current ripple – referred to Imax	5 ppm 60 Hz and greater
resolution of reference current	18-bit ±1 LSB
resolution of current measured – fast sampling	16-bit ±1 LSB at 200 μsec
resolution of current measured – slow sampling	22-bit ±1 LSB at 16.67 msec

4.2.7 SR-FGBH-PS and SR-FGBV-PS Fast Global Horizontal and Vertical Corrector Power Supplies

The FGBH and FGBV fast global corrector power supply circuits consist of the corrector coil set located in a fast global HVC magnet. This magnet is located over stainless steel bellows on both sides of the dipole magnets. This magnet serves as an alignment and fast orbit position corrector. This requires the power supply to have both high voltage and current. The operating current for the power supplies is ~15 A for 3.0 GeV The coil resistance is ~0.5 Ω and coil inductance is ~ 0.10 mH. The cabling from the coil sets to the power supply will be # 10 AWG flexible copper, routed through the tunnel ceiling into the equipment area above the main tunnel.

The FGBH and FGBV power supplies will use a switch-mode, bipolar, four-quadrant, current-regulated power supply. It will fit in a standard 19-in. electronics rack. A precision analog regulator to control the current will be used. The power supply will use a DCCT as the current feedback device. These corrector power supplies are part of a fast beam position feedback system. A microcontroller will be used for state control (on/off commands and interlocks). See Figure 4.2.7 for a block diagram of the fast global corrector power supply.

Fast Global Corrector Power Supply Specifications

AC input power	120 VAC ~14 AAC
DC maximum output current – Imax	+ 24 ADC
DC minimum output current – Imin	- 24 ADC
DC output voltage	± 45 VDC
operating quadrants	4: (V+, I+), (V–, I+), (V–, I–), & (V+, I–)
small-signal – 3 db bandwidth	5 kHz
large signal – bandwidth	100 Hz
stability (8 h–10 s) – referred to Imax	1,000 ppm
stability (10 s–300 ms) – referred to Imax	50 ppm
stability (300 ms–0 ms) – referred to Imax	25 ppm
absolute accuracy – referred to Imax	100 ppm
reproducibility long term – referred to Imax	100 ppm
current ripple – referred to Imax	5 ppm 60 Hz and greater
resolution of reference current	20-bit ± 1 LSB
resolution of current measured – fast sampling	16-bit ± 1 LSB at 200 µsec
resolution of current measured – slow sampling	22-bit ± 1 LSB at 16.67 msec

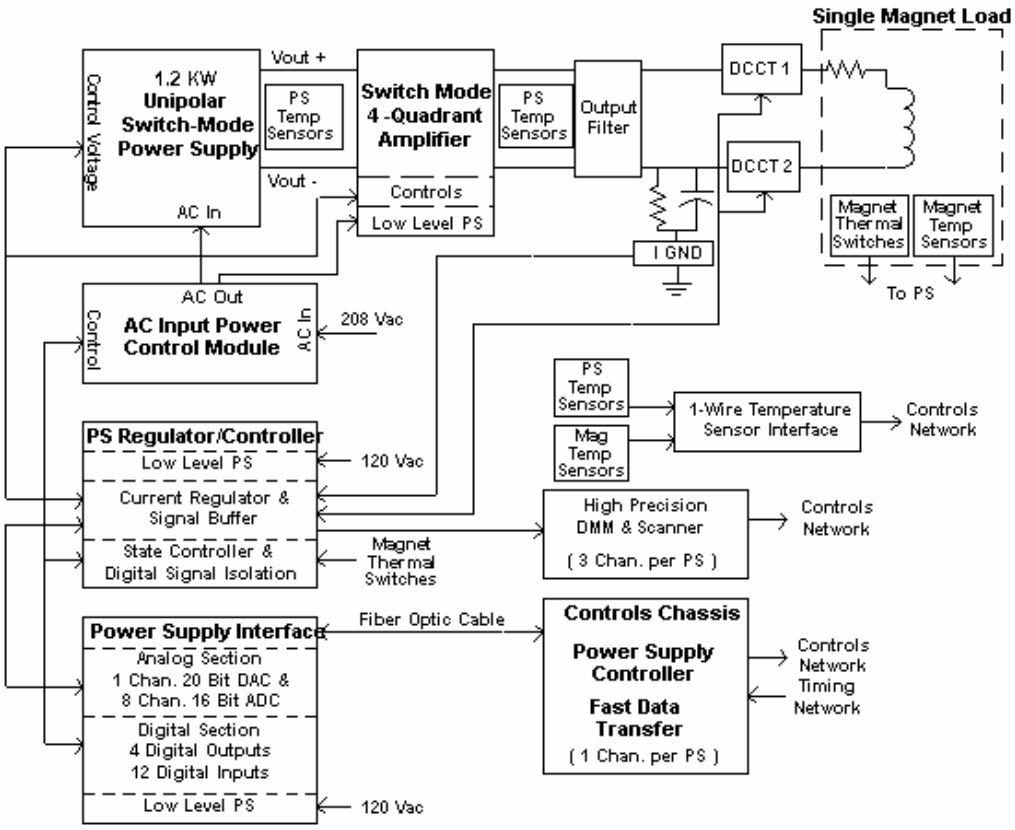

Figure 4.2.7 Block diagram of the Fast Global Corrector power supply.

4.2.8 Power Supply Interlocks

All power supplies will have sufficient interlocks that will prevent the power supply from becoming damaged due to changes in cooling conditions, AC power disturbances, and nonstandard operating conditions.

All magnet coils will have an over- temperatures interlock if there is a change in cooling and/or operating conditions. Temperature interlock for magnets that are part of ring- and pentant-wide circuits will be interfaced to a ring-wide interlock system. This system will use a PLC with remote I/O modules located in every cell. The system will monitor all the thermal switches on these magnets and route the interlock signal to the appropriate power supplies.

All power supplies will have an electrical safety interlock that will prevent the power supply from turning on if the machine safety system requires it.

4.2.9 Power Supply Instrumentation

Redundant DCCTs will be used to confirm the power supply current reproducability.

High-precision DMMs and scanners will be used to monitor the power system current, the redundant current sensor, and the analog current set point. This equipment will ensure long-term stability and reproducability.

Temperature monitoring of the magnet coils and power system environment will be accomplished using low-cost digital temperature sensors. With such systems, a problem can be identified before it becomes an emergency, making it possible for repairs to be scheduled more conveniently.

4.2.10 Power Supply Controls

The Power Supply Interface has a precision DAC for generating the reference current and a multi-channel ADC for inputting PS signals. The PSI also has digital I/O for state control and status readbacks of the PS.

A VME device card will be used to communicate between the control system and the PSI. This card will be located in a control system's VME chassis that will be mounted in one of the power supply system racks. This card will generate the reference current profiles, input analog data, and perform digital state control and status readbacks. The output of the device card is a fiber optics cable that connects to a PSI.

The other controls will include the operation of the high-precision DMM and scanner and readout of the digital temperature sensors.

4.2.11 Electrical Safety

All power supplies will conform to the latest BNL safety requirements, especially concerning arc flash protection. Whenever possible, NRTL-listed equipment will be used.

4.2.12 Cable Tray and Cable Routing

The cable tray for the magnet circuits will be located in the equipment area above the main tunnel. The cable will drop through the tunnel ceiling at two locations in each cell, where it will connect to two dipole magnets. There will also be a tray inside the main tunnel only in the area of the cell. This tray will be located over the storage ring magnets. The single cables will be installed with a twist to prevent pickup from noise sources. All cables will be tray-rated cables. Power supply cables will be arranged to minimize pickup from other circuits. All power cables will be separated from signal cables. The quadrupole, sextupole, and corrector

cables will be routed through conduit in the main tunnel ceiling. The cable going through the conduit will run in the cable tray in the tunnel until it is connected to the magnet. All cables and trays will meet NEC codes.

See Figure 4.2.8 for a block diagram of the cable and tray for one cell.

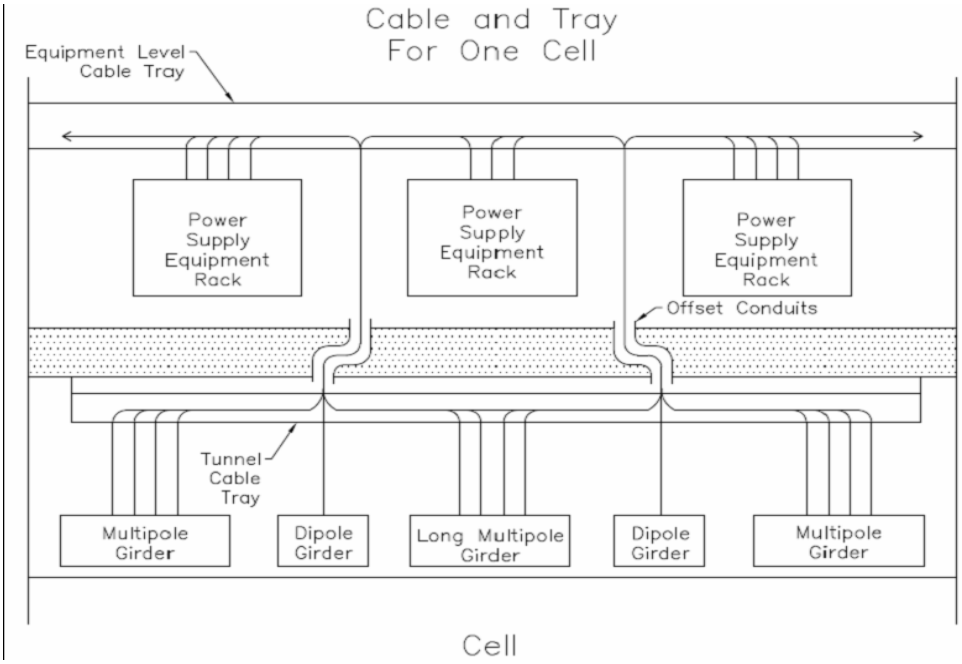

Figure 4.2.8 Block diagram of the cable and tray for one cell.

4.2.13 Power Supply Racks

All storage ring power supplies except for the dipole will be mounted in sealed Nema 12 electronics racks. These racks will have a maximum of six 3kW power supplies installed in them. These racks will also have power supply controls and instrumentation installed in them. At each cell location there are 11 power supply racks (Figure 4.2.9). The power racks will be located above the magnets they supply.

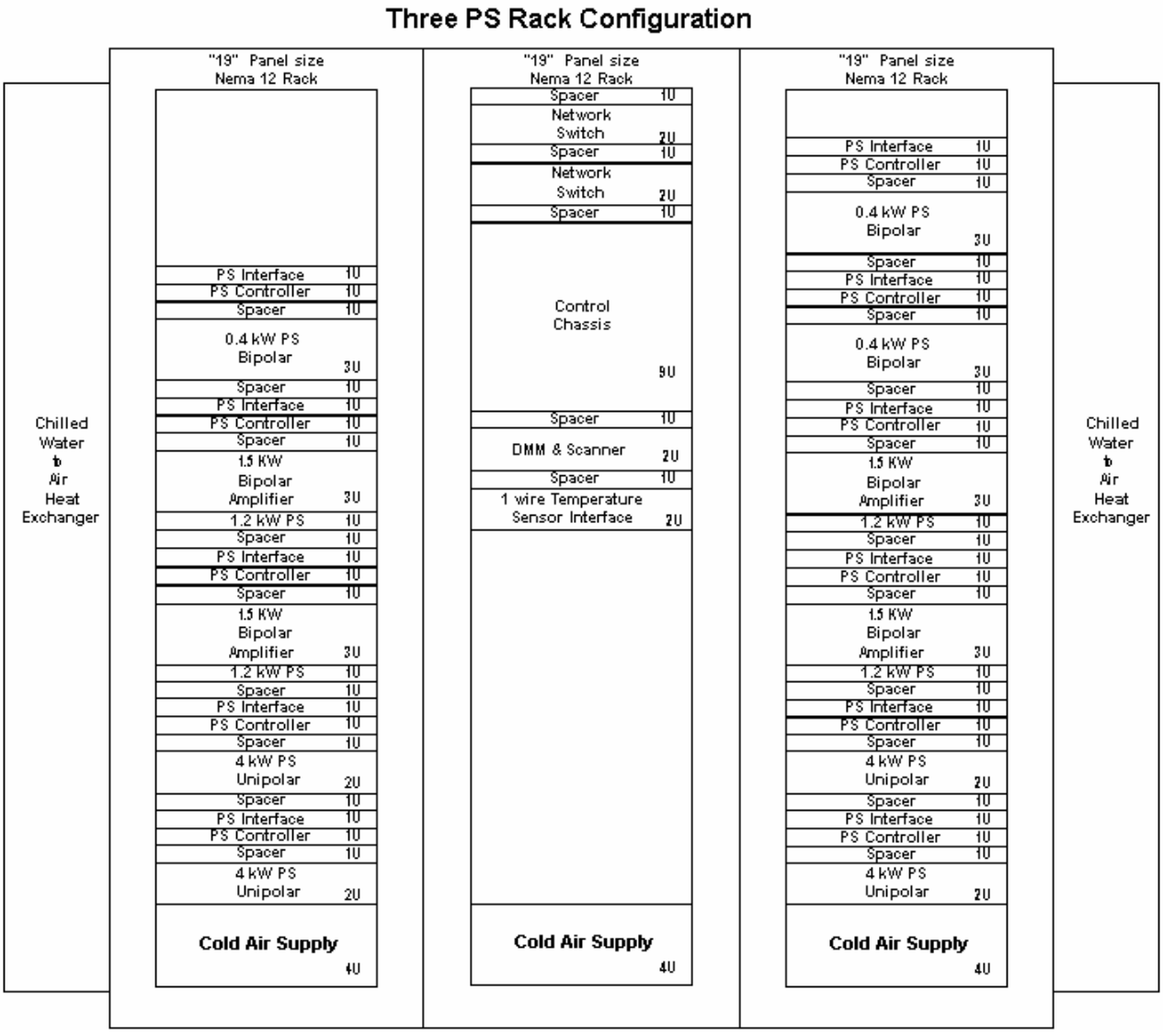

Figure 4.2.9 Magnet power supply rack layout.

A water-to-air heat exchanger will cool a set of three or four racks. Cooled air will flow through the power supplies and circulate back to the heat exchanger. The heat exchanger will use chilled water and have the outlet temperature regulated (Figure 4.2.10).

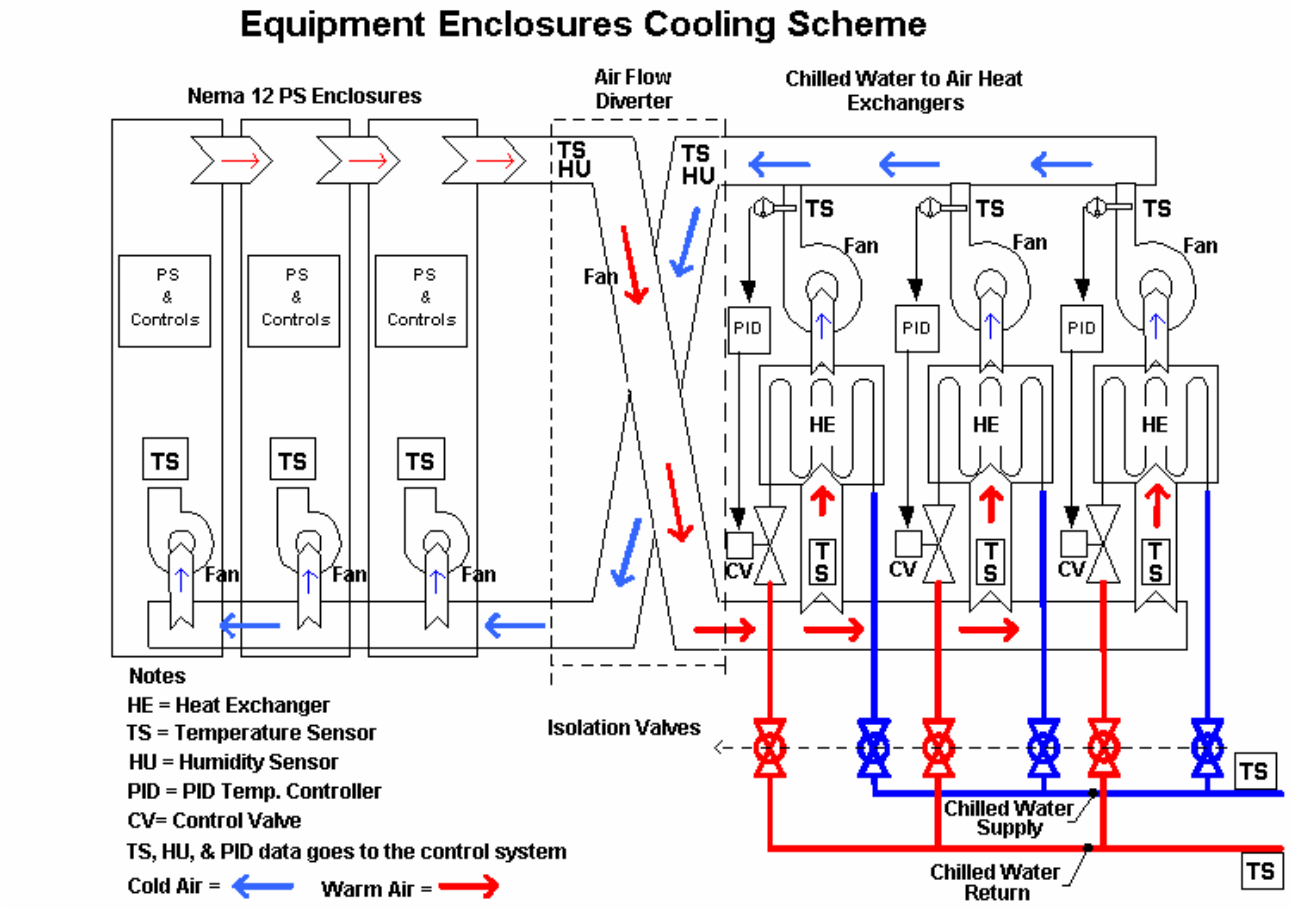

Figure 4.2.10 Rack cooling scheme.

4.3 Magnet–Girder Support System

4.3.1 Scope

This section describes alignment tolerances, stability requirements, and preliminary design of the storage ring magnet support system. Specifications for magnet alignment and stability are established from analysis of the storage ring nonlinear dynamics. Functional requirements of the girder supports are presented and design features for meeting these requirements are discussed. Various sources of ambient motion affecting the stability of the support system are identified and design solutions to mitigate their effects are discussed

4.3.2 Alignment Tolerances and Stability Requirements

The alignment tolerances for the ring magnets impact the ring performance in several ways. Magnet alignment is necessary to be able to store the electron beam with the design emittance and lifetime (i.e., sufficient dynamic aperture, DA). First, there is a relative magnet-to-magnet alignment tolerance to a line relative to the rigid girder. Second, there is an alignment tolerance specified for the transverse position of the ends of the girder and its roll angle and longitudinal position (six parameters), as it is installed in the tunnel. The girder misalignment introduces a correlated offset of the magnets. For this preliminary design, we took the achievable magnet-to-magnet alignment values from recently commissioned light sources as our specification and calculated the impact on the DA. Future studies will further explore sensitivity to these tolerances, along with the tolerance on magnetic field errors. The current tolerances are listed in Table 4.1.1. The impact of tolerance errors is discussed in Section 4.1.1.

The stability of closed-orbit position is critical to providing a constant flux in the user beamlines (i.e., intensity through slits and mirror systems). There are several sources of steering that cause large closed-orbit motion (relative to the user beamline): power supply fluctuations, energy modulations, and alignment variations due to vibrations of the magnets. We only consider the last effect here. The magnet motions that are of most concern are those of the quadrupole transverse position, dipole longitudinal position, and roll angle. This closed-orbit motion is the result of the large COAF, discussed in Section 4.1, which determined the magnitude of beam motion per unit of transverse motion of the quadrupoles, assuming that all quadrupole motions were uncorrelated in location around the ring, as well as uncorrelated in time. Here we discuss in more detail the time variation of the beam orbit due to quadrupole and dipole motion and the impact this has on the user beam.

To estimate the magnitude of the resulting orbit motion, we need to know how the quadrupoles are shifted around the ring. This depends on the noise source that generates this motion, as well as its coupling to the magnets through their support system (girders and floor). The simplest model of these magnet vibrations is just the random fluctuations of the magnet centers by a common tolerance level and assuming this impact will be the same at any frequency of vibration. This tends to overestimate the impact on the beam motion, since it ignores correlations that will smooth the distortions, as well as the synchrotron radiation damping that will damp the beam to the shifted closed orbit. This latter effect will mean that for frequencies greater than $F_{x,y} \approx 1/\tau_{x,y}$, where $\tau_{x,y}$ are the transverse damping times, the effective beam emittance will grow, while the centroid orbit shift will be reduced from that estimated from the random closed-orbit shift calculation.

We place a limit on the amplitude of magnet motion to be that which contributes to an RMS orbit shift equal to 10% of the RMS beam size in that plane. These sizes are shown in Table 4.3.1 for beam at the center of the two ID straight sections (long and short, LID and SID):

Table 4.3.1 Beam size at the center of the ID straights for 0.5 nm-rad (x) and 0.008 nm-rad (y) emittance.

Long ID	Long ID	Short ID	Short ID	TPW
σ_x, σ_y	σ_x, σ_y	σ_x, σ_y	σ_x, σ_y	σ_x, σ_y
[μm], [μrad]	[μm], [μrad]	[μm], [μrad]	[μm], [μrad]	[μm], [μm],
107.7 4.64	4.8 1.67	29.6 16.9	3.1 2.58	175 12.4

The closed orbit at the center of the short straight section for 2,000 random seeds is shown in Figure 4.3.1, for the ring quadrupoles shifted by Gaussian random values with RMS values of (ΔX = 0.157 μm and ΔY = 0.022 μm). Each point represents a different sampling of the random fluctuations of the quadrupole centers at any frequency with that amplitude, and includes all of the nonlinear elements in the calculation.

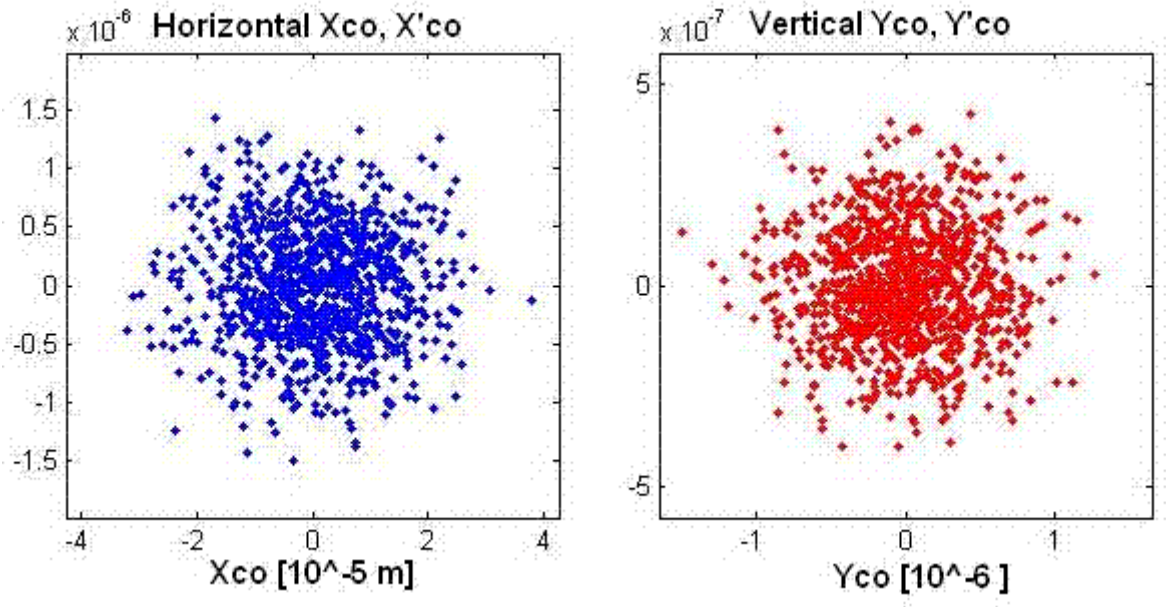

Figure 4.3.1 The horizontal and vertical closed-orbit in the LID straight for 2,000 seeds with RMS random quadrupole center shifts of ΔX = 0.157 and ΔY = 0.022 μm.

The RMS horizontal and vertical beam orbit shifts were 19.4 and 0.5 μm, respectively, or 10% of the RMS beam size in the LID. These RMS values give a very conservative tolerance for quadrupole vibration tolerances. At frequencies above the damping frequency, $F_{x,y}$, this calculation gives an estimate of the emittance dilution.

$$\Delta\varepsilon_x / \pi = \frac{1}{n}\sqrt{\sum x^2 \sum x'^2 - \left(\sum x\, x'\right)^2} \tag{4.3-1}$$

where x and x' are closed orbit and slope from each seed and the sum is over all seeds. The effective emittance dilution shown in Figure 4.3.1 is only 1% horizontal and 1% vertical of the emittance plane, or $\Delta\varepsilon_x$ = 5.1 pm and $\Delta\varepsilon_y$ = 0.09 pm, representing a small increase in the damped beam emittance.

Since the dipole magnets do not have gradients, their transverse motions have little impact on the closed-orbit motion. However, longitudinal position fluctuations of the dipoles will also create a horizontal beam

motion and the roll angle will create a vertical closed-orbit motion. Using a similar random distribution analysis, we set a tolerance level for the RMS fluctuations of the dipole longitudinal position, $\Delta S < 2$ μm, and the dipole roll angle of $\Delta\theta < 0.1$ μrad. These tolerances, together with the quadrupole levels set above, contribute increases of the RMS closed-orbit motions of 11% and the effective emittance dilution of

$$\Delta\varepsilon_x = 5.6 \text{ pm and } \Delta\varepsilon_y = 0.12 \text{ pm.} \quad (4.3\text{-}2)$$

Because the magnets are not supported independently but on girders, magnetic center fluctuations will be correlated. In Section 7.1.1 the effect of random misalignment of the girders was considered and the closed-orbit Girder Amplification Factor was computed to be 3 to 5 times less than the COAF for the quadrupoles, for independent fluctuations. The GAFs in the long ID straight sections are 34 μm (H) and 7.8 μm (V). In the short ID straight sections the GAFs are 9.4 μm (H) and 4.3 μm (V). To maintain an RMS closed-orbit fluctuation of ~10% of the RMS beam size in the LID would require random girder fluctuations of less than 0.31 μm (H) and 0.061 μm (V). The tolerances for the SID would be 0.31 μm (H) and 0.0072 μm (V). This shows the reduction in tolerance levels for vibrations coming from the correlation of the magnet vibrations, compared to the random quadrupole tolerance, and that the random model tends to yield a worst-case tolerance level estimate for vibrations.

Another model for quadrupole magnet center fluctuations attempts to include a magnet-to-magnet spatial correlation based on a ground movement model of a plane wave passing through the ring. This model was implemented in the accelerator design code BETA-ESRF [4.3.1]. The horizontal and vertical quadrupole motions are then calculated from the amplitude and wavelength (λ) of the wave. The increase in the effective emittance can be calculated from the closed-orbit shift around the ring using Eq. (4.3-1). Since there will be a dependence on the direction of the wave relative to straight sections, several phases relative to the lattice orientation have been considered, to estimate the maximum impact. The wavelength varies as a function of frequency, which depends on the knowledge of the speed of propagation. We assumed V = 270 m/sec for both S and P waves (see Section 4.3.3.5.1 for measurement for the BNL site). The impact on the beam's closed-orbit shift is then estimated by displacing the center of each quadrupole on the corresponding point of the plane wave. The effective amplitude of the closed-orbit distortion is estimated by sampling the closed orbit around the ring, instead of for different seeds. No consideration for the girders is taken, nor is there any damping of the wave or the beam assumed. Figure 4.3.2a shows the tolerance level for the horizontal (pressure, P) wave amplitude versus frequency ($f = V/\lambda$), for an effective emittance dilution that is 1% of the beam emittance, or 5 pm.

Figure 4.3.2b shows the tolerance level for the vertical (shear, S) wave amplitude versus frequency ($f = V/\lambda$), for an emittance dilution that is 1% of the beam emittance, or 0.08 pm. Clearly, as the wavelength exceeds the ring diameter of 248 m (f<~2 Hz), the entire ring moves in phase and the closed-orbit impact becomes small; the tolerance becomes quite large. Above 20 Hz (H) and 10 Hz (V), the amplitude tolerance becomes almost independent of frequency, about at the levels where $\Delta X = 0.08$ μm and $\Delta Y = 0.04$ μm.

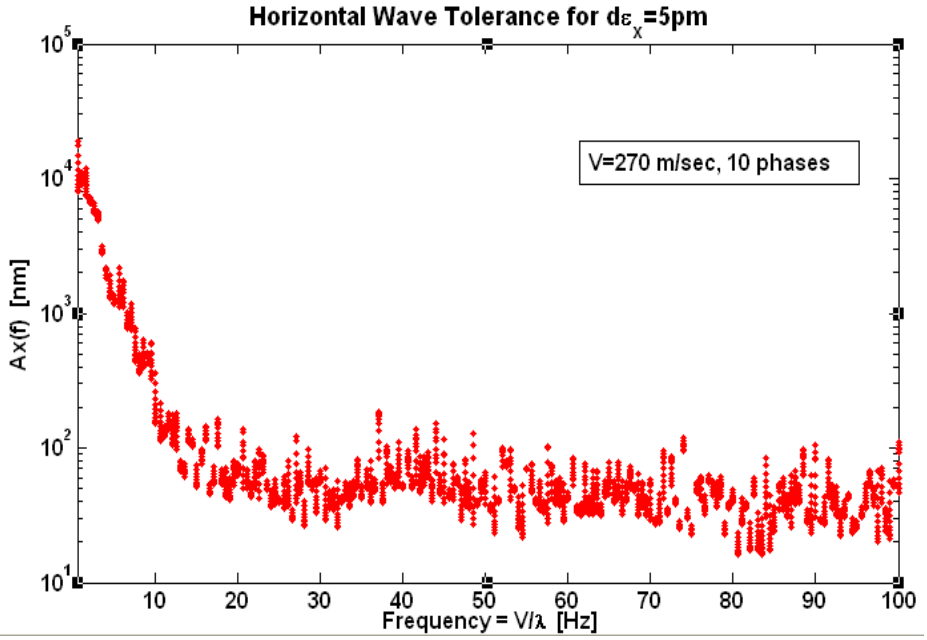

Figure 4.3.2 a The tolerance level for a horizontal wave amplitude, in nm, yielding a 5 pm emittance dilution, assuming a wave velocity of 270 m/sec.

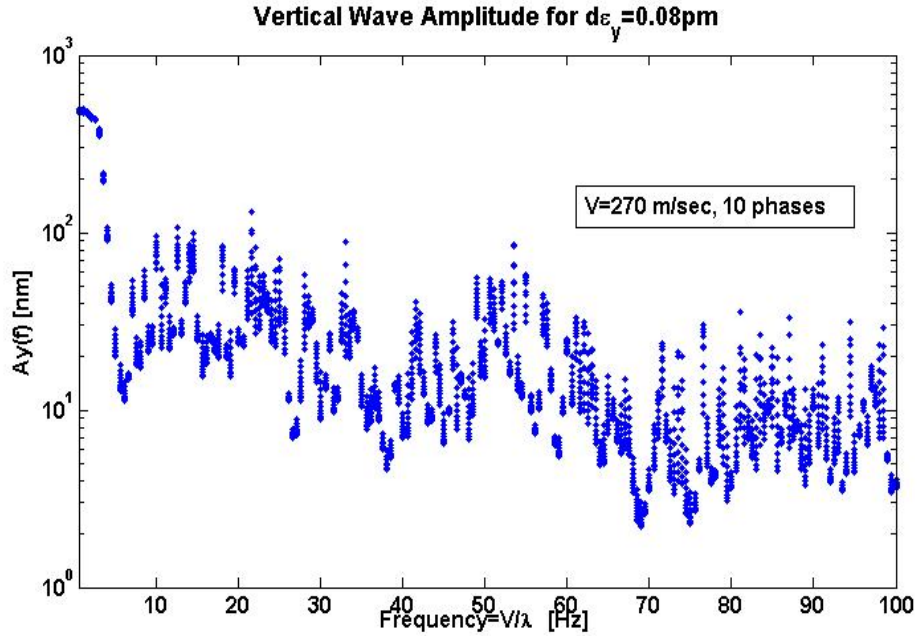

Figure 4.3.2 b The tolerance level for a vertical wave amplitude, in nm, yielding a 0.08 pm emittance dilution, assuming a wave velocity of 270 m/sec.

At frequencies below the 2 Hz level, clearly this model will yield very large tolerances, since all the ring magnets move together. In the low-frequency range (up to ~50 Hz), the global feedback system will take out most of the closed-orbit motion independent of the source term, to a level limited by the BPM and corrector electrical noise level. Above 50 Hz, the centroid motion becomes less obvious, but the beam emittance will be diluted by the effective emittance resulting from the magnet motion.

In summary, the magnet stability tolerances estimated with these models show the worst-case being the random model for the ~10% vertical beam size. However, the effective emittance contribution of this is 1% of the beam emittance and could be relaxed at least by a factor of 2, to about 0.050 μm. These tolerance limits, for the magnets only, are listed in Table 4.3.2. All other tolerances are readily achievable with careful design of girders and the accelerator floor. However, a global feedback system is planned, to ensure that orbit stability is achieved even if these tolerances cannot be achieved. Based on the calculations in Section 6.3, this feedback system will handle random quadrupole fluctuations as large as 0.3 μm vertically.

Table 4.3.2 Magnet Stability Tolerances for AC Closed-Orbit Stability, without Feedback Correction.

Tolerance Limits	ΔX RMS Quads	ΔY RMS Quads	X (LID) RMS	Y (LID) RMS	X (SID) RMS	X (SID) RMS
Random motion	<0.157 μm	<0.022 μm	10.5 μm	0.48 μm	3.2 μm	0.30 μm
Random girder motion	<0.31 μm	<0.072 μm	10.6 μm	0.5 μm	3.0 μm	0.30μm
Plane wave <5Hz	>2 μm	>0.1 μm	10.5 μm	0.5 μm	3.0 μm	0.30 μm
Plane wave >10Hz	~0.08 μm	~0.04 μm	10.5 μm	0.5 μm	3.1 μm	0.28 μm
Additional limits	**ΔS RMS Dipole**	**Δθ RMS Dipole**				
Random motion	≤2 μm	≤0.1 μrad	10 μm	0.48 μm	3.2 μm	0.30 μm

4.3.3 Preliminary Design of the Magnet–Girder Support System

4.3.3.1 Functional Requirements

The storage ring girders in a cell provide common mounting platforms for different set of magnets, as shown in Figure 4.3.3. Multipole magnets are mounted on girders in sections numbered 2, 4, and 6. Dipoles are mounted on separate girders in sections numbered 3 and 5, because of their height difference and less stringent alignment and stability requirements.

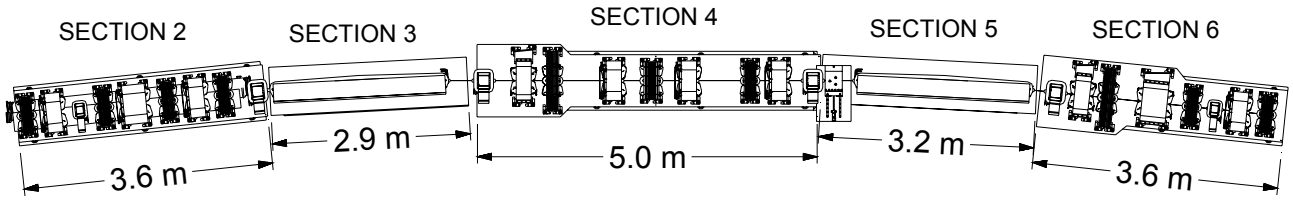

Figure 4.3.3 NSLS-II girders in one cell of the storage ring.

General functional requirements of the magnet–girder support system are given as follows:

1. Raise the centers of the magnets to the nominal beam height of 1 m. This height was chosen based on stability considerations that are discussed in Section 4.3.2.
2. Provide a stable platform for assembling and aligning the magnets outside the tunnel. The stringent alignment tolerances can only be met by precision alignment techniques (see Section 4.3.3.3) requiring out-of-tunnel assembly and alignment. The magnet alignment must remain unperturbed during the transportation and installation of the magnet–girder assemblies in the tunnel.

3. Meet girder-to-girder alignment requirements, both during the initial alignment and subsequently to compensate for long-term floor settlement.
4. Meet dynamic stability requirements under expected ambient floor motion, flow-induced vibrations, and temperature fluctuations of the tunnel air and process water.

In addition, the overall width of the magnet–girder support system must be less than 1 m, for ease of transportation and assembly in the tunnel. The support design must also be cost effective without sacrificing speed of installation and alignment.

4.3.3.2 Main Preliminary Design Features

In many recent light sources the girders have been precisely fabricated with very stringent top surface tolerances (~15 μm flatness) and with T-slot type alignment features. Magnets, built with equally tight tolerances, are fastened directly to the girder's top surface without an interface of alignment hardware. After a careful examination of this approach, we decided to design NSLS-II girders and magnets with conventional tolerances, and to use a vibrating-wire alignment technique for aligning the magnets to within ~30 μm tolerance.

A typical girder with its mounting pedestals is shown in Figure 4.3.4. The nominal length is 2.9 to 3.2 m for the dipole girders and 3.6 to 5.0 m for the multipole girders. The girders are approximately 0.8 m wide and 0.5 m high. They are fabricated by welding commercially available plates and channels of thicknesses ranging from 1 to 2 inches. After welding, the girders are stress-relieved by commercial vibratory stress-relief equipment.

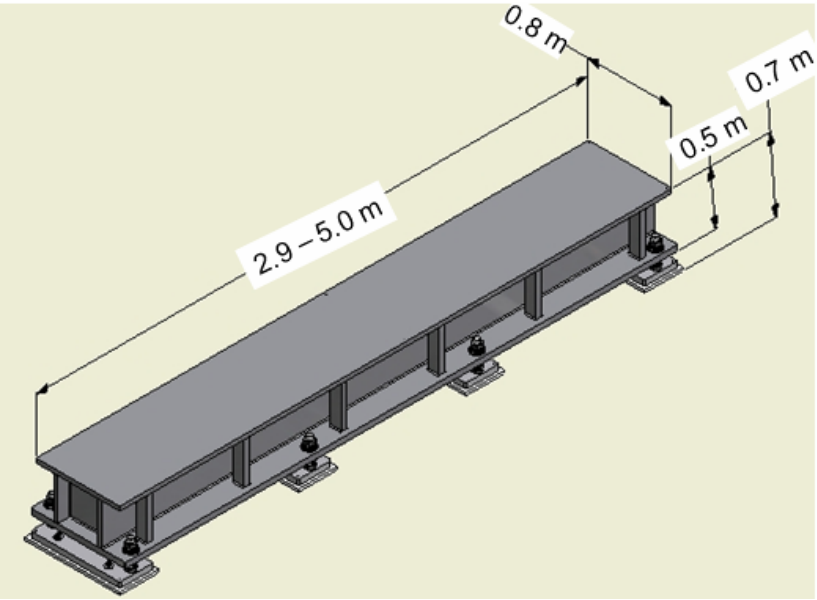

Figure 4.3.4 Preliminary design of the NSLS-II storage ring girder.

The girders are mounted on four 2-inch-thick pedestals that are grouted to the floor with nonshrinking epoxy grout. For mounting and height adjustment, eight 2 inch-diameter bolts with spherical washers are used. The girder is thus over-constrained in order to minimize static deflection and to raise the first natural frequency of the magnet–girder assembly. A similar over-constrained scheme has been used successfully at SPring-8 [4.3.2] and will be implemented at the ALBA light source [4.3.3].

4.3.3.3 Magnet–Girder Assembly and Alignment

NSLS-II lattice magnets have magnetic alignment tolerances that exceed mechanical assembly tolerances and the ability of conventional alignment techniques to locate the magnetic components within the required

tolerances. Therefore, a vibrating wire alignment technique, originally developed at Cornell University [4.3.4] and subsequently adopted at SLAC, will be used. It has been shown that this technique is capable of aligning magnets to within 10 μm with respect to an axis defined by the wire.

In this alignment technique, an oscillator drives a sinusoidal current in a thin wire (~150 μm diameter) stretched through the apertures of all the magnets on a girder while a particular magnet being measured is powered (see Figure 4.3.5).

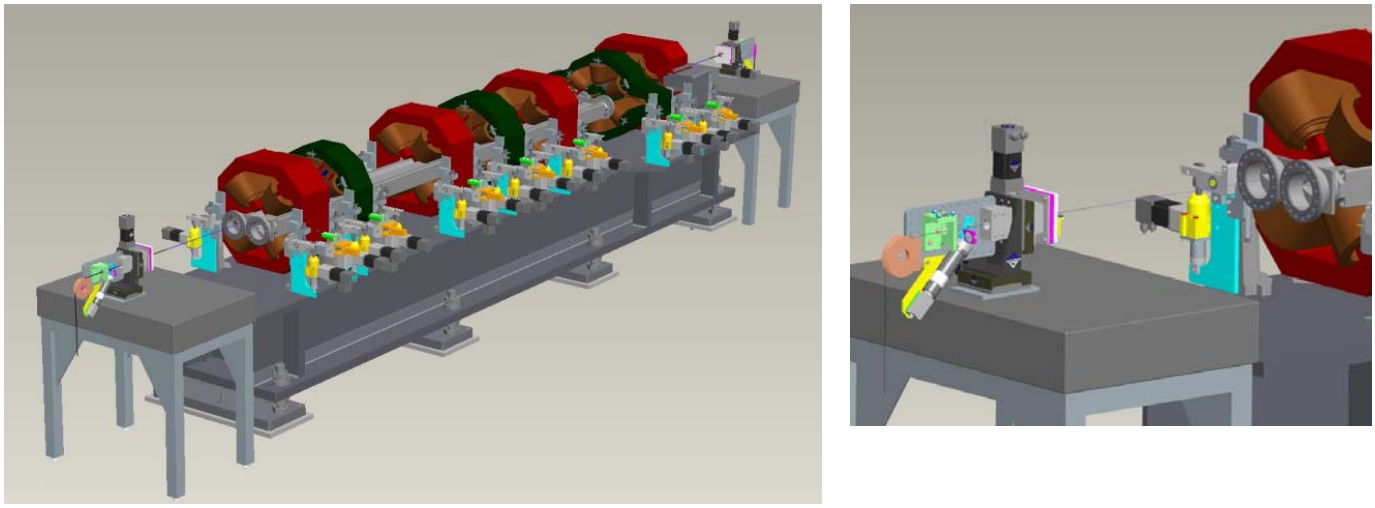

Figure 4.3.5 **Left**: Vibrating wire alignment system mounted on the girder. **Right**: Special brackets with wire movers, wire locators, and laser tracker fiducials are attached to either end of the girder.

The presence of any transverse magnetic field at the wire position exerts a sinusoidal force on the wire, causing it to vibrate. The vibrations in the wire in the transverse plane are detected by a pair of sensors (one for each axis). By carefully selecting the drive current frequency to match one of the resonant frequencies of the wire, even very small fields may produce easily detectable wire motion. For measuring average center over the length of the magnet, the resonant mode chosen is the one having an anti-node roughly at the center of the magnet being measured. The transverse field profile in the aperture of the magnet can be measured by recording the amplitude of wire motion as a function of the transverse position of the wire. In the case of a quadrupole, a linear dependence of field with horizontal and vertical position is seen, from which the magnetic axis (defined as the point where the field is zero) can be determined in the coordinate system defined by the wire translation stages. In the case of the sextupole magnets, the field profile is parabolic and the magnetic center is defined as the point where the field gradients (or equivalently, the quadrupole terms) are zero. The magnets are then moved such that the magnetic centers lie on the line joining the two end points of the wire, and are locked into place. Due to the long length (~6 to 7 m) of the wire, there is a significant sag (~600 μm) which must be precisely measured and corrected for while adjusting the magnet positions. It has been shown that the sag can be computed to sufficient accuracy from the measured fundamental resonant frequency. In the case of the quadrupoles, it may be necessary to carry out the measurements at two or more different excitation currents to eliminate any errors caused by background fields, such as the earth's field or remnant fields in the yokes of other un-powered magnets on the girder. Laser trackers are then used to transfer the positions of the wire ends (defining the axis to which all magnets are aligned) to the fiducials on the girder.

The following magnet assembly and alignment plan has been developed Upon receipt individual dipole, multipole, and corrector magnets will be subjected to an incoming test and inspection regimen. Inspections will include dimensional checks, electrical tests and magnetic measurements. Magnetic measurements shall

be performed or certified by BNL's magnet division for every lattice magnet. Magnets will then be stored until needed for girder assembly. Initially, the magnets will be installed and aligned on the girder with a laser tracker. The top-half of the multipole magnets will then be taken off and the vacuum chamber will be installed. The ends of the chamber will be sealed with Mylar caps. The caps will have small holes in either end to allow the ends of the vibrating wire to protrude through while a positive purge of dry nitrogen gas is maintained. After the top half of the magnets are reassembled, their iron cores will be supported on precisely computer-controlled positioners as shown in Figure 4.3.5. The roll angles of the magnet cores will be brought to within ±0.2 mrad tolerance by using magnet positioners and digital inclinometers. The girder is then installed in the vibrating wire test stand built in an clean temperature-controlled laboratory and all magnets are aligned to a common straight line as described above. The magnets are then tightly fastened to their supports legs.

To determine the feasibility of maintaining the magnet alignment during this fastening process, a bolting test fixture was fabricated using a Swiss Light Source magnet of the size and weight comparable to that of the NSLS-II magnets. Using electronic indicators, ten trials of positioning and then bolting the magnet were performed to replicate the procedure that will be required with the magnet mover system. Location data and time per trial were recorded. The tests proved that it is relatively quick (<10 minutes per magnet) and easy (standard fine thread hardware, no special tools nor experienced labor) to obtain a stable positioning of the magnet vertically to within 5 microns, and laterally to within 10 microns of the desired theoretically “perfect” position. Thus real magnetic alignment of the multipoles to within 20 microns on a rigid girder appears feasible.

4.3.3.4 Installation of Magnet–Girder Assemblies

A transporter system with self-contained air pads will be used to transport the girder–magnet assemblies from the alignment laboratory into the storage ring tunnel for final installation.

During the early phases of girder installation, the multipole girders will be installed prior to the dipole magnets. The wire support brackets will be left attached for the entire installation process. The air pad system will cushion any shocks to the girder during transport to prevent shifting of the magnets from their aligned positions. The girder transporter will locate the girder over the eight pedestals studs that will affix the girder to the tunnel floor.

Instrumented torque wrenches will be used in conjunction with laser trackers to precisely offload the girder from the air pads onto the pedestals’ studs. Once the girder is fixed to the floor and prior to dipole installation, in-situ vibrating wire measurements will be repeated to confirm alignment of the magnets. These measurements will be discontinued when it is established that the magnet alignment was not disturbed during transportation and alignment.

4.3.3.5 Mechanical Stability of the Magnet–Girder Support System

Sources affecting the mechanical stability of the support system include ground settlement, ambient floor motion, flow-induced vibrations, and thermal transients. These sources can be categorized in terms of the frequency range—*fast* when greater than a few Hz or *slow* when operating at frequencies lower than one Hz. Sources are also categorized based on the time-scale of the excitation, as being short (<1 hour), medium-term (<1 week), or long-term (>1 week). Short-term sources include natural and cultural ground vibrations, flow-induced vibrations, and power supply jitters. Thermal transients due to temperature changes of the cooling water or the tunnel air, as well as gravitational and tide effects, constitute medium-term sources. Floor settlement or seasonal temperature changes, which may have direct impact on the alignment of components, are considered to be long-term effects. Cultural noise or human activity is typically observed in the frequency range of 1 to 100 Hz. Ground motion from ocean waves or tides is centered at about 0.2 Hz.

4.3.3.5.1 Medium- and Long-Term Stability

Over the years, various studies have been performed at the BNL site and in the vicinity of NSLS-II to characterize the subsurface conditions. Drill-core data show that the soil at the site consists mainly of medium coarse sand with traces of silt and, in some cases, traces of clay and gravel. The shear wave velocity in the top sand layer is about 270 m/sec. The bedrock lies at a depth of approximately 430 m beneath the site. Therefore, the BNL site is classified as a very deep site with relatively soft soil. The soil consisting of glacial sands is well settled and, based on the drill-core results, exhibits limited scatter in key properties (coefficient of variation ~0.18). This is important, in that the differential movement (or settlement) in the soil supporting NSLS-II is expected to be of the order of 10 μm /10 m / year. To ensure that this is the case, a detailed study of ground settlement based on finite element analysis will be performed, taking into account both the site soil conditions and the facility layout.

4.3.3.5.2 Short-Term Stability

Short-Term Stability – Ambient Ground Motion

Ambient ground motion measurements near the NSLS-II site were taken from August 31 through September 1, 2006. Data measured at the following locations at BNL were used for a comparison of the NSLS-II site with the ALS, ESRF, and SPring-8 sites:

1. Microscopy suite of the Center for Functional Nanomaterials (CFN)
2. Foundation of a light stand near CFN, not stiffened by the presence of the building
3. A remote location near the northeast corner of BNL
4. Experimental hall of NSLS directly beneath the X1 beamline

The RMS (4–50 Hz) amplitudes of the ground motions in vertical, north–south, and east–west directions are given in Table.4.3.3. The most important value is that of the microscopy laboratory at CFN, where the RMS amplitudes are 20 nm or lower in all directions. The lower values, compared to those at the free-field at CFN and at the remote northeast BNL location, are indicative of the stiffening effect of the CFN building and the floor. The ambient ground motion at the floor of NSLS X1 beamline is considerably higher at 18 and 30 Hz, due most likely to rotating mechanical equipment.

Table 4.3.3 RMS (4-50 Hz) Ground Motion near the NSLS-II Site.

Location	Time	Vertical (nm)	North–South (nm)	East–West (nm)
Microscopy lab at CFN	7:30 pm	20	12	19
Free-Field at CFN	11:40 pm	24	41	38
Remote location near the northeast corner of BNL	Noon	21	25	26
Beamline X1 at NSLS	Midnight	71	12	13

Figure 4.3.6 shows the vertical log mean of site vibrations at the NSLS-II site expressed as PSD, compared with similar data from ALS, ESRF, and SPring-8. Shown also are PSD spectra measured at NSLS beamline X1 just after midnight, the “free-field” location near CFN, and the microscopy suite at CFN identified by the black arrow. The legend indicates the RMS amplitude using summation between 4 and 50 Hz, except for the NSLS-II log mean, which is summed with a 6 Hz lower cutoff because of contamination by the instrumentation noise floor at lower frequencies. The RMS amplitudes for ALS, ESRF, and SPring-8 were calculated in the 2 to 100 Hz band.

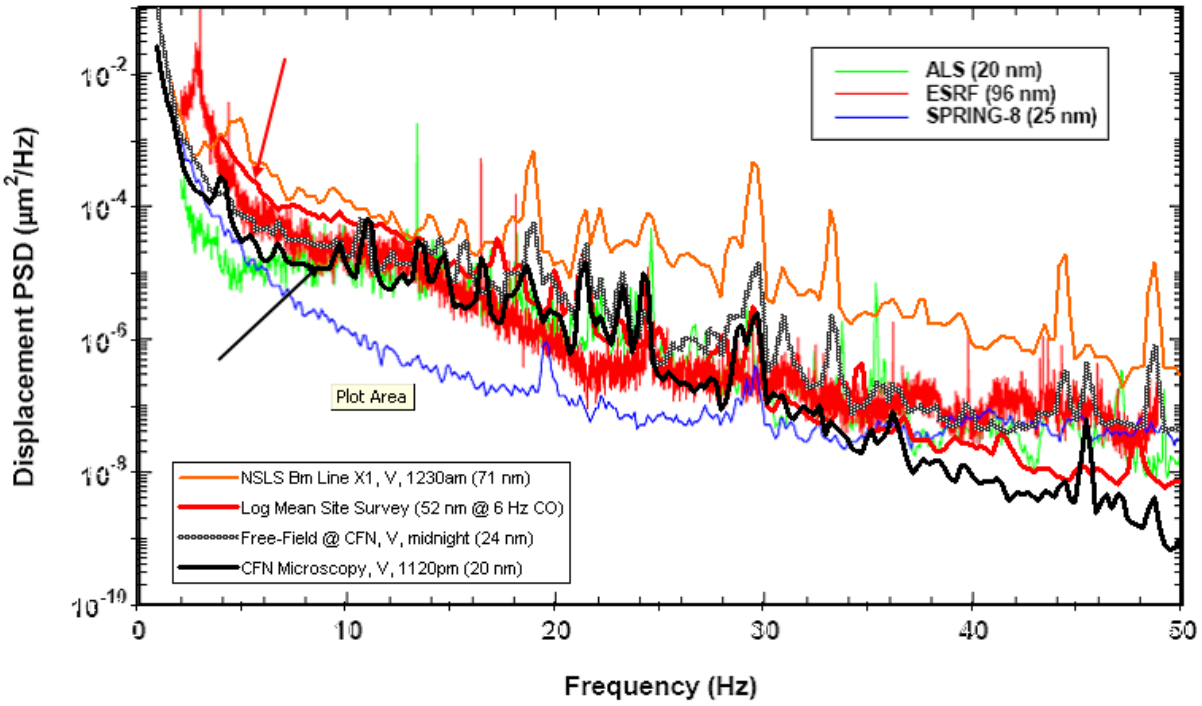

Figure 4.3.6: Comparison of PSDs of vertical ground motions at various locations near the NSLS-II site and at ALS, ESRF, and SPring-8 light sources [4.3.5].

The vibration measurements indicate the presence of local noise sources at ~18 and 30 Hz in the NSLS building. Further vibration measurements are planned to identify and eliminate these local sources of vibration. In addition, the CFN measurements show that the installation of the NSLS-II storage ring and experimental hall will significantly stiffen the site. The floor vibration levels of the NSLS-II storage ring are then expected to be comparable to those of the other light source facilities.

4.3.3.6 Resonant Frequencies of the Girder Support System

Although the NSLS-II magnet–girder assembly fastened to the pedestals is a complex dynamical system, its important design features can be understood by a simple 1-D oscillator shown in Figure 4.3.7a.

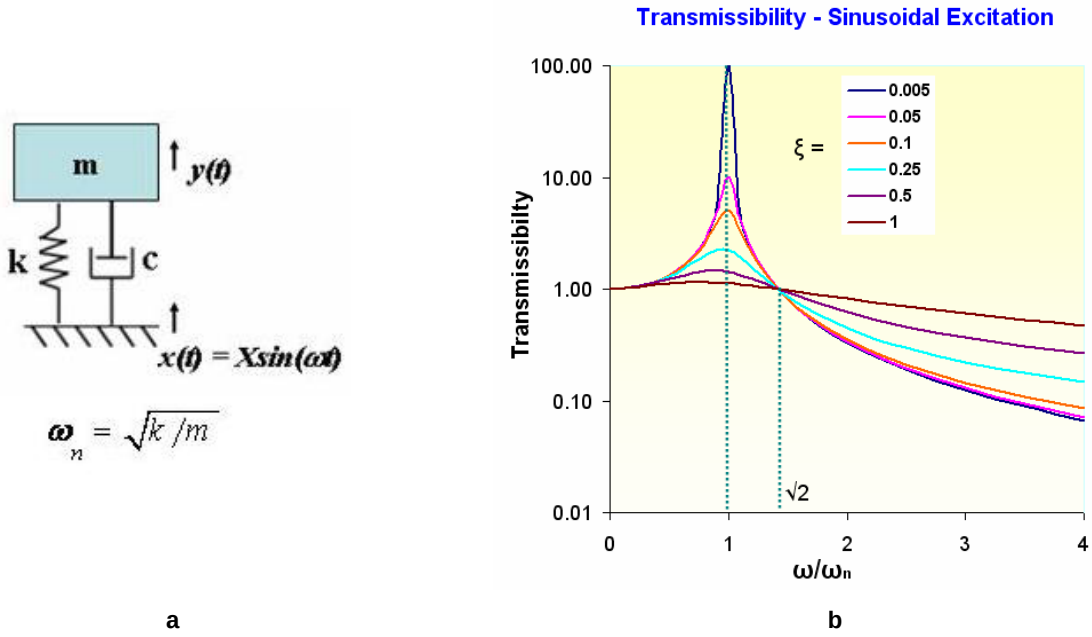

Figure 4.3.7 **a**) 1-D oscillator; **b**) transmissibility plot.

For such an oscillator, the natural frequency is

$$\omega_n = \sqrt{k/m} \tag{4.3-3}$$

and the vibration amplification (or transmissibility) is given by

$$Transmissibility = Y/X = \sqrt{\frac{4\xi^2(\omega/\omega_n)^2 + 1}{[1-(\omega/\omega_n)^2]^2 + 4\xi^2(\omega/\omega_n)^2}} \tag{4.3-4}$$

where the fraction of critical damping, ξ, is given by

$$\xi = \frac{c}{2\sqrt{mk}} \tag{4.3-5}$$

Transmissibility curves, obtained from Eq. 4.3-4 for different values of critical damping, ξ, are plotted in Figure 4.3.7b. There is no significant vibration amplification (transmissibility $\approx$ 1) when the natural frequency, ω_n, is substantially greater than the excitation frequency, ω. The ambient ground motion reduces sharply as $1/\omega^4$, as shown in Figure 4.3.6, and its amplification above 30 Hz can be ignored. Several investigations have been carried out on the dynamic response of the magnet–girder support systems using vibration measurements and finite element modal analyses. These studies have shown that it is quite difficult to raise the lowest natural frequency of the support system to greater than 20 Hz if elaborate alignment mechanisms are used either between the girder and its pedestals or between the girder and the magnets. When such alignment mechanisms are used, then the internal structural damping (ξ = 0.02 to 0.04) of the support

system is insufficient to reduce the floor motion amplification to an acceptable level. External damping devices, either active or passive, are then used, such as viscoelastic damping pads at APS and ESRF.

For the NSLS-II magnet–girder support system, a lowest natural frequency of greater than 50 Hz will be obtained by eliminating elaborate alignment mechanisms, and by lowering the beam height to 1 m. Short, stiff threaded rods will be used for height adjustment only. The alignment of the girders will be achieved by precise but removable alignment mechanisms. Finite element model analysis of the NSLS-II magnet–girder assembly shows that the lowest two natural frequencies are 58.8 Hz and 74.4 Hz. The corresponding mode shapes, rolling and twisting of the girder, are depicted in Figure 4.3.8.

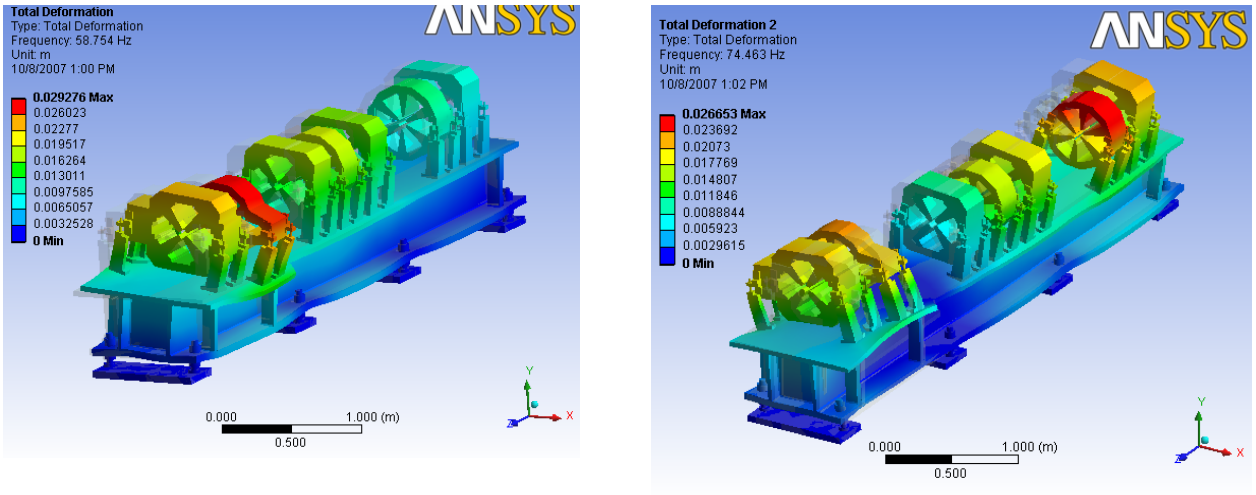

Figure 4.3.8 Mode shapes of the NSLS-II magnet–girder assembly.
Left: First mode shape, rolling, ω_1 = 58.8 Hz. **Right**: Second mode shape, twisting, ω_2 = 74.4 Hz.

4.3.3.7 Flow-Induced Vibrations

Flow-induced vibrations of the water headers can be transmitted to the magnets and the vacuum chambers [4.3.6] by flexible hoses and pipes. The effects of flow-induced vibrations will be mitigated by paying close attention to several useful design guidelines, namely:

1. Locate all rotating equipments including fans, blowers, compressors, and pumps outside the storage ring tunnel, preferable tens of meters away from the tunnel floor and ceiling.
2. Keep low flow velocities (less than 2 m/s) in the process water headers.
3. Design header supports to minimize their vibration, such as by integrating viscoelastic dampers in the headers hangers, or by attaching headers directly to the ceiling.
4. Arrange water flow circuits and connection fittings such that sharp bends are eliminated. Special attention is to be given to the routing and clamping of the hoses and tubes that connect the magnets and vacuum chambers to their respective headers.

Analytical models and vibration measurements will be employed to ensure that flow velocities required to regulate the temperature of the vacuum chambers do not induce unacceptable level of vibrations.

4.3.3.8 Thermal Stability

Ambient temperature variations will result in displacements of both the magnets on the girders and the BPMs on the vacuum chambers [4.3.7]. To ensure acceptable thermal deformations of the ring components, process water and tunnel air temperatures will be maintained to within ±0.05ºC and ± 0.1ºC, respectively, of

their nominal values, 25.0 ºC. Air-conditioning temperature cycling of ~1-hour duration will be maintained in order to take advantage of the thermal inertia of the support system. The girders will be thermally insulated to further reduce the effects of temperature transients.

Lowering the beam height from 1.4 m to 1 m would reduce the vertical thermal expansions of the assembly proportionately. In addition, over-constraining each girder to its pedestal at eight locations would minimize thermal bending effects.

To investigate the effect of temperature transients, FE thermal analyses were performed for the girder, magnets and vacuum chamber assembly. For the analyses, the fluctuations in the temperature of the tunnel air and the cooling water flowing through vacuum chamber were approximated by linear increase and decrease over 15 minuts corresponding to 1-hour temperature cycle. For modeling heat transfer by air convection, a film coefficient value of 8 W/m^2 °C and 1 W/m^2 °C was applied on all external surfaces and internal girder's surface, respectively. The lower film coefficient value was applied on the internal girder's surface to include the effect of stagnant air condition.

For modeling heat transfer by process water a film coefficient value of 15,000 W/m^2 °C was applied. For girder insulation a glass-wool material with a thermal conductivity of 0.03 W/m °C was considered in the analysis.

Figure 4.3.9 shows the temperature distribution in girder, magnets and vacuum chamber assembly. The maximum temperature change in the girder and magnets is limited to ~ 0.01ºC due to the effects of thermal mass and girder insulation. For the vacumm chamber, however, the temperature change is ~ 0.05ºC, the same as the change in the water temperature.

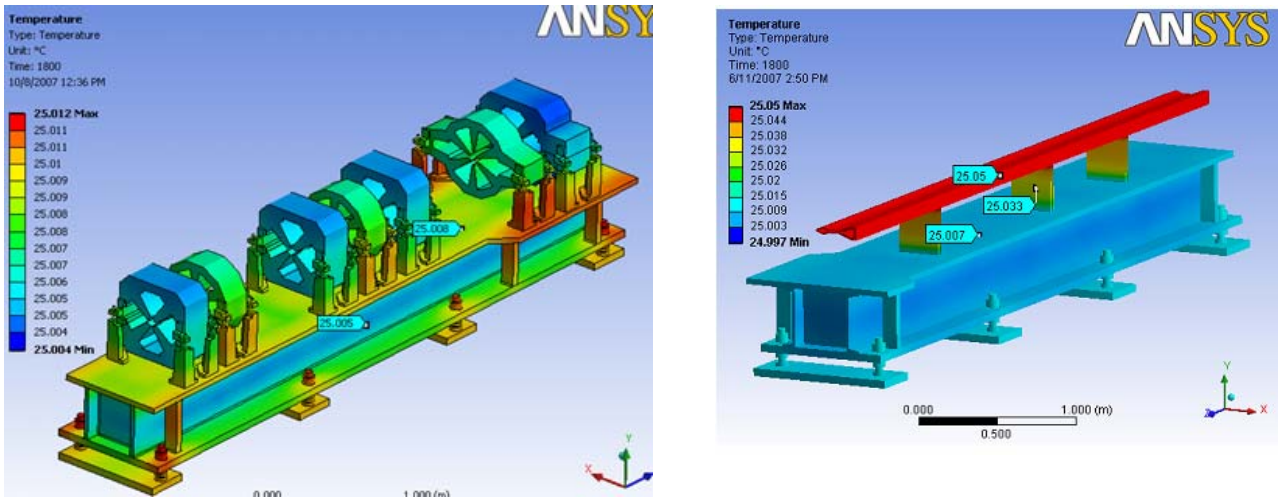

Figure.4.3.9 Temperature distribution in the girder, magnets and vacuum chamber assembly.

Vertical deformations for the girder, magnets and vacuum chamber assembly corresponding to the calculated temperature distribution are shown in Figure 4.3.10. The FEA results indicate that the RMS vertical misalignment between the magnets is 0.013 μm, which is less than the design tolerance of 0.025 μm. For the vacuum chamber, at the BPM locations next to the Invar support stands, the maximum vertical displacements are about 0.14 μm as compared to the mechanical stability budget of 0.2 μm for the chamber-mounted BPMs.

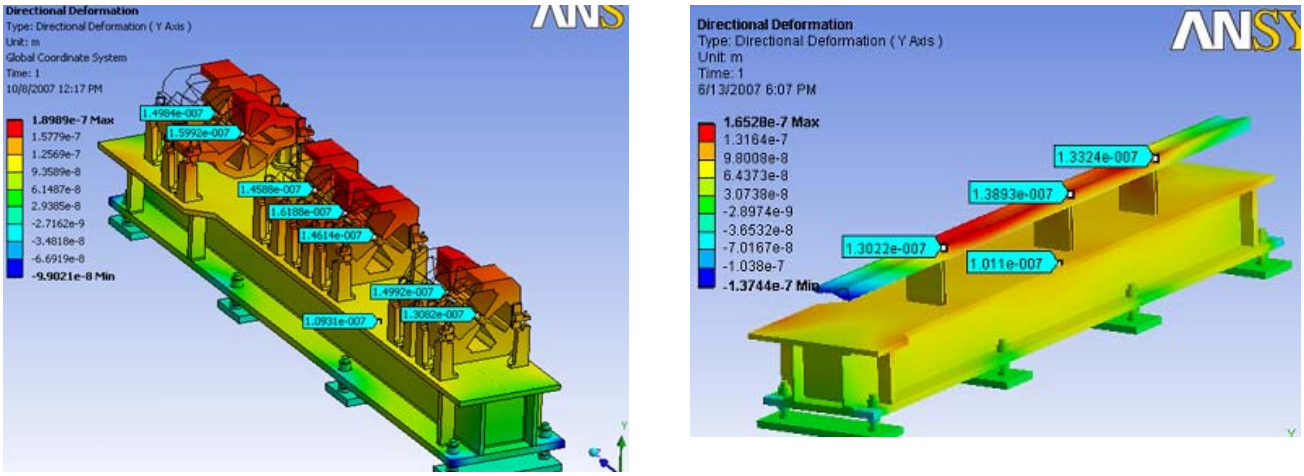

Figure.4.3.10 Vertical thermal deformations of the girder, magnets and vacuum chamber assembly.

4.3.3.9 Stability of the User BPM Support System

Compared to the chamber-mounted BPMs, the BPMs at the two ends of the insertions devices (user BPMs) as well as X-BPMS in the front ends have even more stringent mechanical stability requirements. The vertical and horizontal RMS displacements of the latter BPMs are specified to be less than 0.1 μm and 1 μm, respectively. We are considering BPM support stands made from carbon fiber composite on which the BPM blocks are supported at their mid-planes (see Figure 4.3.11). A carbon fiber composite can have thermal coefficient of expansion as low as 0.2 μm/m/ºC. With the tunnel air temperature fluctuations controlled to within ± 0.1 ºC, the vertical displacement of 1 m high support stand can be maintained to about ± 0.02 μm. The carbon fiber composites are, however, weak in the transverse (thickness) direction which can result in a system with very low natural frequency. Typical Young's moduli along the principal and transverse directions are 120 GPa and 7.5 GPa, respectively. From our preliminary discussions with vendors, we have been assured that the vendors can supply us with a 10-inch diameter carbon fiber composite that will meet the thermal design specification (< 0.1 μm) and the natural frequency requirement (> 50 Hz).

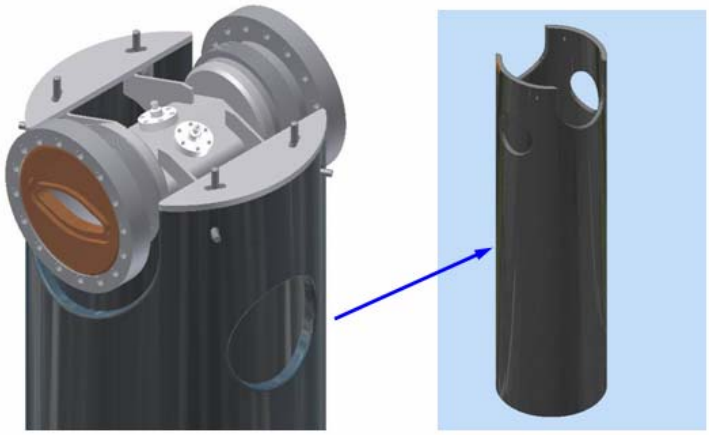

Figure 4.3.11 User BPM support stand with a BPM block mounted at its mid-plane.

A second design option for the user BPM support stands consists of a system of aluminum pipe sandwiched between two structural steel pipes. A schematic of this design is shown in Figure 4.3.12. In this design, the aluminum pipe counteracts the expansion of the steel pipes, and by carefully adjusting the lengths and diameter of each member it is possible to get zero thermal expansion at the BPM support point as indicated by the FEA thermal results (vertical displacement = 0.005 μm) shown in Figure 4.3.13.

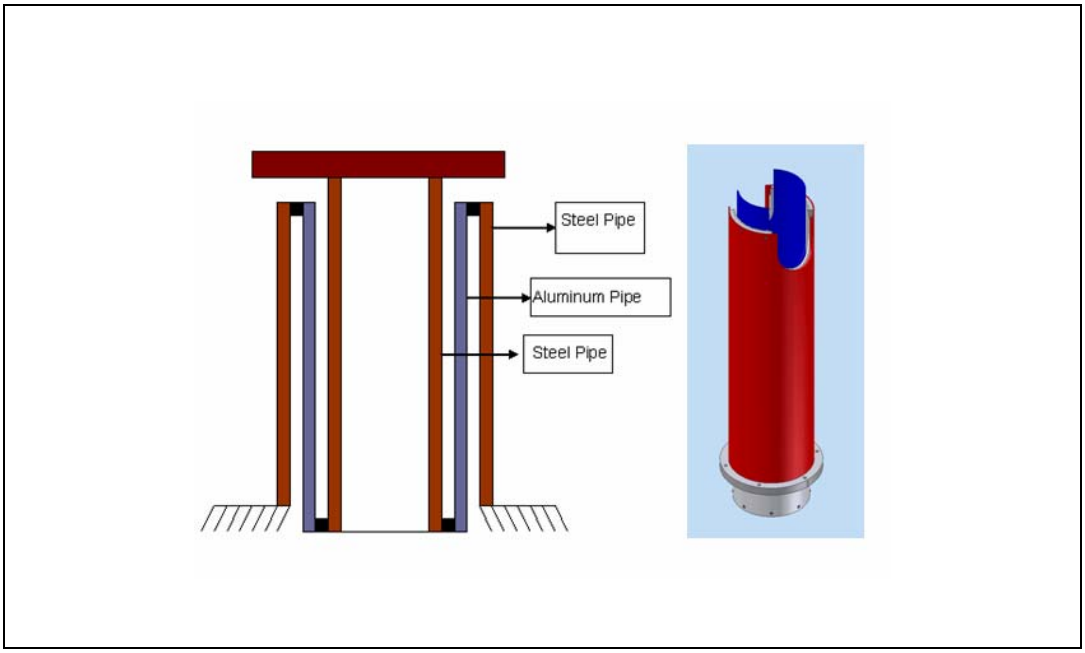

Figure 4.3.12 User BPM support stand consisting of aluminum and steel pipes

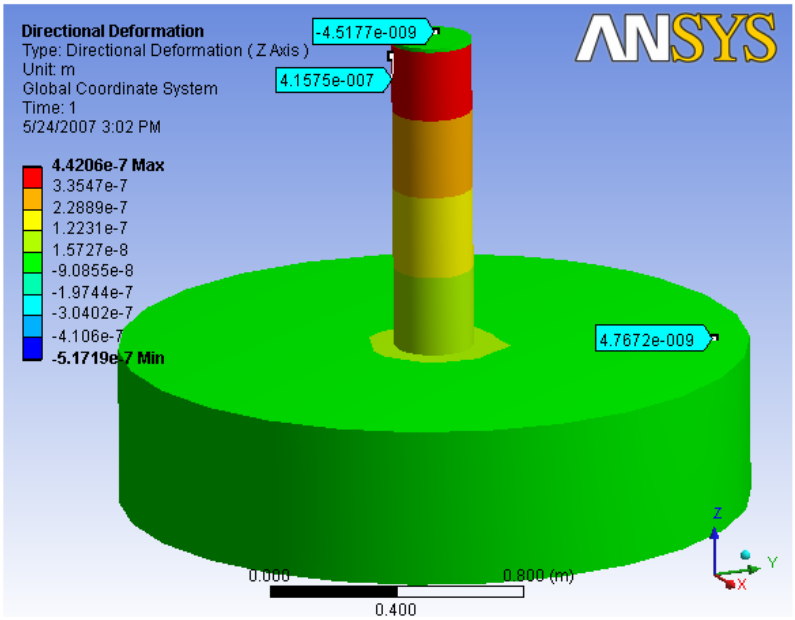

Figure 7.3.13 Maximum thermal deflection at the user BPM support point = -0.0045 microns.

Vibration FEA analysis results for this design are shown in Figure 4.3.14. The lowest natural frequency for the system is 45 Hz which corresponds to vibration (swaying) in the horizontal direction. The RMS horizontal displacement (2-50 Hz, 1σ) is calculated to be 0.026 μm as compared to the specification of 1 μm.

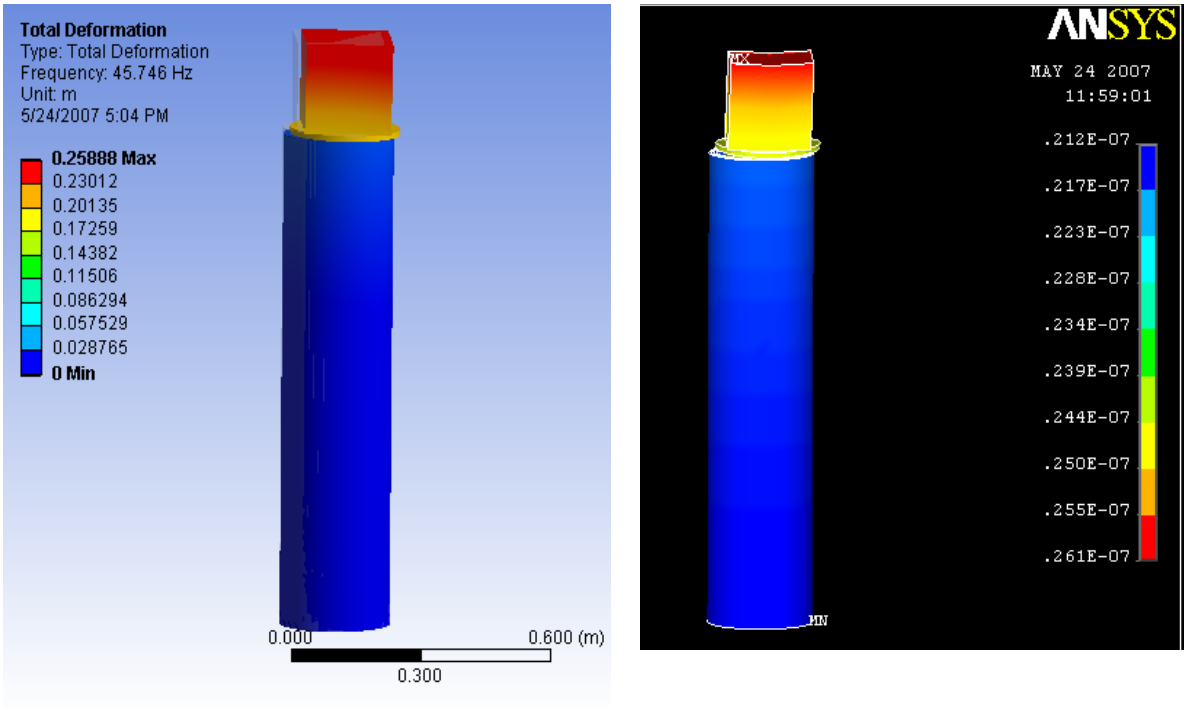

a **b**

Figure 7.3.14 **a:** Modal analysis of user BPM support stand -natural frequency = 46 Hz, **b:** Random vibration analysis of user BPM support stand-RMS displacement = 26 nm

4.3.3.10 R&D Program on Stability of the Magnet–Girder Support System

To further improve the mechanical stability performance of the girder support system, the following R&D tasks will be undertaken:

- real-time online measurements and analysis of the NSLS-II ambient ground motion.
- optimization of the stiffness of the magnet–girder assembly (A prototype assembly will be built for this purpose.)
- use of viscoelastic damping devices
- characterization and mitigation of the flow-induced vibrations of the magnets and the vacuum chambers
- investigation of the effect of process water and tunnel air temperatures on the field quality of the storage ring magnets
- assessment of insulating materials to reduce the effects of thermal transients in the tunnel

References

[4.3.1] BETA USERS' GUIDE by L. Farvacque, T.F. Gunzel, J.L. LaClare, A. Ropert.
[4.3.2] K. Tsumaki and N. Kumagai, "Vibration Measurement of the SPring-8 Storage Ring," IEEE, PAC, 2001.
[4.3.3] L. Nikitina and Y. Nikitin, private communication on ALBA girders, August 13, 2006.
[4.3.4] A. Temnykh, "The Magnetic Center Finding using Vibrating Wire Technique," CBN 99-22, Cornell University, May 26, 1999.
[4.3.5] S. Sharma, C. Doose, G. Portmann, L. Zhang, K. Tsumaki, and D. Wang, "Ground Vibration Problems at the Light Sources," 22nd Advanced ICFA Beam Dynamics, SLAC, Nov. 6-9, 2000, SLAC-WP-18, pp. 37-48.
[4.3.6] Nakazato, et al., "Observation of beam Orbit Fluctuation with Forced-Vibrating Magnets and Vacuum Chambers," MEDSI2002, Chicago, IL 2002.
[4.3.7] L. Emery, "Measurements of Thermal Effects on the Advanced Photon Source Storage Ring Vacuum Chamber," MEDSI2002, Chicago, IL, 2002.

4.4 Beam Chambers and Vacuum Systems

4.4.1 Scope

The storage ring vacuum system provides adequate and low impedance aperture for the circulating electron beam, and low pressure for long beam lifetime and low bremsstrahlung radiation. The storage ring vacuum system includes all vacuum chambers, vacuum pumps, vacuum valves, bake-out systems, and vacuum instrumentation and control. The storage ring vacuum system extends throughout the storage ring from the booster injection line-storage ring interface to the photon exit gate valve at the front end transitions to the user beamline.

During the start-up and beam commissioning of the storage ring, no insertion devices will be installed or positioned at the designated straight sections. Therefore, straight beam pipes with same cross section as the cell multipole chambers will be installed at these straight sections. Some appendage vacuum components such as rf-shielded gate valves, bellows, pumps, vacuum gauges and residual gas analyzers, will be installed at the designated straight sections together with the insertion devices after the initial beam commissioning.

Many components such as photon absorbers, beam scrappers, insertion devices, etc. require or share storage ring vacuum, but only the components whose main purpose is to maintain, monitor, and control storage ring vacuum are included in detail here. The other components are described in their respective sections.

The average pressure with beam is designed to be less than 1×10^{-9} Torr with main residue gas being hydrogen. At this pressure level, the beam lifetime due to bremsstrahlung and Coulomb scattering is longer than 40 hours. The stored beam lifetime for 500 mA operation will be limited to 2–3 hours by the Touschek lifetime due to the scattering loss of electrons in the bunch. However, localized pressure bumps will produce bremsstrahlung radiation and damage the beam line components, and have to be suppressed.

To achieve the low thermal outgassing and low photon-stimulated desorption (PSD), all the vacuum vessels and appendage vacuum components will be made from ultra high vacuum compatible materials. All the vacuum components will be carefully prepared, cleaned, and conditioned using UHV compatible processes. In-situ bake will be implemented to further lower the thermal outgassing and PSD.

4.4.2 Mechanical Design

4.4.2.1 Design Overview

There are 30 cells in the storage ring. Each vacuum cell consists of five basic chambers; an upstream matching multipole chamber, a dipole chamber, an arc section multipole chamber, a second dipole chamber, and a downstream matching multipole chamber. There are RF-shielded bellows connecting the chambers together. There is a straight section, either 6.6 m or 9.3 m long between the cells, for insertion devices and for special components such as RF cavities, injection devices, damping wigglers, and so forth. A typical vacuum cell layout is shown schematically in Figure 4.4.1. The dipole chambers are approximately three meters long and the straight chambers for the multipole magnets 3 to 5 m long. All-metal, RF-shielded gate valves will be employed to isolate each of the 30 cells and the straight sections between cells.

Most of the storage ring cell chambers will be made of extruded aluminum with a cross-section similar to that of the APS chambers [4.4.1]. Regular or bi-metal Conflat flanges with copper gaskets will be used throughout the vacuum systems, except for the flanges and seals for beam position monitor buttons, where Helicoflex delta seals will be employed. Water-cooled copper or Glidcop absorbers will be positioned in the

storage ring vacuum chambers to absorb the unused photons and heat loads, and to protect the un-cooled flanges and bellows. The entire vacuum cells will be in-situ bakeable to 130°C to remove adsorbents, such as water, and contaminants on the inner surface. Vacuum bake for the aluminum chambers will be at 120°C using pressurized hot water circulated within the cooling water channels. Alternative bakeout and conditioning approaches, such as super dry hot nitrogen flush and non-evaporable getter (NEG) strip heating, will be explored for their benefit and applicability. External heating jackets will be used for the bakeout of the appendage vacuum components.

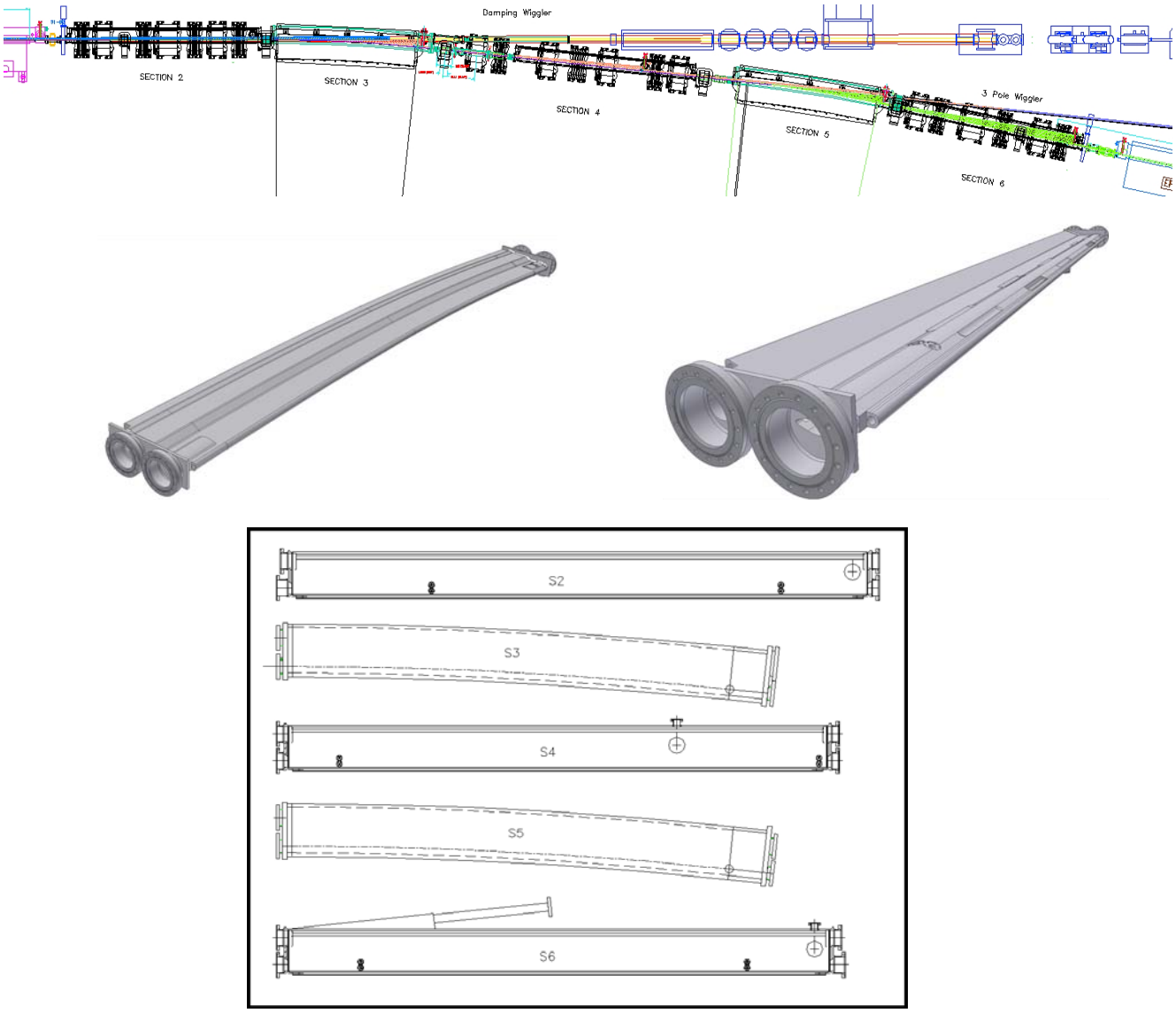

Figure 4.4.1 The layout of the five cell vacuum chambers in a typical storage ring cell with two photon exit ports; the 3D models of dipole chambers, and the arc multipole chamber; and the top view of the five chambers in each cell.

To achieve fast conditioning after intervention, sufficient pumping capacity is needed. Following rough pumping and in-situ bakeout, the vacuum cell chambers will be pumped by sputter ion pumps, non-evaporable getters (NEGs), and titanium sublimation pumps (TSP) as their main UHV pumping, The vacuum chamber design must provide provisions for stability during bakeout and with sufficient precision for accurately locating the vacuum chambers and BPM buttons after bakeout. Three chamber supports made of Invar will be employed for each cell chamber, one fixed support in the middle and two flexible supports at the

ends. The impedance of the vacuum chamber should be low enough so as not to excite higher-order mode resonances. Smooth cross-sectional transitions between components are required, as are flexible interfaces such as RF-shielded bellows between cell chambers and insertion devices.

4.4.2.2 Vacuum Chamber Design

The electron beam vacuum chambers differ according to their location within the storage ring. The vacuum chambers will provide adequate ports for heat absorbers, BPM buttons, pumps and exit ports to the front ends. A pronounced antechamber design similar to that of APS [4.4.1] will be used to allow adequate aperture for the exiting photon beams and to better distribute vacuum pumping capability. The cell vacuum chambers, as shown in Figures 4.4.2 and 4.4.3, contain two distinct but connected channels; the beam channel portion must be continuous, but the antechamber portion may be interrupted at various locations for vacuum valves, bellows, absorbers, insertion device chambers, and other devices where the mechanical requirements constrain the use of the antechamber. Ports emanating from the aluminum cell chambers will have aluminum-stainless bi-metal Conflat flanges which joint to the standard mating Conflat flanges using regular copper gaskets. The internal beam chamber cross-section will be elliptical, 25 mm vertical by 76 mm horizontal, to allow sufficient beam-to-chamber clearance, except at absorbers. The absorbers will be inserted horizontally from the antechamber side wall and positioned 22 mm to 27 mm from the beam channel center to intercept a portion of the photon fans from the bending magnets The antechamber is also sized for distributed NEG pumping and to fit within the multipole magnets.

The photon exit slot connecting the beam channel and antechamber is sized as large as possible to provide adequate aperture for photon fans and sufficient vacuum pumping conductance. However, the vertical height of this slot is restrained by magnet pole gaps and by the minimum required wall thickness under atmospheric pressure load when the chamber is under vacuum. The chamber cross sections inside the dipole, quadrupole and sextupole magnets are shown in Figure 4.4.2. There will be 2 mm clearance between chambers and magnet poles and coils at the closest points, except at corners of sextupole poles, to count in the chamber fabrication tolerances, to allow the alignment of BPM buttons and the adjustment of the chambers and supports. The extruded chamber cross sections and the cross sections after machining are given in Figure 4.4.3. The multipole chamber inside the sextupole magnets will be machined down to a minimum wall thickness of 3.1mm to accommodate the 68 mm sextupole pole gaps. The 3D finite element analysis of the stress and deflection due to atmospheric pressure load of the multipole chambers at the sextupole location are shown in Figure 4.4.4. The maximum stresses is 64 MPa, and the maximum deflections are less than 0.6 mm. The yield strength of the extruded aluminum A6063 T5 is 145 MPa, therefore providing a safety factor of > 2. The analysis for dipole chamber gives a maximum stress of 42 MPa, a safety factor of > 3, and maximum deflection of 0.55 mm.

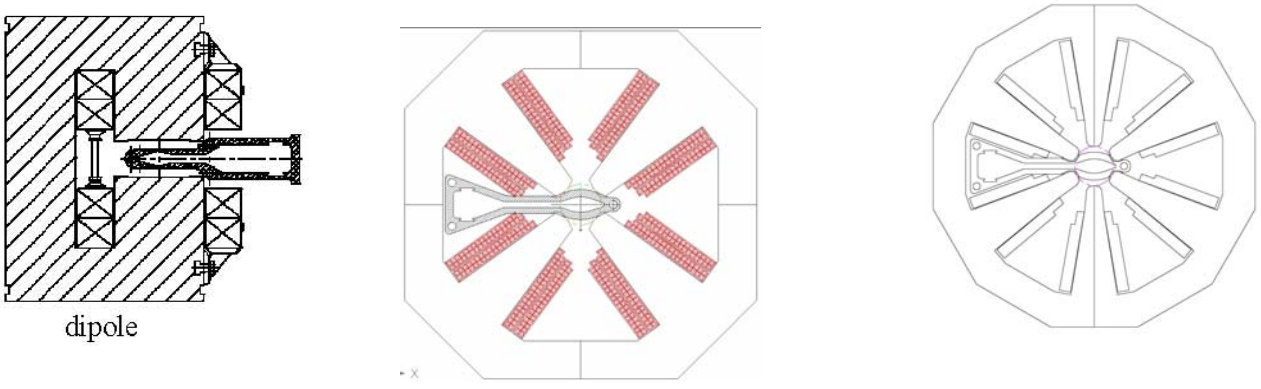

Figure 4.4.2 Storage ring vacuum chambers and magnet cross-sections at dipole, quadrupole, and sextuple interfaces. The beam channel will have an aperture of 25 mm (V)×76 mm (H). The clearance between chamber outer surface and the magnet poles will be 2 mm or more.

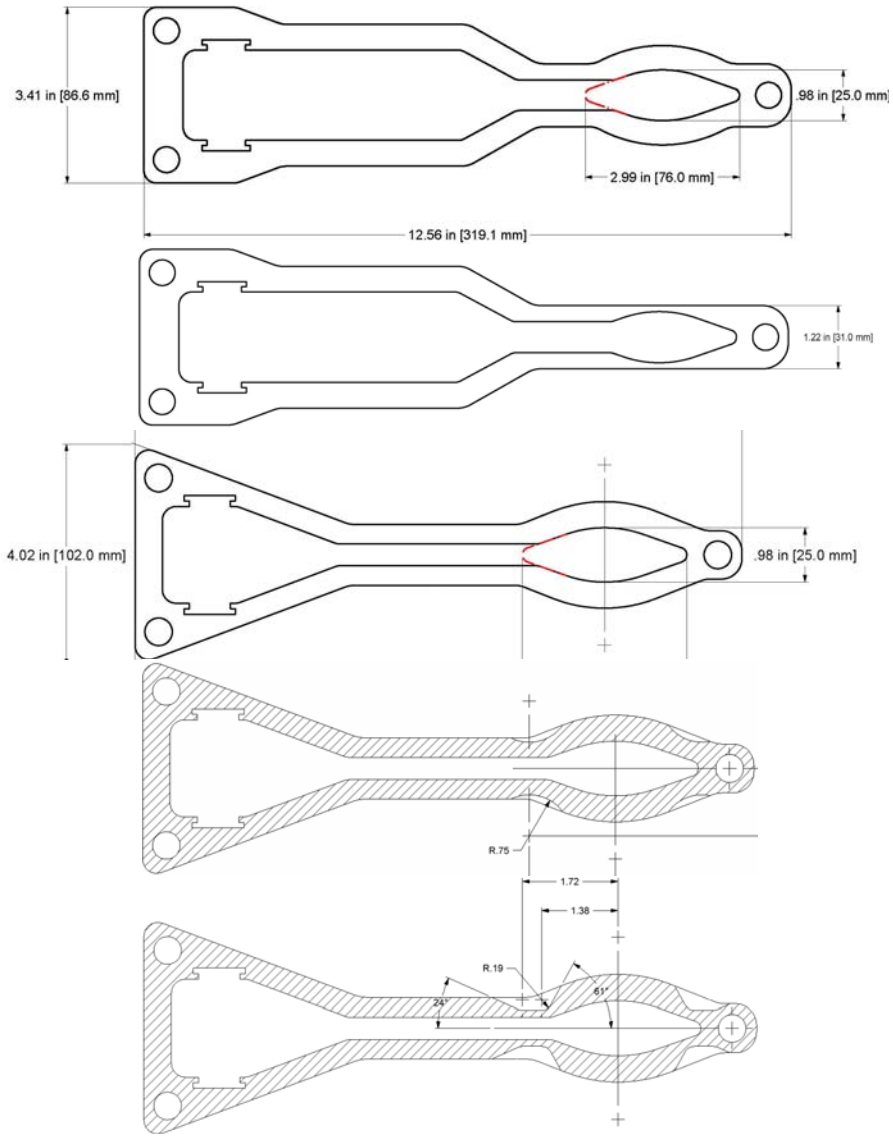

Dipole extrusion

Dipole after machining

Multipole extrusion

Multipole at quadruple after machining

Multipole at sextupole after machining

Figure 4.4.3 Storage ring vacuum chamber cross sections after extrusions and after machining, at dipole, , quadrupole, and sextupole interfaces. The minimum wall thickness at the sextupole location is ~3.1 mm, and 3 mm inside the dipole magnet.

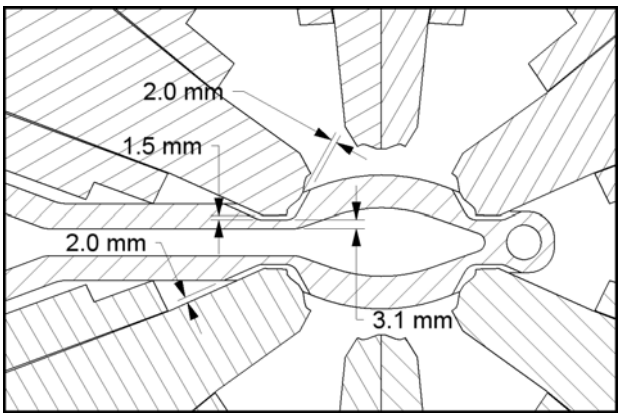

Multipole chamber cross section inside sextupole

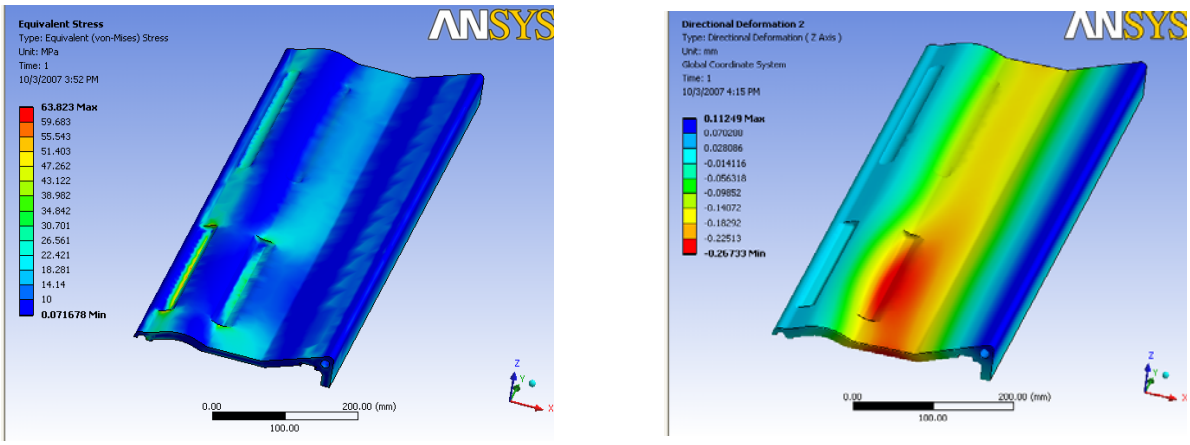

Figure 4.4.4 Top: the cross sectional view of the multipole chamber at sextupole magnet pole location: **Bottom:** 3-D finite element analysis of the deflection and stress of the multipole chamber at the sextupole pole tip locations, where the minimum wall thickness is 3.1 mm. Bottom **left:** The maximum deflection due to atmosphere pressure load is found to be 0.28 mm×2; and Bottom **right:** the maximum von Mises stress at this single point is 64 MPa, within the maximum allowable stress of 145 MPa for extruded aluminum A6063 T5.

As shown in Figure 4.4.1, there are five extruded cell chambers in each cell, named S2-S6 chambers (the straight section chambers are named as S1 chambers). The cross sections and the exact length of the cell chambers, and the locations of various absorbers within, must be developed to provide adequate apertures for both the electron beam and the photon fan, while protecting un-cooled components such as flanges and bellows. Detailed ray tracing analysis was carried out for both bending magnet radiation fans of ±52 mrad, and for damping wiggler radiation fans of ~±3 mrad. The radiation fan from other insertion devices has divergence of <<±1 mrad and will clear through the cell chambers and the connecting bellows into the front ends. Ray tracing also provides the distribution of the power and power density and the number of photons intercepted by various absorbers, allowing detailed thermal analysis of the absorbers, and pressure profile distribution in the electron beam chamber.

A portion of ray tracing at downstream end of the first bending magnet is shown in Figure 4.4.5, where ~ 40% of bending magnet fan is intercepted by the crotch absorber. Approximately 20% of the bending fan will enter the front end, together with the DW fan, through the opening in the crotch absorber. The remaining 40% of the bending fan travels downstream through the connecting bellows to S4 multipole chambers, where it is trimmed further by the two flange absorbers. The percentage of the bending fan intercepted by each absorber depends on the distance from the tip of the absorber to the beam center line, which provides

adequate protection to the downstream beam pipes, flanges, and bellows. The typical distance used for ray tracing is 25 mm; however, some are at 23 mm, 27 mm, or further, depending on the shielding requirement and dynamic aperture requirement. A list of bending radiation absorbers in a typical superperiod is given in Table 4.4.1, together with their distance from the center of the long straight, the position from the beam center, and the power and photons intercepted. The power and density are used for thermal analysis of the absorbers, while photon flux on the absorbers is used to derive pumping requirements and the pressure profile in the electron beam channel.

The DW fan passing through the crotch absorber must be clipped immediately before traveling down the front end, due to its divergence and distance (over 10 m) from the DW. This is accomplished using a DW absorber with side walls at inclined angles ~5^{o} to limit the maximum power density., and thus the temperature of the absorbers to below 300C. Depending on the canting angles of the DW, 15 – 30% radiation power (or 10 – 20 kW) will be absorbed here. The DW fan will be further clipped by fixed masks in the front end prior to entering the beamline.

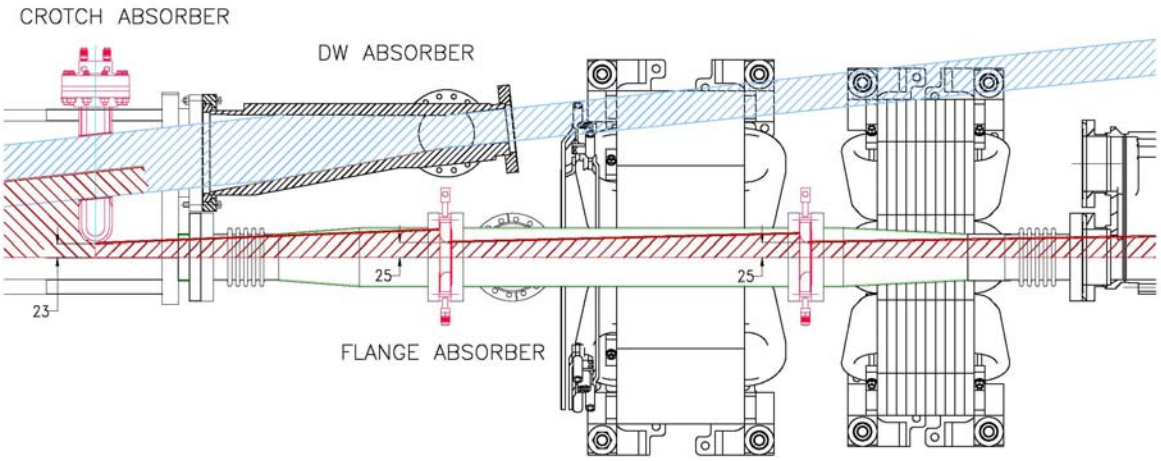

Figure 4.4.5 Chamber and absorber layout at the downstream end of the S-3 chamber (the first bending chamber), showing both the bending magnet radiation fan and the damping wiggler fan. The crotch absorber has an opening for passing the damping wiggler fan into the front end while intercepting some bending radiation.

Table 4.4.1 List of absorbers in each superperiod with their distance from the center of the long straight section, position from the beam center, angle of the bending magnet fan intercepted, total power, and the number of photons intercepted.

Section	Absorber	S	X	BM Fan	Power	# hv
#	Type	(m)	(mm)	on Absorber	3 GeV	3 GeV
S6	Stick		25	(degree)	(watt)	
S1-LS	Stick	0.00	22	0.210	84	7.1E+17
DW	Stick		37			
S3	Crotch	11.04	23	2.459	983	8.3E+18
S4	Flange	11.55	25	0.851	340	2.9E+18
	Flange	12.20	25	0.549	220	1.9E+18
	Stick	15.78	27	0.659	264	2.2E+18
S5	Crotch	20.28	25	3.611	1444	1.2E+19
S6	Stick	23.64	25	1.969	788	6.7E+18
S1-SS	Stick	24.61	22	0.086	34	2.9E+17
EPU	Stick	29.13	32	0.115	46	3.9E+17
S2	Stick	32.95	25	0.092	37	3.1E+17
S3	Crotch	36.14	23	3.366	1346	1.1E+19
S4	Flange	36.66	25	0.851	340	2.9E+18
	Flange	37.31	25	0.549	220	1.9E+18
S4	Stick	40.89	27	0.659	264	2.2E+18
S5	Crotch	45.38	25	3.611	1444	1.2E+19
S6	Stick	49.03	25	1.998	799	6.8E+18

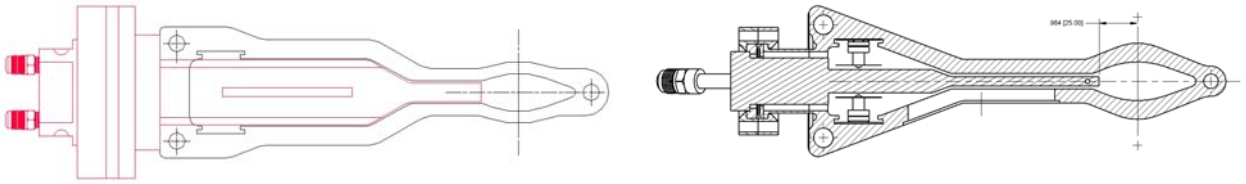

Figure 4.4.6 Conceptual design of the crotch absorbers and the stick absorbers as inserted from the side ports through the antechamber and photon exit slot. Most absorbers are positioned at 25 mm from the center of the electron beam channel, with a few positioned from 22 mm to 37 mm away.

Table 4.4.2 Types and numbers of cell vacuum chambers, absorbers, and RF-shielded bellows in the NSLS-II storage ring.

Description - Type	Length (m)	Quantity
Cell chamber – Bending – S3, S5	3	60
Cell chamber – Straight – S2	4	30
Cell chamber – Straight – S4	3.5	30
Cell chamber – Straight - S6	3.5	30
Cell – RF shielded Bellows	0.2	150
Cell - Absorber		225
ID - Absorber		45
ID chamber – EPU	~4	5
ID chamber – Damping wiggler chambers	~4	16*
ID – SRF cavity	~7	2
ID – Injection kickers + septum	~7	1
ID chamber – Empty 6.6 m straight	~5	10
ID chamber – Empty 9.3 m straight	~7	8*
ID – RF-Bellows	~0.2	~60

* Two 4 m beampipes will be used at each 9 m long straight.

4.4.2.3 Pumping at the Photon Absorbers

There are approximately eighteen photon absorbers, as listed in Table 4.4.1, in each superperiod to intercept and absorb unused photons from the two bending magnets .The absorbers are located as far from the source of the photons as practical, to reduce the power density, and thus the peak temperature on the absorber surface. Sputter ion pumps with titanium sublimation pumps (TSP) will be located at the absorbers to remove as much desorbed gas as possible, thus minimizing the amount of gas diffused back to the beam channel. The maximum gas load from bending magnet photons intercepted by each crotch absorber is estimated to be $\sim 2\times10^{-6}$ Torr-l/s, as described in Section 4.4.3.2, and can be handled with the combination of a sputter ion pump and titanium sublimation pump. The absorber for the DW radiation fan will intercept more than 10 kW of photons, resulting in a gas load of $> 3\times10^{-5}$ Torr-l/s. This high gas load at the DW absorber may be pumped by the combination of a sputter ion pump and a NEG cartridge pump, which has higher capacity than a titanium sublimation pump. Typical absorbers as inserted into the cell chambers from the side ports through the antechamber and the photon exit slot are shown in Figure 4.4.6. The crotch absorbers will be located at end of the dipole chambers where no NEG strips are present. Some stick absorbers are located in the middle of cell chambers or straight section chambers, and have to pass through the NEG strips mounted in the antechamber. Insulating coatings will be applied to the outer surface of the stick absorbers to provide electrical isolation during NEG strip conditioning and activation.

4.4.2.4 Injection Kicker Chambers

Kicker magnets require special ceramic vacuum chambers. The four ceramic chambers will be located in the injection straight section, upstream and downstream of the injection septum magnet to correct the electron beam path as needed during injection to the storage ring. These chambers will be specially designed so that they are able to 1) withstand the stresses of fast magnet actuation, 2) resist fatigue, and 3) maintain vacuum integrity. The internal surface of the ceramic chambers will be coated with a conductive film to reduce impedance for the beam image current and prevent charge buildup [4.4.2]. The film must be thin to minimize the eddy current induced by the fast-pulsing kicker field, so as not to disturb the injected beam.

4.4.2.5 Photon Exit Ports

There are two photon exit ports at each vacuum cell to extract photon beams to the user beamlines: one at straight chamber S4 for the photon beam originating from the upstream insertion device; and the second at the upstream end of straight chamber S6 for photons from the three-pole wiggler or bending magnet #2. The downstream end of these exit ports will have bending magnet photon shutters to intercept the photons before the front ends and beamlines are installed, or when the beamlines are not in use. Pneumatic gate valves will be located downstream of the photon shutters to allow vacuum isolation of the storage ring and front ends for maintenance and troubleshooting. The exit port chambers will be made of stainless steel. Sputter ion pumps with TSP will be placed at the photon shutters to remove the desorbed gas molecules. A bremsstrahlung radiation stop will be installed downstream of the gate valve prior to front end installation, to protect the equipment and personnel at the experimental floor.

4.4.2.6 RF-Shielded Bellows, Flanges, and Ports

To reduce the broadband impedance of the vacuum chamber wall and to minimize the localized HOM heating, the inner cross-section of the electron-beam chamber should be maintained as smooth as possible. High transverse impedance may cause beam instability, which might put an upper limit on the stored current. The changes in cross-sections of the beam chamber should vary smoothly, with an angle of inclination less than 1/9 for tapered transitions. The height of the steps should be less than 1 mm, in general, and less than 0.5 mm at small-aperture ducts for insertion devices. For vacuum components with cavity-like or discontinuous structure, such as flange joints and bellows, RF contact fingers will be installed to reduce the impedance and provide a smooth path for the beam image current. The opening of the thin slits of these fingers should allow enough pumping of residual gases that have been outgassed from the surface behind the slits. Calculations will be made to optimize the design of the thin slits while minimizing the impedance of the chambers. Slots or screens, if deemed necessary, will be implemented at the ion pump ports to reduce impedance and still provide adequate pumping conductance. Only commercially available RF-shielded gate valves will be used along the storage ring beam channel.

Two types of RF-shielded bellows will be studied for their finger contact force, flexibility, cost, and vacuum and RF properties: the single-finger type with hydro-formed bellows used at APS [4.4.3], and the double-finger type with welded bellows used at B-factories and a few synchrotron radiation facilities in Asia. They are shown in Figure 4.4.7. The welded bellows will allow more compression and lateral movement than the hydro-formed ones. The double-finger design may not be as reliable as the single-finger type, but does offer lower contact resistance. The magnetic permeability of both welded and formed bellows must be measured and the eddy current effect calculated, since fast corrector magnets will be mounted over the stainless steel bellows. The welded bellows will cost more than the formed ones.

Explosion-bonded bi-metal transition Conflat flanges, made from 316L stainless steel and A6061-T6 aluminum plates, will be used for the aluminum chambers throughout the storage ring. These Conflat type flanges with aluminum weld neck will be tungsten-inert-gas welded to the cell chambers using a robotic welding machine. They have the standard stainless steel knife-edge sealing face for the copper gaskets and are commercially available. They will form reliable, leak-tight joints with other bi-metal flanges and standard stainless steel flanges of adjacent chambers, bellows and other appendage vacuum components, such as vacuum pumps and gate valves. The bi-metal joints can be in-situ baked up to 250^{o}C.

a

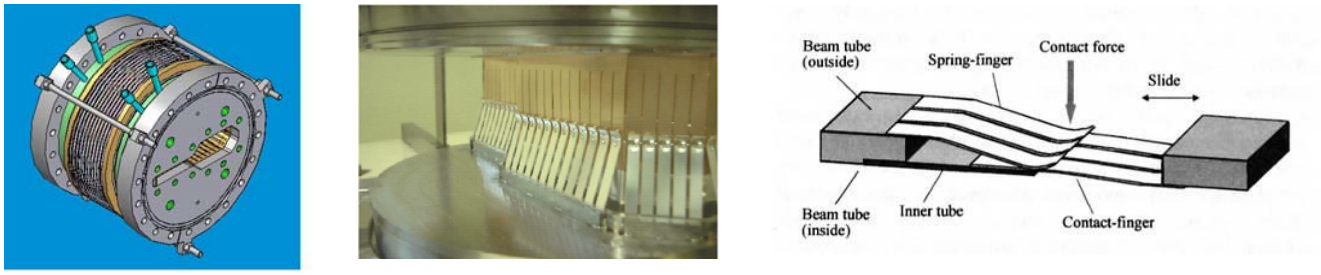

b

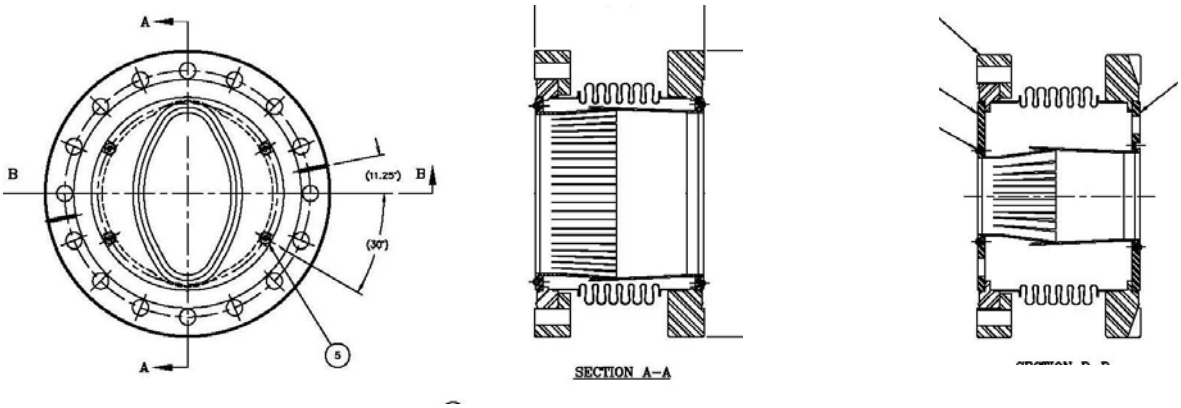

Figure 4.4.7. Two types of RF-shielded bellows: (a, upper row) the ones with welded bellows used in B-factories and BEPC-II with single or double fingers; and (b, lower row) the APS type with single fingers and hydro formed bellows.

4.4.3 Pressure Requirements and Distribution

As mentioned earlier, an average beam channel pressure of less than 1×10^{-9} Torr is needed. This pressure will provide ample beam-gas lifetime with minimal radiation and beam loss effects. Beam losses generate radiation according to electron current, energy, and vacuum pressure. At pressures greater than 10^{-8} Torr, both the stored beam lifetime and the life of many vacuum pumps will be reduced. Titanium sublimation and NEG pumps have lifetimes that are directly related to the operating pressure; therefore, maintaining this vacuum level in the storage ring improves vacuum component life, stored beam life, and minimizes the amount of radiation produced from bremsstrahlung scattering.

The beam gas scattering loss in the NSLS-II storage ring will depend largely upon the interaction of the beam with heavier residual gas molecules such as CO, CO_2, and Ar due to bremsstrahlung and Coulomb scattering. The gas density inside the vacuum chamber is determined by the installed pumping and by the surface condition of the vacuum chambers and the absorbers, which is bombarded by photons generated by the circulating electron beams. During initial ring commissioning, there are severe limitations on the achievable beam current and stored beam lifetime, caused by large pressure increases due to high photon-stimulated desorption (PSD) yield. Experience gained during early commissioning of the NSLS x-ray ring showed that residual gas spectra obtained with no stored electrons were typical of a well-baked UHV system. Hydrogen constituted approximately 95% of the residual gas at that time, and the average vacuum was in the 10^{-10} Torr range. The composition of the desorbed gases during initial operation of the x-ray ring was ~ 43% H_2, ~ 25% CO, and ~ 16% each of CO_2 and CH_4. After three months of additional beam conditioning, the

PSD rate dropped by a factor of five, and the CO, CO_2, and CH_4 peaks represented much smaller percentages of the total desorbed gas. The PSD yield versus beam conditioning dosage for copper and aluminum chambers [4.4.4, 4.4.5], as measured at NSLS, is shown in Figure 4.4.8. Typical desorption yields after 100 A.hr beam conditioning are used in the pressure simulation. The beam lifetime did not show a corresponding increase with the reduced desorption rate, mostly due to Touschek effect.

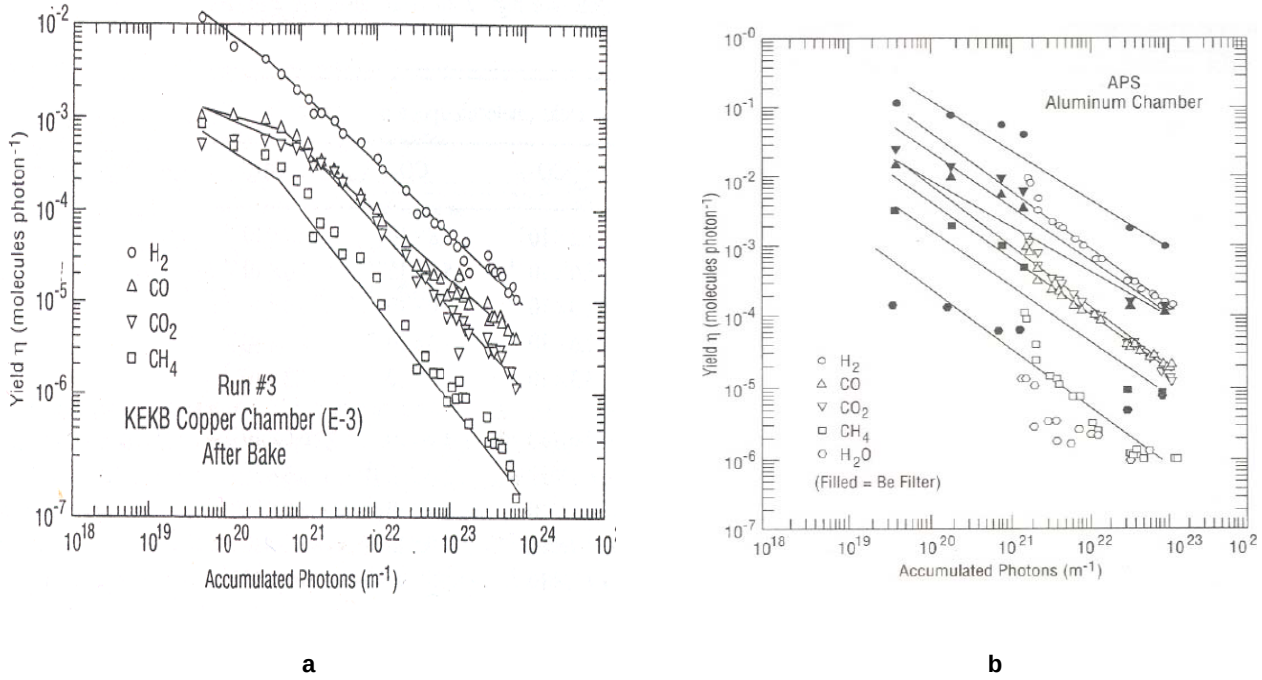

Figure 4.4.8 Comparisons of PSD yields with photon dosages for copper and aluminum. **a)** PSD yields for a 1 m pure copper sample beam chamber at KEKB. **b)** PSD yields for a 1 m extruded aluminum sample beam chamber at APS.

Most of the NSLS-II storage ring vacuum chambers will be fabricated from extruded aluminum and may be exposed to low levels of bending magnet photon radiation due to scattered photons. Almost all unused photons will be intercepted by water-cooled copper and GlidCop absorbers. After proper conditioning with photons, the PSD yields for copper, stainless steel, and aluminum will be at the same levels.

The 25×76 mm electron beam channel is vacuum pumped using distributed NEG strips in the ante chamber connected by a narrow pumping slot. Two NEG strips are installed in the extruded ante chamber and have a combined pumping speed of 240 l/s/m. The NEG pumps only chemically active gases. Sputter ion pumps (SIP) are employed to pump the inert gases not pumped by the NEGs. The SIPs are located under the photon absorbers where the majority of PSD occurs. The SIPs provide ~ 200 l/s pumping speed and are part of a combination SIP/TSP. The TSP provides an additional 500 l/s of pumping for active gases.

Linear conductance of the electron beam channel is ~ 8 l/s/m. The photon exit slot in the chamber extrusion between the ante chamber and the beam channel in dipole chamber is 15 mm high which limits the NEG pumping speed to about 135 l/s/m, in the beam channel. The slot in the multipole extrusion is 10 mm high, which yields a conductance of approximately 45 l/s/m in the beam channel.

4.4.3.1 Static Vacuum: Thermal Outgassing

The static pressure distribution in the storage ring will be determined by the amount of thermal outgassing from the internal surfaces in the vacuum chambers. These outgassing rates will depend on the construction

materials used and their preparation. After precision cleaning, the chambers will be vacuum-baked and may be glow-discharge conditioned to reduce outgassing and remove contaminants prior to their final assembly into the storage ring magnets and girders. All the chambers and vacuum components in the vacuum cell will be in-situ baked, to reduce the thermal outgassing as well as the PSD yields. Most of the internal vacuum surfaces along the storage rings are aluminum. The contribution of other materials to the thermal outgassing load is much smaller than that of aluminum wall. Vacuum-baked aluminum outgassing of 1×10^{-12} Torr-l/s/cm^2 is used for thermal gas load modeling. The thermal gas load is estimated to be 1×10^{-8} Torr-l/s/m.

4.4.3.2 Dynamic Vacuum: Photon Stimulated Desorption

During operations with stored electrons, specially designed water-cooled Glidcop absorbers will intercept most unused synchrotron radiation. The PSD rate η for vacuum-baked copper and Glidcop has been studied at NSLS [4.4.4] and at other laboratories. An η value of 1×10^{-5} molecules per photon is used for the modeling calculations [4.4.6]. The total photon flux from the storage ring dipole magnets is calculated using Np (ph/s) = $8\times10^{+20}$ [E(GeV)] [I(Amperes)]. For 3 GeV and 500 mA, the total photon flux is $1.2\times10^{+21}$ ph/s. Using these values and converting to gas load yields 3×10^{-4} Torr-l/s (or ~5×10^{-6} Torr-l/s per bending magnet). The undulator radiation will have a narrow fan. It will mostly be collimated and intercepted down at the front end and beamline, and will produce little gas load to the storage ring beam channel. In contrast, the damping wiggler radiation will have a relatively wide fan. Approximately 15% of the DW radiation will be intercepted by the crotch absorber located upstream of the S4 multipole chamber, equivalent to ~$1\times10^{+20}$ ph/s by each DW. Assuming the same η value of 1×10^{-5} molecules per photon, this corresponds to an additional gas load at photon exit port of 3×10^{-5} Torr-l/s from each DW.

4.4.3.3 Dynamic Pressure Distribution

The pressure rise with beam operation will be determined by the PSD of gases from internal surfaces of the vacuum chamber, and the amount of dynamic pumping. Most synchrotron radiation will be intercepted by water-cooled Glidcop absorbers,. The pressure distributed in a super-period of 52 m was calculated using both Molflow [4.4.7] and Vaccalc [4.4.8] software. The storage ring pressure distribution in the beam channel with with no beam current,, with 500 mA stored beam current, and with damping wigglers is plotted in Figure 4.4.9. PSD yield of 1×10^{-5} mol/ph, reached after approximately 100 amp-hours of beam conditioning, is used in the calculation. The design average pressure of less than 1×10^{-9} Torr can be reached with the current pumping scheme of distributed NEG, lumped ion pumps, and TSP. However, the DW absorber, as shown in Figure 4.4.5, does produce a sharp, but localized peak up to 10 nTorr, assuming 15% of the DW radiation be clipped here. The pressure peak will be proportionally higher if more DW fans are to be clipped here. The significant increase in bremsstrahlung radiation at this location could damage the downstream equipment and may require additional shielding. The importance of the distributed pumping by NEG strips is clearly illustrated in Figure 4.4.10. The reduction of the lumped pumping speed at the absorbers from 500 l/s to 100 l/s, due to long manifold or saturation of TSP film, only increase the average pressure by two folds. The average pressure increases by over ten folds when the NEG strip pumping is eliminated, perhaps due to saturation or fails to activate. To further illustrate this point, the NEG strips at short straight are left intact in the simulation, which generate a local pressure of ~ 0.1 nTorr.

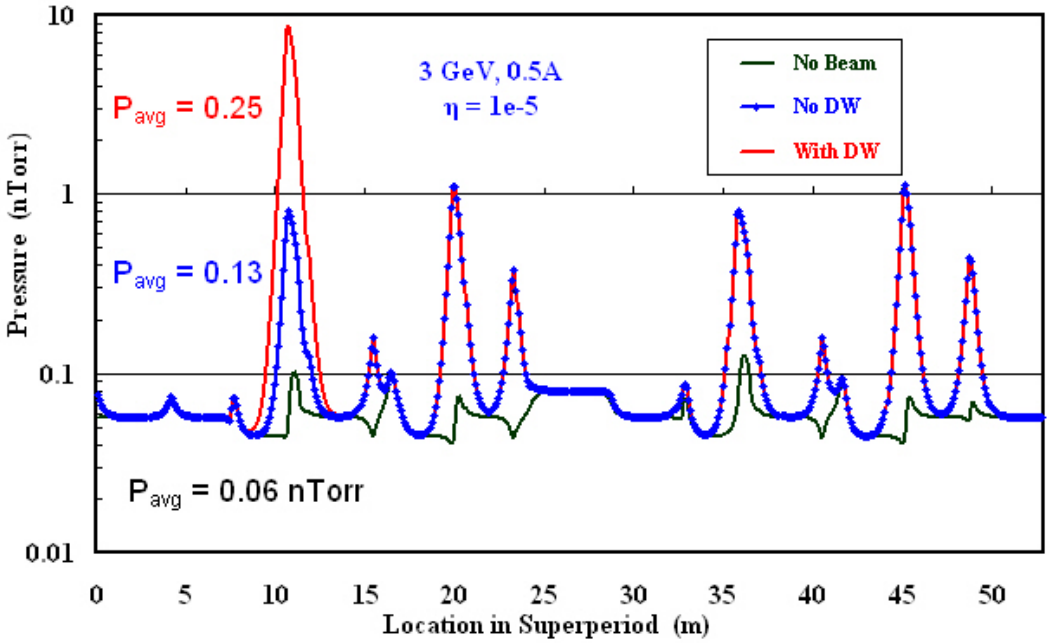

Figure 4.4.9 Pressure distribution inside the electron beam channel in one superperiod, without beam (black), with 500 mA (blue line and circles) ,and with damping wigglers (red line). The average pressure is about 0.1 nTorr without damping wiggler, ~ 0.3 nTorr with damping wiggler. However, the localized pressure at wiggler absorber is peaked at 10 nTorr.

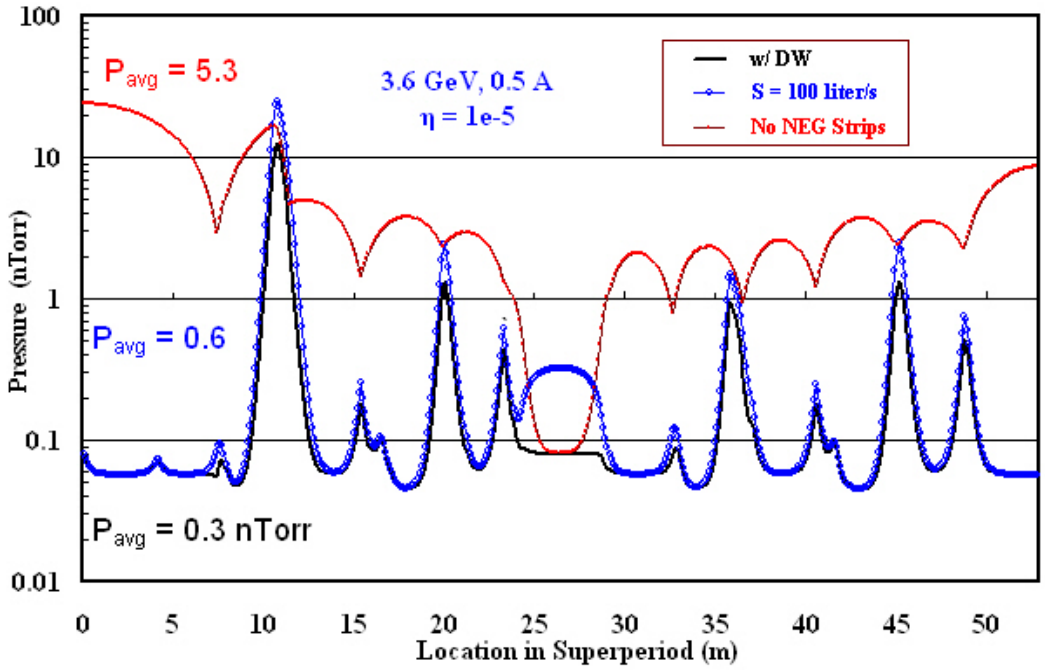

Figure. 4.4.10 Pressure distribution inside the electron beam channel in one 52 m superperiod with damping wigglers. The blue curve represents the pressure when the lumped pumping speed (IP+TSP) at absorbers is reduced from 200 l/s to 100 l/s. The red curve is when the NEG strips are not activated and the average pressure exceeds 5 nTorr.

4.4.4 Vacuum Chamber Materials, Fabrication, and Treatment

Most of the storage ring vacuum chambers will be constructed from extruded A6063-T5 aluminum. This alloy was selected based on a comparison of various properties for commonly used vacuum chamber materials for electron storage rings, as described below.

4.4.4.1 Selection of Chamber Materials

There are three common UHV materials suitable for the vacuum chambers of the electron storage ring: stainless steel, aluminum alloys, and OFHC copper, with stainless being preferred for a few new SR facilities in Europe, and aluminum for the new ones in Asia and the U.S. Copper was chosen for storage rings with high energy and high power density, such as the B-factories at SLAC and KEK, and also for its high thermal conductivity and radiation shielding properties. However, copper has the disadvantages of high material and fabrication costs. For the 3 GeV NSLS-II, radiation shielding and thermal conductivity requirements are not as critical as in the higher energy machines. Moreover, most synchrotron radiation from bending magnets will be removed by discrete copper or Glidcop absorbers. Therefore, copper has not been considered a preferred chamber material. The choice between stainless and aluminum for the NSLS-II cell chambers is based on experience at NSLS and APS, plus aluminum's vacuum and mechanical properties, ease of fabrication, and relatively reasonable cost.

One major difference between NSLS-II and other new SR facilities of comparable energy is the large bending magnet radius. The photon fan from the bending magnet will have a small dispersion and will be easily intercepted by discrete absorbers. This allows a narrow chamber geometry design; therefore, the cell chambers can be fabricated from extruded aluminum with uniform cross-sections. The need to accommodate the distributed NEG pumping also favors extruded aluminum, since an antechamber can easily be produced by aluminum extrusion. The cost of extrusion is considerably lower than that of chambers made of stamped stainless plates or machined aluminum plates, although the cost of machining the external chamber profile to fit the magnet poles and the various access ports will be significant. A few important arguments concerning the choice of material are listed and further discussed below.

Table 4.4.3 Electron Storage Ring Chamber Materials and Their Critical Properties.

Specifics	Aluminum	Stainless	Copper
Initial PSD rate	High	Low	Average
Mechanical strength	Acceptable	Excellent	Good
Thermal expansion	Large	Small	Small
Thermal conductivity	Excellent	Poor	Excellent
Weldability	Good	Excellent	Good
Beam impedance	Low	High	Low
Bi-metal flanges	Yes	No	Yes
Cooling channels	Extrusion	Brazed	Brazed
Fabrication cost	Low	Average	Expensive
Ease of in-situ bake	Good	Poor	Good
Radiation shielding	Poor	Average	Excellent

The outgassing of unbaked aluminum is higher than that of stainless, but an in-situ baked aluminum surface has similar or lower outgassing than that of stainless. The initial PSD rate of an aluminum surface is higher than those of copper and stainless. However, aluminum conditions faster and will reach the same PSD rate at a modest integrated beam dosage. The high thermal conductivity of aluminum offers distinct advantages over stainless, both during the in-situ bake and during normal operation. No conductive coatings or strips are needed on aluminum to reduce the chamber wall impedance, whereas stainless chambers may need copper strips and absorbers in certain locations and for mis-steered beam. Therefore, our preferred

material to form the cell chambers through extrusion is aluminum A6063-T5 alloy. Stainless-to-aluminum bi-metal Conflat flanges will be welded to the aluminum chambers, and standard copper seals can be used to form reliable joints between the chambers, bellows, and appendage components.

4.4.4.2 Vacuum Facility

To ensure the necessary chamber surface properties, cleanliness, mechanical quality, and leak tightness, vacuum facilities will be needed for cleaning, welding, assembling, and evaluating the vacuum chambers and other vacuum components for the storage ring and injectors. A dedicated chemical cleaning facility is required to clean the long chambers and other vacuum components. It will consist of four long, stainless steel tanks and a gantry crane capable of handling chambers up to 6 m long and 200 kG in weight. These tanks will provide ultrasonic cleaning with hot water, commercial bio-degradable cleaning agents, and de-ionized water rinse, and are suitable for aluminum, copper, inconel, and stainless chambers and materials. The exact cleaning recipe and process will be based on the chamber material and experience developed at other SR facilities such as NSLS and APS. Programmable robotic welding stations with laminar flow hoods will be set up to weld the cleaned chambers, the sub-assemblies, and the flanges. A Class 1000 clean room with ~100 m^2 floor space is needed for the assembly of the chambers with distributed NEG strips, ion pumps, gauges, absorbers, BPM buttons, and other components.

A facility with these capabilities was established at Argonne National Laboratory for the construction of the Advanced Photon Source. The NSLS-II project plans to use the ANL/APS facility for the production, chemical cleaning, and automatic welding of the cell chambers of the NSLS-II vacuum system. Should this prove impractical for some reason, equivalent facilities will be established at BNL. Even if the ANL vacuum facility is utilized, a small chemical cleaning facility is still needed at BNL for storage ring and beamline vacuum components. The clean room and vacuum bakeout/evaluation stations are still required at BNL for the final assembly and evaluation of the cell chambers. If we do not utilize the APS facility and need to establish all of the capabilities at BNL, then ~2,000 m^2 of space would be required. If the ANL facility is used for production, cleaning, and welding, then ~1,400 m^2 would be required. Building 905 at BNL has been identified as the preferred location for the BNL vacuum facility. This building has more than 2,500 m^2 of space, as well as overhead cranes, and is available for use by the NSLS-II project.

4.4.4.3 Fabrication, Assembly, and Evaluation

Most of the storage ring chambers will be made of extruded aluminum. Immediately after extrusion, the long chamber sections will be stretched to obtain the uniform cross-section and to meet the dimensional requirement. They will then be cut to the designed length. The bending chambers will be formed to the curvature on a hydraulic press with dies or rollers of correct radius. To preserve the internal cross-sections, the inner volume of the bending chambers will be filled with DI water and frozen prior to the bending/forming operation. The extruded chambers will be machined at industrial vendors to the appropriate external profiles and to add photon exit ports, access ports for BPM buttons, pumps, absorbers, and other vacuum components. The chambers will then be cleaned at the chemical cleaning facility and sealed in an aluminum bag filled with dry nitrogen gas for storage and further processing.

The aluminum chambers and flange adaptors are welded together with tungsten-inert-gas welding processes, using programmable robotic welding machines. The relative humidity of the laminar hoods over the welding zones will be reduced to less than 50% during welding to minimize oxide growth at the heat zone and to ensure weld integrity. Following welding, the vacuum chambers will be pumped down with a turbomolecular pump (TMP) backed by a dry mechanical pump, then checked for leaks using a leak detector with minimum helium sensitivity of 5×10^{-11} Torr-l/s. Specific procedures for repairing each type of weld leak will be developed to ensure that the quality of the chambers is not compromised. The cooling water channels will be leak-checked with vacuum and by sniffing while pressurized. The welded chambers are then brought

into the Class 1000 clean room for assembly of peripheral components, such as BPM buttons, NEG strips, pumps, absorbers, and gauges. The chamber end flanges will then be capped with blank flanges.

The assembled chambers will be installed at the evaluation stands for final leak checking and bakeout at 130^{o}C using temporary ovens. The vacuum level and the residual gas composition will be closely monitored during the bakeout, using vacuum gauges and residual gas analyzers (RGA), to ensure that the chambers remain leak-tight and are free of contaminants. All the pumps, gauges, BPM buttons, absorbers, and thermocouples are to be activated and measured to ensure their proper operation during and after the bakeout cycle. The possible use of a DC glow-discharge system to clean internal surfaces with an Ar/O_2 mixture during bakeout will be investigated for its merit versus the technical complexity and cost. After bakeout, the chambers will be either at storage vacuum or back-filled with dry nitrogen for the subsequent assembly into magnets/girde and installation in the SR tunnel.

4.4.4.4 Installation, Alignment, and In-Situ Baking

During the machining of the vacuum chambers, all mounting holes for the survey fiducials will be checked against the beam channel cross-sections and the BPM mounting surfaces. To ensure precision alignment, the design of the vacuum chambers and the proposed alignment schemes will be reviewed and approved by the diagnostics, accelerator physics, and alignment and support groups. The required precision of the chamber alignment is ≤0.5 mm in general, and ≤0.1 mm for special parts such as the BPM buttons. The assembled and tested chambers will be installed into the split magnets and aligned using built-in adjustment bolts of the fixed support plates mounted on the girder. After the installation and alignment of individual chamber/magnet girders in the tunnel, the end capping flanges will be removed and the RF-shielded bellows will be installed and connected to the next cell chambers. Two sector gate valves will be mounted and supported on the end flanges of the S2 and S6 chambers of each cell. The magnet buses, cooling water lines, and vacuum equipment cables will then be connected prior to final measurement, pump down, leak check, and in-situ bakeout.

The in-situ bakeout of the storage ring cell in the tunnel will be carried out with pressurized hot water provided by the storage ring utility system. Additional heating jackets, heating tapes, and thermal insulation are needed for large appendage components, such as gate valves, ion pumps, etc., to ensure uniform temperature distribution, especially at large flange joints where uneven temperatures may result in seal failure and vacuum leaks. The supports for the chambers and the pumps must be adjusted to allow thermal expansion during the bake, while still maintaining and protecting the mechanical stability of the entire system. Three Invar plates, one fixed in the middle and two flexible at the ends, will mount and support each cell chamber on the girder. The storage ring cell will be pumped down with a turbomolecular pump backed by a dry mechanical pump during the bakeout. The vacuum level and gas composition will be continuously monitored using cell vacuum gauges and RGAs during the bakeout. The temperature of the chambers will be raised slowly by the hot water system and the heating jackets, and controlled by the bakeout programmable logic controller with inputs from the installed thermocouples on the chamber surface. The entire vacuum cell will be baked at 120°C for ~ 40 hours to remove absorbed water and other contaminants from the surfaces. The sputter ion pumps, the titanium sublimation pumps, the NEG strips, and NEG cartridges will be degassed during the bake, then activated during the ramp down of the bake. The bakeout of the whole cell will be completed in ~3 days, from Day 1 to Day 3, and can be comfortably fitted in a normal work week while still leaving sufficient time for any necessary remedial actions. The vacuum cell will be leak-checked again after the bake, using the cell RGA. The fixed support points on the chambers will be checked and adjusted to their original positions by the survey group to ensure that all the critical components, such as the BPM buttons are properly aligned.

4.4.5 Storage Ring Vacuum Pumping

The types and sizes of the pumps to be used at NSLS-II will be standardized throughout all the machine areas as much as possible, to lower the unit cost and to ease routine maintenance in the future. The selection of the pumps will be based on the experience gained from existing pumps used in NSLS and other similar SR facilities.

4.4.5.1 Roughing Pumps

A set of TMPs backed by dry mechanical pumps will be used to rough down the vacuum section from ambient pressure to high vacuum, and during in-situ bake before turning on the in-line ultra high vacuum pumps. The TMPs will be connected to the vacuum sections through small, manually operated, all-metal angle valves. TMPs with magnetic or ceramic bearings of ~100 l/s size backed by dry pumps of ~5 l/s are deemed sufficient, since the ultimate pumping speed at the vacuum chambers is limited by the conductance of the chambers, the angle valve, and the flexible hose. TMPs will be manually valved out once the sector reaches ultra high vacuum. Each of the TMP stations will be equipped with vacuum gauges and electro-pneumatic valves to quickly and effectively isolate the TMP from the vacuum section in the event of pump or power failure. A dozen TMPs will be needed during the first phase of NSLS-II construction for component testing and leak checking. These TMPs, due to limited operating lifetime under heavy usage, will be replaced with newer models during NSLS-II commissioning and operation. A list of TMPs required for the operations at the storage ring is given in Table 4.4.4.

Table 4.4.4 List of Vacuum Pumps and Gate Valves for the Storage Ring and Font Ends.

	IP 200 l/s	TSP 500 l/s	NEG Lumped 500 l/s	NEG strips*~100 l/s/m	TMP portable	Gate valves
SR	150	150	60	150	10	60
Exit port	60	60	0	0	4	60
ID	60	60	60	27	4	
Total	270	270	120	177	18	120

*Each chamber will have a pair of 3–5 m NEG strips for a total length over 1 km.

4.4.5.2 Ultra High Vacuum Pumps

After initial rough down and in-situ bakeout of the vacuum sectors, the system pumping will be transferred from TMPs to ultra high vacuum pumps, including SIPs, TSPs, NEG cartridges, and NEG strips. TSPs and NEGs have high pumping speed for active gases such as CO, CO_2, H_2O, and H_2 with equilibrium pressure down to 10^{-12} Torr; they, however, will not pump inert gases (CH_4, C_2H_6, etc.) nor noble gases (He, Ne, Ar, …). Sputter ion pumps will remove inert and noble gases as well as active gases.

Triode-type SIPs have better pumping speed for noble gases, but they tend to have higher leakage current and are harder to rebuild after electrode saturation. A few noble diode SIPs, with tantalum cathode plates and similar pumping speed as triode pumps for noble gases, will be used to supplement the regular diode-type SIPs, thus avoiding so called “argon instability.” Ion pumps of 30 l/s and 200 l/s will be used throughout NSLS-II, with the 30 l/s pumps used at conductance-limited areas such as booster synchrotron and beam transport lines; and the larger pumps at SR absorber and shutter locations. These SIPs will have large anode cells to retain sufficient pumping speeds down to the 10^{-10} Torr range. A DESY-style high-voltage feedthrough, which is less prone to radiation-induced corrosion at the brazing joint, will be used for the ion pumps. Commercial dual ion pump controllers with local and remote capabilities will power and monitor the SIP, by interfacing with the PLC and control computers, through hard wires and Ethernet linkage, respectively. Ion pump currents will supplement the vacuum gauges to provide pressure distribution over the whole ring. However, due to the buildup of leakage current in the ion pump elements, the reliable pressure

reading from ion pumps is limited to the mid 10^{-10} Torr range. A list of ion pumps for the storage ring is given in Table 4.4.4.

The large volume of active gases desorbed from the photon absorbers can be efficiently removed from the SR by localized TSPs of ~500 l/s, thus minimizing the quantity of gases diffused back to the electron beam channel. Alternatively, at absorbers for damping wigglers, with a modest increase in cost, TSPs may be replaced with NEG cartridges of comparable pumping speed but higher capacity before needing reactivations. Both TSPs and NEGs can be activated and reactivated locally or remotely. However, TSPs have the advantage of only generating a brief gas burst during their short sublimation period, while NEG activation takes longer, during which time a large amount of hydrogen is produced and should be removed by portable TMP stations.

Distributed NEG pumping in the form of NEG strips, similar to those employed at the APS storage ring, is planned for use in all cell vacuum chambers. This is deemed efficient to provide linear pumping to the beam channel through the photon exit opening. Dual strips will be mounted on the top and bottom of the antechamber. There will be sufficient clearance between the two mounted NEG strips to allow the passage of photons, even when a beam mis-steers, and for the insertion of stick absorbers. The mounting of the dual strips will be carefully designed and thoroughly tested to eliminate any potential electrical faults during in-situ bake and NEG activation. The NEG activation is at 400^{o}C for 30 minutes and will be achieved with resistive heating of the NEG strips with ~70 ampere current, carried out at the end of in-situ bakeout or during the machine maintenance period. The two NEG strips together will provide more than 240 l/s per meter pumping speed for active gases such as CO and H_2 even after pumping ~0.1 Torr-l per meter of active gases, corresponding to a few months of beam operation at 10^{-9} Torr pressure.

Some of the ID vacuum chambers will have very small gaps of a few mm, resulting in very limited linear conductance. In these cases it is not effective to simply rely on the lumped pumps located at both ends of the chamber. Sputter-coated NEG thin film has been applied to the inner surface of ID chambers at several SR facilities, notably at ESRF, where over 20 ID chambers have been coated and in operation for more than 5 years, and at Soleil, where most straight chambers have been NEG coated. For narrow-gap undulators at NSLS-II, NEG coating will be considered during the design stage; if appropriate, it will greatly simplify the pumping system design. For long straight sections that are not occupied by insertion devices, distributed NEG strips together with ion pumps and titanium pumps will be installed to maintain ultra high vacuum.

4.4.6 Vacuum Measurement and Control

4.4.6.1 Monitoring and Control Methodology

The vacuum level in the storage ring, the front ends, and the beamlines will be monitored and interlocked with the ion pump current and with vacuum gauge readings. Residual gas analyzers will also be used for online monitoring and diagnosis. Each vacuum sector will have a convection-enhanced Pirani gauge and two ionization gauges as the primary vacuum gauges. Additional vacuum gauges will be installed to protect the RF cavities and kickers. Vacuum devices such as gauge controllers, ion pump controllers, and RGA - with local and remote capabilities - can be operated through front-panel switches. Their communication with the equipment control system will be through RS232 or Ethernet links for remote monitoring and control. It is anticipated that most of the vacuum controllers will be off-the-shelf items purchased through competitive bids from qualified vendors.

Due to the high level of radiation in the SR tunnel, controllers for vacuum systems will be placed in satellite electrical racks located at mezzanine above the storage ring tunnel. Electrical power for vacuum diagnostics and controllers will be standard 115 VAC and 60 Hz. Since vacuum pumps and associated vacuum equipment surrounding the ring vacuum chambers are subjected to synchrotron and bremsstrahlung radiation, radiation-resistant cables and appropriate routing will be employed to minimize radiation damage.

4.4.6.2 Vacuum Gauges

One primary vacuum gauge, a convection-enhanced Pirani gauge, will be installed in each vacuum sector to provide pressure readings ranging from atmospheric pressure down to 10^{-4} Torr. It will also be used for other vacuum equipment protection and interlocking. Two ion gauges, either Bayard-Alpert ion gauges or inverted-magnetron cold cathode ion gauges, will be installed at each SR vacuum section as the primary UHV gauge. The same type of ion gauge will be used for injectors, beam transport lines, front ends, and user beamlines. Both types of ion gauges have a useable pressure-sensing range down to 10^{-11} Torr and they have been implemented successfully at various synchrotron radiation facilities. CCGs have the advantage of overlapping the lower end of the Pirani gauge range and can be operated through long cables for signal transfer, thus eliminating the needs of locating electronics nearby. CCG tubes do not have built-in hot filaments and are therefore less susceptible to mishandling and filament breakage during startup and commissioning. The accuracy of CCG readings is normally at ±50%. Moreover, it is difficult to degas CCGs once they are contaminated. CCGs are still our choice at this point in the design process. The numbers of vacuum gauges in each area of the storage ring are listed in Table 4.4.5.

Table 4.4.5 Number of Gauges and Residual Gas Analyzers in Areas of the Storage Ring.

	TCG*	Ionizing Gauge	Residual Gas Analyzer
SR	30	60	34
Front end	30	60	60
ID	30	60	10
Total	90	180	104

*TCG = convection-enhanced Pirani gauge

Interference with the gauge readings due to the presence of copious electrons, photons, and photoelectrons has been observed at many SR facilities. Therefore, if practically achievable, the gauge tubes will be mounted on elbows at shielded ports on the antechambers to minimize interference and erroneous pressure readings. The gauge tubes will also be installed in areas with minimal stray electrical and magnetic fields. Radiation-hardened material such as Kapton-insulated cables will bridge the short distance between the chamber gauge ports and the cable tray to ensure system reliability. Kapton cables are bakeable up to 200^{o}C. Microprocessor-based multi-gauge controllers will be used to power the vacuum gauges and to provide system monitoring and control through RS232 or an Ethernet bus. The gauge controller will be hardwired to PLCs to interlock gate valves, other beam components and subsystems.

4.4.6.3 Residual Gas Analyzers

Quadrupole-type RGAs will be installed to measure the partial pressures of residual gas species at selected locations in the injectors, storage ring, front ends, and user beamlines. Their use will help to identify sources of residual gases, including photon-desorbed gas from chamber walls and absorbers, air leaks, cooling water leaks, oil back-streaming, specialty gases back-streamed from the beamlines, and other contaminants. RGAs, with electron multiplier, will have partial pressure sensitivity down to the 10^{-13} Torr range. Due to the high cost, RGAs may only be installed at some vacuum sections during the initial phase of NSLS-II operation. The RGAs' quadrupole mass filter RF box, which contains sensitive electronics, may be located near the head and needs to be shielded from synchrotron radiation. The PC-based control units for RGAs, however, will be located at the satellite control racks, to allow easy access for online analysis and maintenance. The number of RGAs estimated for the storage ring and front ends is listed in Table 4.4.5.

4.4.6.4 Vacuum Control and Equipment Protection Systems

The vacuum control system has to 1) monitor and control all the vacuum equipment including gauges, pumps, valves, etc., to ensure that they are operating properly in their appropriate ranges; 2) collect and

archive the data for instant display and alarm and for off-line analysis; and 3), most importantly, interlock and protect the storage ring and injector from harm before damage develops.

The vacuum control system will interface directly with each vacuum device, and as part of the storage ring equipment control and protection systems (EPS). Due to high radiation levels in the storage ring tunnel, all the vacuum devices and the vacuum control system will be located at the satellite control racks. They will be backed by uninterruptible power supplies. Vacuum devices include gauge controllers, ion pump controllers, chamber and absorber temperature readouts, cooling water flow sensors, and gate valve solenoids. They can be operated via front-panel switches and with the machine control system through RS232 or Ethernet links for high-level monitoring and control. The low-level vacuum controls, consisting of several dedicated PLCs with digital and analog I/O modules, take inputs from the vacuum devices and send out commands through dry contact circuits. The PLCs, with their own microprocessors and operating systems, will be programmed by vacuum system experts and provide the logic for the operation and control of the vacuum devices.

For gate valve control, the PLCs will use a voting scheme, with inputs from the setpoint contacts of several gauges and pumps, to initiate valve interlock and closure, therefore minimizing false triggering due to the malfunctioning of a single gauge or pump. The PLC for the water flow and temperature monitoring system, with direct inputs from thermocouples and flow meters, will read and compare those with the pre-set values. An out-of-range alarm from this PLC will trigger an output to the EPS to abort the beam, thus preventing overheating of the chamber wall or absorbers, due to either the malfunction of the cooling water system or abnormal beam steering. The PLC outputs for the flow meters, the temperature readouts, and gate valve status will be part of input arrays to the EPS, which will be used to determine if conditions are unacceptable. When warranted, the EPS will initiate a fast beam abort by interrupting the low-level RF power to the accelerating cavities. The stored beam would coast inward to a scraper and be lost in a fraction of millisecond.

References

[4.4.1] J. Noonan, J. Gagliano, G.A. Goeppner, R.A. Rosenberg, and D.R. Walters, “APS Storage Ring Vacuum System Performance,” Proc. PAC97, p 3552-5 (1998).

[4.4.2] C. Doose, L. Emery, and S.H. Kim, “Investigation of the Surface Resistivity Tolerance of the Kicker Ceramic Vacuum Chamber at APS,” Proc. PAC01, p1491-3 (2001).

[4.4.3] J. Jones, S. Sharma, and D. Bromberek, “APS SR Flexible Bellows Shield Performance,” Proc. PAC99, p 3095-7 (2000).

[4.4.4] C.L. Foerster, C. Lanni, and K. Kanazawa, “Measurements of photon stimulated desorption from thick and thin oxide of KEKB collider copper beam chambers and a stainless steel beam chamber,” *J. Vac. Sci. Technol. A* **19**, 1652 (2001).

[4.4.5] C.L. Foerster, C. Lanni, J. Noonan, and R.A. Rosenberg, “Photon stimulated desorption measurements of an extruded aluminum beam chamber for the Advanced Photon Source,” *J. Vac Sci. Technol.* A14, 1273 (1996).

[4.4.6] V. Anashin, et al., “Photodesorption and Power Testing of the SR Crotch-Absorber for BESSY-II,” Proc. EPAC98, p. 2163 (1999).

[4.4.7] R. Kersevan, “MOLFLOW User’s Guide,” Sincrotrone, Trieste Technical Report, ST/M-91/17 (1991).

[4.4.8] M.K. Sullivan, “A Method for Calculating Pressure Profiles in Vacuum Pipes,” PEP II AP Note No. 6-94, March 1994. (Vaccalc is a software using the finite differential method for pressure calculation.)

4.5 Beamline Front Ends

4.5.1 Scope

The beamline front ends connect the storage ring to the user beamlines and provide radiation protection to personnel. Most of the front-end components generally reside within the storage ring's shield wall, outboard of the dipole vacuum chamber. The major components of the beamline front-ends are photon masks, shutters, heat absorbers (such as beam-defining apertures and/or slits), fast valves (or other shock wave protection devices), vacuum isolation valves, pressure isolation sensors, and diagnostics. Vacuum chambers are also included; however, the chambers are often part of the individual front-end components. Other components, such as filters, may be included depending on the application. The front end usually starts at the exit to the dipole vacuum chamber and extends to a beryllium window or a differential pump, where the user vacuum is isolated from the machine vacuum. If a beryllium window is used, it generally is positioned as close as is practical to the outer end of the storage ring shield wall. Also to be considered as important front-end components are radiation shields, i.e., safety shutter shields and bremsstrahlung shields. Vacuum pumps, vacuum sensors, and diagnostics (e.g., for Residual Gas Analysis, to activate fast valves, etc.), heater tape and provisions for bakeout, as well as the vacuum valves, are included in the front ends—even though these components are generally considered part of the vacuum system. Support tables and stands made of structural steel are provided to support the front-end components at the nominal 1m beam height.

Only six beamline front ends will be installed in the initial scope of the project: three in-vacuum undulators (IVUs), two damping wigglers (DWs), and one elliptically polarized undulator (EPU). The project scope also includes engineering and design effort for the bending magnet (BM) and three-pole wiggler (3PW) front ends. The preliminary design of the front end described below can be adopted, with appropriate modifications for beam power and beam size, to all front ends.

4.5.2 Standard Front End Design

Figure 4.5.1 shows the preliminary layout of a typical front end with its main components and their approximate locations from the center of a long straight. The first component is a bending magnet photon shutter (BMPS) which intercepts bending magnet photons when there is no front end or when a front-end is under maintenance. A slow gate valve (SGV) is the next component provided to separate the storage ring vacuum from the front-end vacuum. Until a complete front end is available for installation, the BMPS and SGV are locked in closed position, and an out-of-vacuum lead stop is provided downstream of the SGV to stop bremsstrahlung radiation.

The next component is an e-beam deflector (EBD), which prevents the injected beam from accidentally entering the beamline hutch during top-off injection. The EBD consists of permanent magnet blocks that provide a vertical field of 1.1 T over a 20cm length with a pole gap of 14 mm. The EBD is designed to deflect a 3GeV beam horizontally into the stationary tungsten blocks of the safety shutter (see below), located at ~7 m downstream. The beam is deflected at this location by 15 cm, which is 5 cm more than the horizontal beam aperture provided in the tungsten blocks.

A pair of photon BPMs (XBPM-1 and XBPM-2) is used to deliver a stable beam to the user's end station by providing beam position data to the global feedback system. Next to XBPM-1 is a lead collimator (CO), which collimates the angles of bremsstrahlung radiation to minimize the size of tungsten blocks required in the safety shutter (SS) and the amount of supplemental lead in the ratchet wall (R-WALL). The uncooled tungsten blocks in the safety shutter are protected by a water-cooled photon shutter (PS) that is inserted in the beam path before the safety shutter is actuated. A fast gate valve (FGV) in the front end is provided to intercept the pressure shock wave in the case of a vacuum breach in the beamline. Another slow gate valve is

usually provided downstream of the ratchet wall collimator (RWC) to separate front end vacuum from the beamline vacuum. Some front ends will be provided precision X-Y slits between FGV and XBPM-2, at the request of beamline users. All components of a front end requiring actuation (SGV, FGV, PS, SS, and X-Y slits) will be remotely operable.

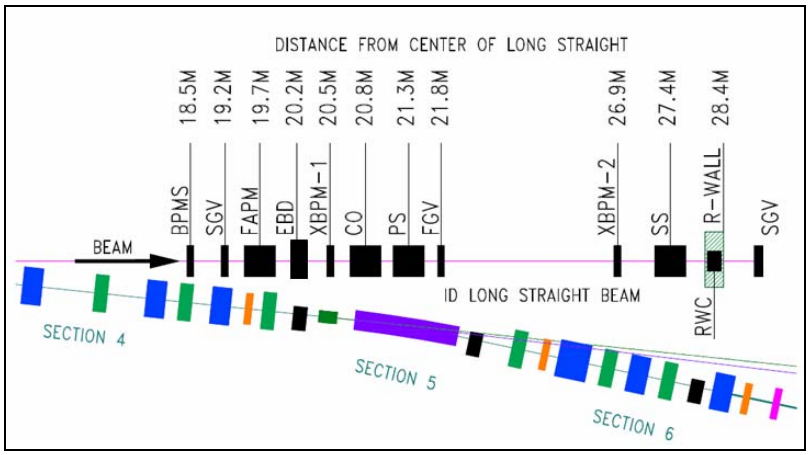

Figure 4.5.1 Typical layout of a front end. From left to right: bending magnet photon shutter (BMPS), slow gate valve (SGV), fixed aperture photon mask (FAPM), e-beam deflector (EBD), first photon BPM (XBPM-1), lead collimator (CO), photon shutter (PS), fast gate valve (FGV), second photon BPM (XBPM-2), safety shutter (SS), ratchet wall collimator (RWC), and slow gate valve (SGV).

The power densities of the NSLS-II insertion devices, shown in Table 4.5.1, are lower than those at the APS Undulator-A (130 kW/mrad^2 at 100 mA). We plan to adopt the APS designs of the front end components with appropriate modifications for the aperture requirements of each beamline.

Table 4.5.1 On-axis power densities of NSLS-II insertion devices (3 GeV, 500 mA).

	Name						
	U20	U19	U45	U100	DW-1.8T	SCW	3PW
Type	IVU	CPMU	EPU	EPU	PMW	SCW	PMW
On-axis power density (kW/mrad$^{2)}$	62.33	77.86	40.03	26.33	55.30	25.60	0.28

Figure 4.5.2 shows the typical APS designs for the three critical components: FAPM, PS, and SS. The heat-absorbing surfaces of the FAPM are designed from a single, solid piece of Glidcop, ~0.5 m long, to handle the high heat flux of the insertion devices. Water-cooling channels are gun-drilled in Glidcop block before machining for the beam aperture with 4° taper and brazing of the Conflat flanges. The design of the PS is very similar to that of the FAPM except that its downstream end can be lowered by an actuator to intercept the photon beam. In the design of the APS safety shutter, two independently movable tungsten blocks are lowered to interlock with the fixed tungsten blocks, thus closing the beam aperture and as well a line-of-sight escape for bremsstrahlung radiation. Only one set of tungsten blocks is being considered in the NSLS-II design, with the provision of redundant position switches for the movable tungsten block, and more restrictive access to the beamline hutches.

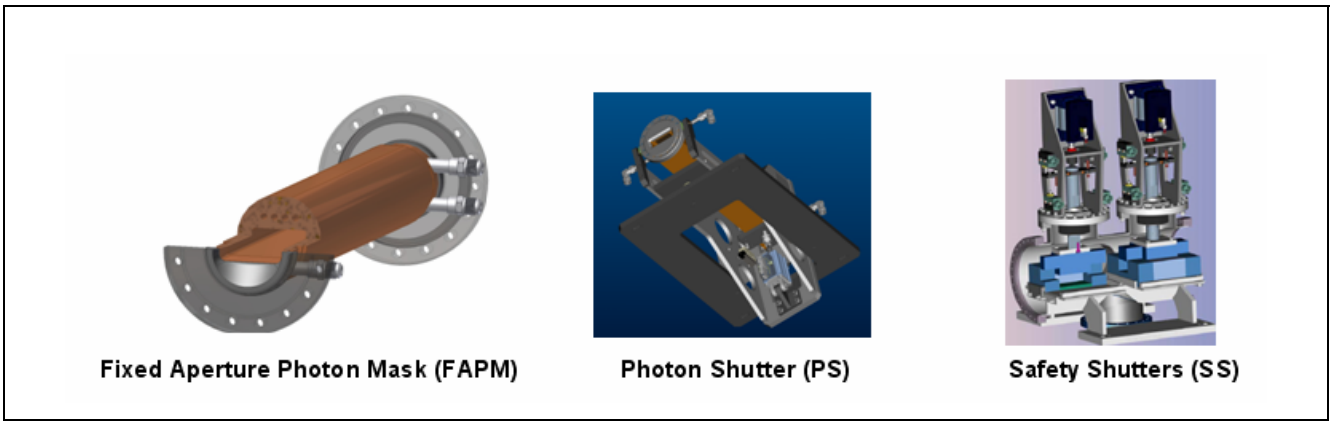

Figure 4.5.3 Typical designs of the APS front end components. Left to right: fixed aperture photon mask (FAPM), photon shutter (PS), and double safety shutter (SS).

FE analyses were performed for all front end components. The most critical component is the photon shutter which is located at ~20 m from the center the IVU in the short straight. It intercepts x-rays at an incidence angle of 4º. The analysis results (Figure 4.5.4) show a maximum temperature of 303 ºC is at the center of the beam footprint. In comparison, the acceptable temperature rise in Glidcop is ~400ºC, based on its thermal fatigue life.

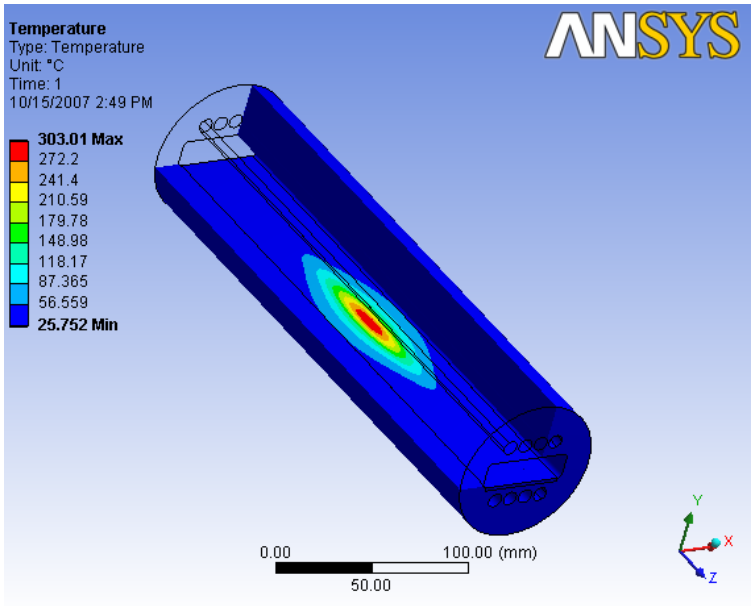

Figure 4.5.4 Temperature profile in the photon shutter located at 19 m from the center of an IVU.

4.5.3 Vacuum Components/Enclosures

The front end vacuum chambers and ducts will be constructed from 304L stainless steel and will be joined to adjacent components using commercially available Conflat flanges, copper gaskets, and UHV hardware. Fabrication of chambers and ducts will be from stainless steel utilizing TIG-welded construction.

Because the front ends share the storage ring vacuum, front-end and SR vacuum pressures must be compatible. A pressure of 10^{-9} Torr therefore must be maintained in the beamline front ends during machine

operations. To achieve these pressures, we will use a combination of UHV components and procedures, in addition to bakeout of the front-end subsystem. The chambers and beam ducts will be designed to withstand a bakeout temperature of 200°C, to accelerate the release of gases. We expect that an integral bakeout system will be incorporated in the beamline front end, to enable the capability of in-situ bakeout.

Only all-metal commercially available gate valves will be used in the front ends. An all-metal right-angle valve will be located between the photon shutter and the fast-closing valve. Attached to this valve will be a fitting with both an ion gauge and an RGA to monitor the total and partial pressures of the front-end vacuum. At the remaining port of the cross, a valve will be installed (to be used in combination with the right-angle valve) to allow for venting and pump-down when replacing either the ion or RGA gauge filaments. Additionally, installation of a vacuum valve between the fast-closing valve and the XBPM-2 is planned, to allow for separate venting/pump-down of the downstream portion of the front end. The fast gate valve should close in less than 15 msec and have a leak rate of less than 7.5×10^{-10} Torr-l/s when closed. Two ion pump/titanium sublimation pump combinations are planned, located strategically in each beamline front end. To minimize any residual gas species generated by the photon beam impinging on a surface, a 400 L/s ion pump/TSP pair will be installed near the photon shutter locations. An additional 400 L/s ion pump/TSP pair will be installed at the safety shutter, due to the relatively long distance (~5 m) between the photon shutter and safety shutter.

4.4.3.2 Radiation Protection

At times during storage ring operations, it will be necessary to access the experimental hutch (for example, to set up equipment and change samples). The remotely actuated safety shutter device is provided (see Figure 7.5.1) to stop brehmsstrahlung radiation, thus providing protection from ionizing radiation for personnel downstream of each shutter. From calculations, a thickness of 20 cm of tungsten is required to attenuate the brehmsstrahlung radiation in the forward direction. Ray-tracings will be done to determine the transverse dimensions of the tungsten shielding. Additionally, lead collimators will be provided in each front end to confine the radiation cone in the downstream experimental area. From calculations, a thickness of at least 30 cm of lead for the collimators will be required to attenuate the brehmsstrahlung radiation in the forward direction. As with the tungsten shield of the safety shutter, ray-tracings will be performed to determine the minimum transverse dimensions of lead required.

A byproduct of the brehmsstrahlung/lead collimator interaction is the production of neutrons that ultimately must be shielded. The concrete used in the shielding wall is a very effective neutron shielding material; however, there will be beampipe penetrations through the shield wall that must be considered. Void volumes between the shield wall and front-end beampipe penetrations will be filled with concrete and lead, to terminate the transit of photons and neutrons beyond the shield wall. For exit ports with no front end, the shield wall window will be completely filled with concrete.

4.4.3.4 Interlocks

The Personnel Protection System (PPS) will monitor the position of the safety shutter to provide personnel at the beamline safety from prompt radiation. The Equipment Protection System (EPS) will control the sequencing and control of front-end devices and prevent damage from occurring. The EPS will prevent damage to front-end components by sensing position, water flow, and vacuum, then taking action by operating components or dumping the beam, when appropriate.

To protect the storage ring vacuum from any inadvertent pressure rise due to front-end or beamline component failures, various interlock sequences will be implemented. Two possible scenarios in which an air-to-vacuum leak in the front end would corrupt the SR vacuum are mentioned here as examples: 1) a slow air-to-vacuum leak due to faulty bellows or a leaking weld in a vacuum chamber, and 2) a catastrophic vacuum leak due to a failure in a beamline.

If monitoring of the vacuum quality indicates a slowly increasing pressure, the origin of this pressure rise will be investigated and repaired during a regularly scheduled maintenance period. Should the pressure in the front end reach the ion gauge set point of approximately 5×10^{-7} Torr, the EPS will first signal the insertion device on the offending beamline to open its gap, thereby eliminating the high heat flux on any front-end components. The bending magnet photon shutter will then be actuated to provide dipole radiation protection to the uncooled isolation valve when it has been moved into the closed position. Finally, first the photon shutter and then the safety shutters will be the last devices instructed to close. With the storage ring isolation valve in the closed and sealed position and PPS in place, ring operations will be allowed to continue unhindered by the vacuum leak in the front end. The front end or beamline experiencing such vacuum difficulties would be repaired during a regularly scheduled maintenance period. Note that all of these front-end actions will be taking place in the background while facility operations continue unhindered.

In the case of a catastrophic leak, once the fast-closing valve is triggered by a pressure exceeding 5×10^{-6} Torr in the front end or beamline, the EPS will send the appropriate signals to dump the stored electron beam. Triggering of the FV will simultaneously close the BMPS, isolation gate valve, and safety shutters. Operations may resume when proper sealing of the isolation gate valve has been verified and the vacuum leak in the front end or beamline has been isolated from the SR vacuum.

4.6 Storage Ring RF Systems

The large dipole radius (25 m) and the medium energy (3 GeV) of NSLS-II result in very low radiated energy from the bending magnets (288 keV/turn). This increases the effectiveness of eight damping wigglers to reduce the bare emittance of 2.1 nm-rad to 0.5 nm-rad. The RF system power requirement for NSLS-II is determined primarily by the power radiated by the damping wigglers. This makes it possible for us to stage the RF system installation to parallel the installation of damping wigglers and user insertion devices.

The small momentum compaction (0.0037), an RF frequency of 500 MHz, and high RF voltage result in small bunch lengths of ~4 mm. This contributes to a short Touschek-dominated lifetime of <2 hours. To improve lifetime to greater than 3 hours, a third harmonic bunch lengthening cavity is included in the baseline design.

The storage ring RF system consists of the 500 MHz Superconducting RF cavities, their associated klystron tube amplifiers and power supplies, the passive SCRF third harmonic Landau (bunch lengthening) cavity, the liquid helium cryogenic plant, and the master clock, frequency synthesizers, digital cavity controllers, and RF distribution system that make up the low-level RF.

4.6.1 Physics Requirements and Design Parameters

The RF system must provide sufficient momentum acceptance (bucket height) so as not to be the limiting factor in the storage ring acceptance. In addition, with the small momentum compaction of the low emittance lattice leading to very short bunches, and the accompanying short lifetime, a third harmonic (1500 MHz) RF system is used to lengthen the bunches to increase the Touschek lifetime from <2 hours to >3 hours. The Landau cavity also increases the dependence of the synchrotron tune on the oscillation amplitude providing Landau damping, which can suppress bunch instabilities. The required RF power is the sum of the beam radiated power in the dipoles, damping wigglers, and user IDs. There is no unique approach to meeting the RF requirements; in fact, the frequency choice of 500 MHz is within a broad range of frequencies in which RF sources and cavity designs exist and that would meet the physics requirements. Three frequencies within this broad range, 352 MHz, 476 MHz, and 500 MHz, have been used successfully in third-generation light sources. The operating frequency of 500 MHz has been selected here due to the availability of existing SCRF cavity designs, commercial RF transmitters, and the large number of 500 MHz systems in use at light sources around the world. This translates into mature technologies and lower development costs. A summary of the ring parameters related to the design of the RF system is shown in Table 4.6.1.

Table 4.6.1 RF and Beam Parameters for the NSLS-II Storage Ring.

RF frequency [MHz]	**499.68**
Circumference [m]	792
Harmonic number	1320
Loss per turn (assuming 5 undulators, 21 m of DW, and dipole losses) [keV]	816
RF acceptance [%]	3
Accelerating voltage [MV]	3.3
Momentum compaction	3.7×10^{-4}
Bunch charge [nC]	1.25
Number of buckets filled with charge	1056

The radiation from dipoles and an assumed complement of five undulators and 21 m of damping wigglers result in an energy loss per turn of 816 keV, corresponding to 408 kW power loss at the design current of 500 mA. A 3% momentum acceptance ($\Delta p/p$) is specified to ensure sufficient Touschek lifetime of the storage

ring. For 816 keV/turn energy loss, this corresponds to an RF voltage of 3.3 MV (see Figure 4.6.1). As insertion devices and damping wigglers are added as the user program is built out, the loss per turn increases to more than 1.6 MeV, and a voltage of 4.8 MV is required to maintain the 3% bucket height.

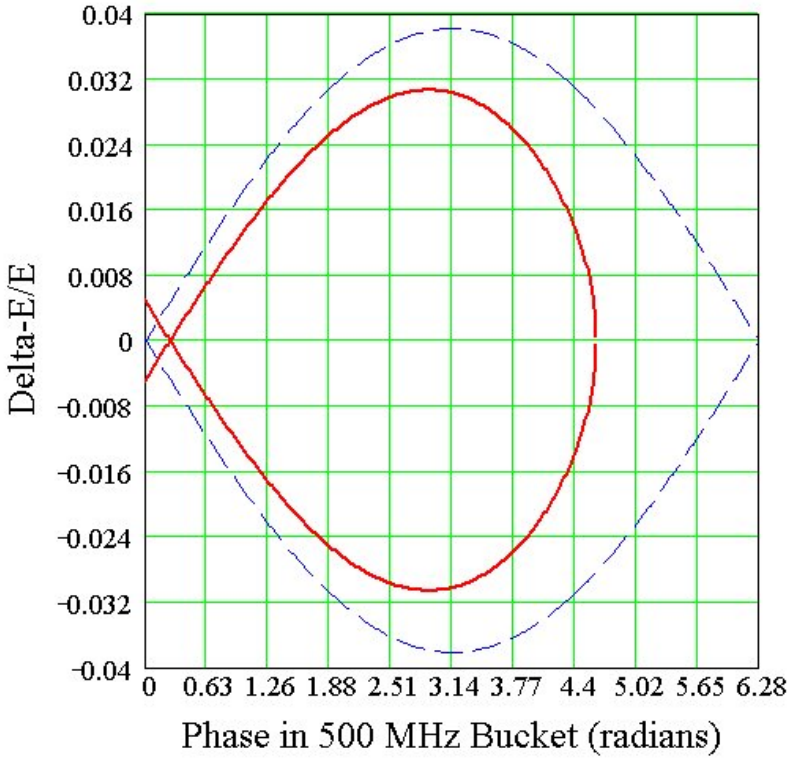

Figure 4.6.1 RF seperatrix for 3.3 MV RF field with (red trace) and without (blue trace) 816 keV/turn radiation losses. The 3% RF acceptance is easily met with two CESR-B cavities.

Thus, the evolution of the RF power requirements over the life of the facility must be taken into account. Table 4.6.2 outlines the initial machine configuration, the capabilities of the RF system, and a reasonable extrapolation as to how this might evolve as insertion devices are added. The exact scenario will be driven by the user requirements and is not fixed at this stage of the machine design.

Table 4.6.2 RF Power Requirements for Dipole Losses and Various Example Insertion Device Configurations for one, two, and four RF systems installed.

	Phase 1: Capability of installed RF (270kW/cavity)		Phase 2: Adding 2nd cavity plus purchase 300-kW Transmitter		Phase 3: Add 3rd and 4th RF station (cavity + transmitter)	
RF power requirements	**#**	**P (kW)**	**#**	**P (kW)**	**#**	**P (kW)**
Dipole	-	144	-	144	-	144
Damping wiggler (9.23 kW / m, 7 m each)	0	0	3	194	8	517
IVU (2.7 kW/m, 3 m each) [CPMU] (3.77kW/m, 3m each)	3	24	[6]	66.6	[10]	111
EPU (4.1 kW/m, 4 m each)	1	12	4	48	5	60
Total		180		452		832
RF power available for additional ID's		90		88		248
Total Available RF power		270		540		1080

The initial RF system will consist of two CESR-B cavities, each powered by a 310 kW transmitter. Three cavities will be purchased with the third cavity to be used as a spare in the event of a cavity failure. Two installed cavities can provide up to 5 MV, which exceeds the voltage requirement of 4.8 MV even for the full complement of insertion devices and the 56 m of damping wigglers envisioned for NSLS-II. However, the power coupler is capable of delivering only ~270 kW of beam power, and so the ring is limited to four damping wigglers and 10 user IDs (or equivalent) by the initially available RF power. Installing a third cavity and transmitter will support a full complement of eight damping wigglers, resulting in the ultimate horizontal emittance of 0.5 nm-rad. Two 500 MHz cavities and one 1500 MHz harmonic cavity (to be described in Section 4.6.3) fit into a single 8 m straight. A second RF straight is reserved for the third and potentially fourth CESR-B cavity and second 1500 MHz cavity, to meet the evolving power requirements of NSLS-II as more user IDs are added.

4.6.1.1 Impedance Analysis and Beam Stability

The high beam loading due to 500 mA average stored current requires highly damped structures to prevent beam instabilities. In this regard, the B-factory cavity designs of KEK, PEP-II, and Cornell are attractive and have been studied in detail.

The narrow band cavity impedances have been calculated using the codes GdfidL, SUPERFISH, and CLANS [4.6.1, 4.6.2, 4.6.3]. These codes calculate the longitudinal shunt impedance as

$$R_{sh} = \frac{\left[\mathrm{Re}\left(\int E_z(z) e^{ikz/\beta} dz\right)\right]^2}{2P}, \tag{4.6-1}$$

where P is the power dissipated in the cavity, E_z is the longitudinal electric field either on axis (monopole modes) or displaced with a radial offset corresponding to a dipole mode, quadrupole mode, etc. Here, k is the wave number (ω/c), and β is the ratio of beam velocity to that of light.

The cavities also have transverse impedances that can couple strongly to the beam. The transverse shunt impedance of a cavity is given by the integral of the force acting on the beam, as

$$Z^{\perp} = -i\left(\frac{\int_0^L (\vec{E} + \vec{v} \times \vec{B})_{\perp} ds}{\beta \cdot I_{av} \cdot a}\right), \tag{4.6-2}$$

where L is the cavity length, I_{av} is the average bunch current, and *a* the offset of the beam from the cavity axis. The beam must couple energy into the higher-order transverse mode through the electric field ;hence, there is a relation between the longitudinal and transverse impedances. The broadband impedance model uses the Panofsky-Wenzel relation,

$$Z_{\perp} = \frac{c}{\omega \Delta^2} \cdot Z_{\parallel}^{(\Delta)}, \tag{4.6-3}$$

where Δ is the offset at which the longitudinal impedance is calculated. The cavity impedances have been calculated for the PEP-II, KEK-B, and CESR-B cavities [4.6.4, 4.6.5, 4.6.6]. All three cavity designs can meet the NSLS-II requirements in terms of attainable voltage and beam power delivered. The SCRF approaches of KEK and Cornell result in lower installed RF power requirements and more efficient operation, attain much lower HOM impedances, and require fewer cavities to achieve the voltage specification. This is particularly important when additional insertion devices are installed that will increase the RF voltage

requirement to ~5 MV. The choice for NSLS-II has been narrowed to either the KEK-B cavity or the Cornell CESR-B cavity. Further studies on cost, reliability, and future upgrade potentials in the preliminary design phase will lead to the final choice. For the purposes of this document, the CESR-B cavity is baselined in order to present self-consistent calculations of system parameters such as RF power and cryoplant requirements, coupled bunch growth rates, system mechanical layouts, and cost. Details of the HOM impedances and coupled bunch growth rates are given in Section 6.2.3.

To meet the initial requirements of 3.3 MV accelerating voltage and 408 kW beam power, two RF cavities with individual klystron transmitters are to be installed. A third cavity to be used as a test cavity / spare will be purchased as part of the baseline machine. It is expected that this cavity will be installed in a future upgrade as additional insertion devices increase the beam power requirement to beyond 2×270 kW, a soft limit of the power couplers in the CESR-B cavities. The CESR-B cavity parameters are given in Table 4.6.3.

Table 4.6.3 CESR-B Cavity Parameters.

Frequency [MHz]	499.68 +/- 0.2
Electric field (normalized to 0.3m) [MV/m]	>8 MV/m
Accelerating Voltage (beam energy gain) [MV]	>2.4 MV
Unloaded Q (at 8MV/m)	$>7*10^8$
Static heat losses [W]	<30 W
Dynamic heat losses (at 4.5k and 8MV/m) [W]	<120 W
Maximum power transferred to beam [kW]	>250 kW
Loaded Q	1×10^5

In addition to coupled bunch instabilities caused by higher order modes in the cavities, the fundamental and harmonic RF systems can cause instabilities where all of the bunches oscillate in unison, the so-called Robinson instabilities. The classical Robinson analysis [4.6.7] is particularly relevant for short and compressed bunch operation of the machine. The resistive Robinson instability is not excited by the cavities. This is due to the fact that the main cavities are detuned below resonance to compensate for beam loading, which strongly damps phase oscillations, while the harmonic cavities' very high quality factor greatly reduces the resistive part of their impedance at the synchrotron frequency, and hence their excitatory (or damping) influence on phase oscillations.

The second observation concerns the reactive Robinson instability. In this instability the static bunch distribution is an unstable fixed point of the longitudinal dynamics, and a perturbation of the bunch pushes it with some growth rate away from that distribution, subsequently damping to one of two stable distributions. In the absence of harmonic cavities, the bunch is marginally unstable. The addition of inductively detuned harmonic cavities for stretched bunches tend to suppress this problem; capacitively detuned harmonic cavities for compressed bunches aggravate the instability. In unstretched or compressed operation, however, the unmitigated instability results in only a small phase shift of the bunch due to the narrow potential well. But for stretched bunches the potential well is wide and flat, and the instability results in gross distortion of the bunches, which must be addressed. A simple cure, first recognized by Miyahara [4.6.8], is to introduce a small-bandwidth feedback of the RF system to the beam. Simulations also show that a reduction of the main-cavity impedance using RF feedback suppresses the instability, although too much feedback excites a higher-order oscillatory instability.

Although glossed over in the discussion to this point, with stretched bunches the classical Robinson picture is not so simply applicable; more involved analyses, such as those by Bosch et al. [4.6.9], and numerical simulations are required to assess the stability of higher-order modes of these bunches. As was just mentioned, the use of RF feedback, which allows the adjustment of the impedance of the main cavities, is a means by which some manipulation of bunch stability is possible. Our experience with the NSLS VUV ring

also shows that short-range wakes can have an impact on the stability of stretched bunches, which is further complicated by the varying bunch profiles along the train.

4.6.2 500 MHz RF System

4.6.2.1 500 MHz Cavities

The CESR-B cavity consists of a bulk niobium SCRF single cell with waveguide coupler, a special fluted beampipe to extract the lowest frequency dipole modes, warm-to-cold transition spool pieces for thermal isolation, water-cooled C48 ferrite HOM dampers, and long tapers to transition from the 240 mm cavity bore to the elliptical beampipe. The CESR-B cavity is a "single-mode" cavity. All higher-order modes with the exception of the TM110 dipole mode propagate through the cylindrical beampipe. A fluted beampipe at the opposite end of the cavity has a lower cutoff frequency to allow the TM110 to propagate to the ferrite load. This has only a small effect on the fundamental mode. This allows a shorter attenuation length in the beam tube and a more compact cavity. The cavity assembly is shown in Figure 4.6.2. The layout of two CESR-B cavities plus a single Super3HC harmonic cavity in a single straight is shown in Figure 4.6.3.

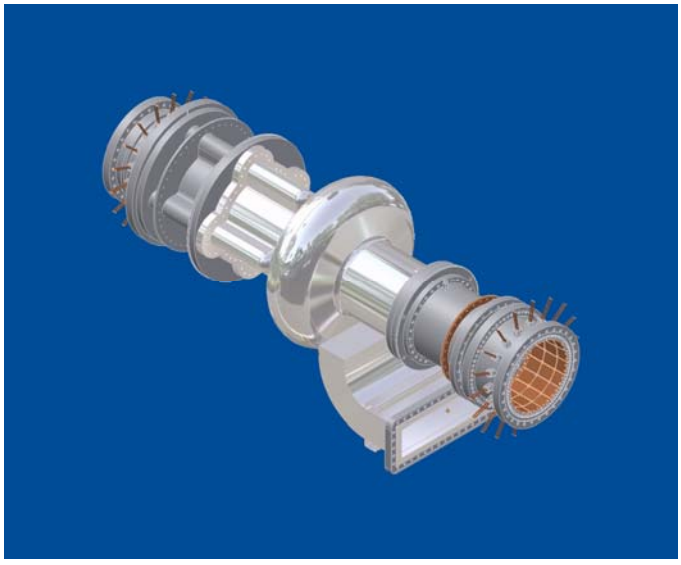

Figure 4.6.2 The CESR-B bare cavity assembly.

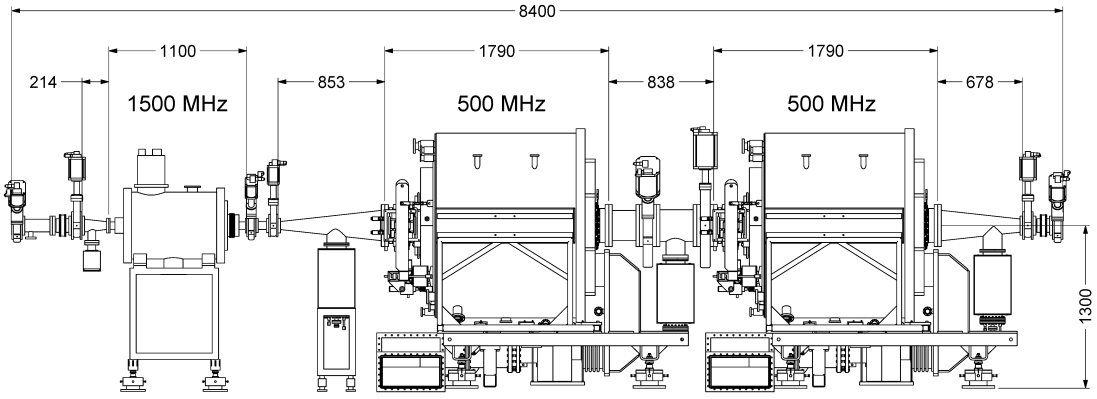

Figure 4.6.3 Layout of two 500 MHz cavities plus one 1500 MHz Landau cavity in a single straight. The tapers from the large cavity beampipe to the ring beampipe are 678-853 mm long, limited by the available length in the straight of 8.4 m. A second RF straight is reserved for additional cavities.

4.6.2.2 HOM Damper

The HOM damper consists of C48 ferrite tiles brazed to water-cooled copper backing plates that form a spool piece outside the cryostat. The ferrite is several 500 MHz attenuation lengths away from the SC cavity. There is power dissipated in the ferrite from two sources. First, there is dissipation of the fundamental 500 MHz field driven by the transmitter. This has been calculated with CFISH [4.6.2, 4.6.10] to be less than 100 W at 2.5 MV cavity voltage. Second, the beam also loses energy from wakefields. This loss is given by

$$P_{loss} = k_{\|} \cdot I_0^2 / n \, T_0 \,. \tag{4.6-4}$$

For NSLS-II, $T_0 = 2.6$ μs, $I_0 = 0.5$ A, and $k_{\|}(\sigma_s = 4\text{ mm}) = 3.6$V/pC, resulting in a $P_{loss} = 2.3$ kW. In the worst case, all of this power is lost in the ferrite, which is still a factor of 4 lower than the design limit.

4.6.2.3 KEK-B Cavity Option

The superconducting cavities developed for the KEK-B factory are being considered as an option for NSLS-II, for several reasons. The most significant advantage is the higher power per coupler, which has been demonstrated at KEK to be greater than 400 kW. In principle, two KEK cavities could meet the power requirements for the full complement of damping wigglers and user insertion devices, ~800 kW. The waveguide feed at the top of the cryostat makes the tunnel installation easier, and the coupling can be optimized for various beam currents and cavity voltages by simple spacers on the antennae coupling mounting flanges, as opposed to the fixed coupling of the waveguide feed for the CESR-B approach. A layout of two KEK-B cavities in an 8 m straight is shown in Figure 4.6.4.

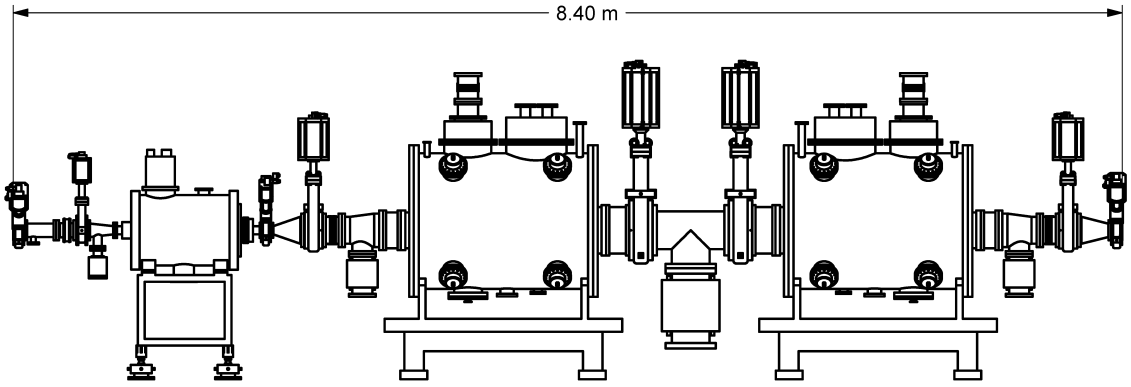

Figure 4.6.4 Installation of two KEK-B SCRF cavities in an 8.4 m (available length) straight.

4.6.2.4 RF Transmitter

The power couplers for SCRF cavities have a wide statistical variation in their power handling capability. Although they have been engineered for high power handling by proper thermal and electrical design, they are prone to multipacting, a resonant electron-avalanche effect that can impose a hard limit on power transmission and cause failure by local heating due to electron loading. The multipacting depends on the secondary-emission coefficient of the surface, which in turn depends on the properties of the bulk material, usually copper or niobium, and surface contaminants, which are usually cryo-pumped organics from the machine vacuum. These contaminants can be present at start-up or accumulate over a period of time, degrading performance and requiring, in the worst case, the cavity to be warmed up with a mild bake to drive off the condensed gases. Experience with the CESR-B cavities has shown transmitted power per coupler in the range of 250–330 kW. A transmitted power of 270 kW is assumed for meeting machine requirements and placing a limit on installed RF power. In addition to the energy losses due to radiation in dipoles, damping

wigglers, and undulators, the RF power transmitter and coupler must provide for the HOM losses that are excited by the beam. We are exploring ways of increasing the power per coupler, and will factor this into the preliminary design and choice of transmitter power.

The coupling of the waveguide to the cavity in the ideal case is adjusted so that the cavity presents a matched load to the RF source at the normal operating current and energy. Since there is a phased installation of cavities and insertion devices, this optimal coupling varies over the life of the machine. The KEK-B cavity has an adjustable antennae coupler that, in principle, can be changed to follow the optimal coupling. In practice, this must be done in a clean room environment and may be of limited value.

For an aperture-coupled cavity such as the CESR-B, coupling is set during the design and manufacture. Usually coupling is set so the generator is matched to the cavity at the highest expected beam-loading (beam power) of 270 kW. This minimizes the requirement on installed RF power. For the staged installation of insertion devices (RF power required) and RF cavities there is not a single minima, and it is necessary to balance the mismatch over the different phases. For an approximate match to the conditions in Phase 3 in Table 4.6.2, the maximum reflected power in the other three phases is ~10.5 kW. Alternatively, we can choose the coupling to be slightly over-coupled in the case of the highest beam-loading, and accept In order to reduce the residual reflected power during commissioning and staged insertion device installation, we have the option of installing a 3-stub waveguide tuner between the circulator and the cavity.

There will be variation of the impedance presented by the cavities to the beam at different times of the machine's life due to the varying number of cavities and insertion devices. RF feedback can be used to reduce (or increase) this impedance; this option is being studied and system layout designed to minimize loop delay to allow its implementation. A minimum transmitter power of 275 kW is required to meet the sum of the radiated, HOM, and reflected power demands. To allow for the case of coupler improvement (coupler is limited by multipacting, not power limitations) or system aging (degradation of klystron output power), the transmitter will be designed for a minimum of 310 kW, allowing up to ~280–300 kW per coupler.

A single 300 kW klystron amplifier will drive each of the main ring cavities through a 350 kW rated circulator and load. Klystrons that meet or exceed this power level are available from three vendors: CPI, Toshiba, and Thompson. The klystron beam power will be provided by a Pulse Step Modulation switching power supply at 55 kV and 12 A. The PSM switching power supplies have the benefit of low stored energy, and fast turn-off capability of the IGBTs eliminating the need for a crowbar circuit to protect the klystron. The power supply will have redundant switching cards built in, and will operate at full capacity even with several card failures. The RF transmitter will have local control via PLC, with system parameters and control available to the main control system via an Ethernet link. The PLC will also monitor the PSM switch modules, so that failed modules are logged and transmitter repairs can be scheduled for the next maintenance period. The main ring power systems with a rating of 300 kW are beyond the power limit of air-cooled coaxial cable, and will be implemented in WR1800 waveguide. A layout of the RF straight with the associated RF transmitters is shown in Figure 4.6.5.

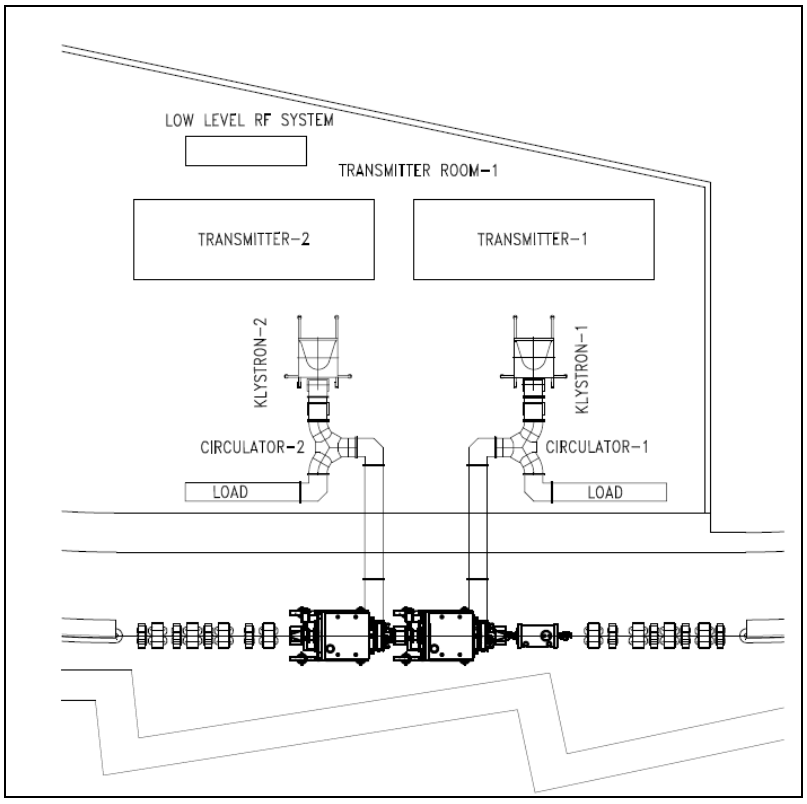

Figure 4.6.5 Layout of an RF straight section with two 500 MHz cavities and their klystron transmitters and a single 1500 MHz harmonic cavity.

An alternative approach of combining several Inductive Output Tube (IOT) amplifiers to obtain the necessary RF power has been developed at other facilities [4.6.11, 4.6.12]. IOT systems have higher efficiencies and some limited failure tolerance. Likewise several hundreds of high-power transistors can be combined to provide the required power. SOLEIL has recently commissioned such a system at 352 MHz [4.6.13]. Both of these options will be explored in detail during the R&D phase.

4.6.3 1500 MHz Harmonic Cavity System

A passive 1500 MHz SCRF cavity, such as the BESSY scaled CESR-B [4.6.14] or Super3HC [4.6.15] scaled SOLEIL cavity, has been studied for the Landau cavity in NSLS-II. Both of these cavities can achieve ~0.5 MV per cell, with the BESSY cavity containing a single cell, and the Super3HC containing two cells per cavity. The details of the impact of the Landau cavity have been discussed in Section 6.2.7 on collective effects. Here we will discuss the hardware and system configuration. For this purpose, two cells (1 cryo-module) of the Super3HC design is in the baseline design.

The nominal voltage and phase of the harmonic cavity is that which cancels the slope and second derivative with respect to time of the total RF field. This results in bunches lengthened by approximately the ratio of the harmonic-to-main cavity frequencies. The field required of the harmonic cavity is approximately the reciprocal of that ratio times the main-cavity field, although slightly less due to the non-zero main-cavity synchronous phase that is a consequence of the beam's radiation loss. In practice, this harmonic-cavity field is pushed slightly higher to provide additional stretching, striking a balance between improved lifetime and the eventual onset of longitudinal instabilities. Furthermore, the use of a gap in the ring's fill pattern for ion clearing results in perturbations of the potential wells that vary along the train. As a result, the lengths of most bunches are shortened by these perturbations and the average lifetime is reduced. For these reasons, the harmonic-cavity field and phase require further investigation. Simulations shown in Section 6.2.7 give a

maximum in bunch length for ~1.1 MV of third-harmonic voltage for the initial fundamental cavity voltage of 3.4 MV. This can be met with a single Super3HC cavity. As the number of damping wigglers and user insertion devices increases, the fundamental mode voltage increases to 4.8 MV and an additional third-harmonic cavity will be necessary for optimal bunch lengthening.

4.6.4 Low-Level RF and Beam Control

The specifications of the RF system amplitude and phase requirements are derived in part from the user requirements that the transverse motion of the photon beam is to be <10% of the RMS beam size, and the increase in photon beam size due to emittance dilution of the electron beam is to be <10%. The relation of the photon beam size and jitter to electron beam size and jitter is influenced by the design of a particular insertion device and beamline, which might impose a tighter tolerance on the electron beam stability. The stability required from the RF system to limit the transverse jitter of the electron beam to 10% beam size is derived below. This will be expanded to study the effect on the photon beam in the next phase of design.

4.6.4 Low-Level RF and Beam Control

The specifications of the RF system amplitude and phase requirements are derived in part from the user requirements that the transverse motion of the photon beam is to be <10% of the RMS beam size, and the increase in photon beam size due to emittance dilution of the electron beam is to be <10%. The relation of the photon beam size and jitter to electron beam size and jitter is influenced by the design of a particular insertion device and beamline, which might impose a tighter tolerance on the electron beam stability. The stability required from the RF system to limit the transverse jitter of the electron beam to 10% beam size is derived below. This will be expanded to study the effect on the photon beam in the next phase of design.

4.6.4.1 RF Tolerances Imposed by User Experiments

Timing experiments, such as the IR experiments run at NSLS currently, require that the timing jitter of the bunch be less than 5% of the RMS bunch length over the frequency range of 500 Hz to 50 kHz. This corresponds to a phase error of 0.16 degree for a 10 ps bunch, or a corresponding momentum jitter of 0.005% due to synchrotron motion.

The majority of users are not concerned with timing experiments but require small and stable photon beam size. The vertical photon beam divergence for a experiment using a higher harmonic of an Insertion Device (ID) is given by[1]

$$\sigma_{y'}^2 = \frac{\lambda_n}{2L}\sqrt{1+16n^2N_w^2\sigma_\delta^2} + \varepsilon_y \Big/ \beta_y \,, \tag{4.61}$$

where n is the harmonic of the ID being used, N the number of periods, L the length of the ID, σ_δ the momentum deviation, ε_y the vertical emittance of the electron beam, and β_y the vertical beta function of the lattice at the insertion device location.

For NSLS-II, ε_y ~8 x 10^{-12} nm·Rad and β_y ~1 m at the ID straights, L ~3 m, N ~100. Because of the n^2 dependence, the worst case is for n >>3, where the two terms on the right hand side of Eq. (1) are comparable. Thus, using Eq. (4-5.1), for a 10 % increase in beam size, the momentum jitter must be 44% of the inherent momentum spread—or equivalently, a phase jitter of 1.4 degrees.

A third limit on momentum spread is due to longitudinal energy oscillation leading to filamentation and increase in beam size. With a momentum kick Δp/p to the bunch, an electron would have a longitudinal oscillation:

$$\delta(t) = \left(\Delta p \big/ p\right) \sin \upsilon_s \omega_0 t + \delta_0 \sin \upsilon_s \omega_0 (t + t_0) . \tag{4-5.2}$$

Because of the longitudinal tune spread the two terms will de-cohere and become

$$\delta(t) = \left(\Delta p \big/ p\right) \sin \upsilon_s \omega_0 (t + t_1) + \delta_0 \sin \upsilon_s \omega_0 (t + t_2) , \tag{4-5.3}$$

where t_1 and t_1 are two random numbers. Averaging over t_1 , t_1 and δ_0 we arrive at

$$\sigma_\delta = \sqrt{\frac{1}{2}\left(\frac{\Delta p}{p}\right)^2 + \sigma_{\delta,0}^2} = \sqrt{1 + \frac{1}{2} f^2 \sigma_{\delta,0}} , \tag{4-5.4}$$

where $f = (\Delta p/p)/\sigma_\delta$ is the relative kick factor. For a 10% increase in σ_δ, f ~ 0.65 or $\Delta p/p = 6.5 \times 10^{-4}$. The corresponding phase jitter is given by

$$\Delta\phi = \frac{h \alpha_c}{\upsilon_s} \Delta p \big/ p , \tag{4-5.5}$$

where h is the harmonic number (1320), α_c is the momentum compaction factor = .00037, ν_s ~0.0087, and $\Delta\phi$ = 2 degrees.

The transverse electron beam size and position are related to the momentum spread and average momentum, respectively. The beam size is given as

$$\sigma_{x,y} = \sqrt{\beta_{x,y} \varepsilon_{x,y} + \left(\eta_{x,y} \sigma_\delta\right)^2} . \tag{4-5.6}$$

The residual dispersion η_y is of the order 1 mm and the second term is negligible in beam size. Vertical position is given as $y = y_0 + \eta_y \langle \delta \rangle$. The allowed centroid jitter is 10% of the beam size or 0.3μm; therefore, the average momentum jitter should be less than 3×10^{-4}, with a corresponding phase jitter of 0.95 degrees. These limits are summarized in Table 4.6.1.

Table 4.6.1 Longitudinal beam stability requirements

	Phase jitter (°)	Momentum jitter (ΔE/E x10^{-4})
Timing-dependent experiments	0.16	0.5
Vertical divergence (from momentum jitter	1.4	4.4
10% increase in σ_δ due to filamentation	2.0	6.5
Vertical centroid jitter (due to residual dispersion)	0.95	3
Dipole, TPW Beam lines (Position stability due to momentum jitter)	0.32	1

Due in large part to the near zero dispersion in the ID straights which mitigates the effect of momentum jitter, the tolerance on the RF is dominated by the IR timing experiments.

The magnitude of the effect on the beam of RF phase and amplitude noise depends on whether the source of the RF jitter is random or harmonic (systematic). Sources of noise are broadly classified into continuum sources possessing a continuous and slowly varying (with respect to frequency) spectral density, and spurious sources that possess spectral lines, possibly varying in time. Examples of the former are the continuum component of synthesizer phase noise, amplifier shot noise, and the continuum components of other active devices in the RF system. Examples of the latter are line related and power-supply switching noise, microphonics, and vibration. To assess the impact of, and derive tolerances for, RF-system noise sources, we need to determine the beam's sensitivity to noise from identified sources and derive a tolerance budget. The sensitivities are to be determined by modeling the RF system's linear response to these sources. Noise magnitudes in existing machines are a starting point for noise intensities, from which sensitivities are used to determine where noise tolerances need to be tightened. This work is in progress, and will be expanded in the preliminary design phase. Digital low-level RF systems have achieved less than 0.1 degree phase and 0.1% amplitude stability [4.6.16], these tolerances should be sufficient for NSLS-II.

4.6.4.2 Master Oscillator and Ring Frequency Synthesizers

The low-level RF and beam control design is at a preliminary stage of defining specifications and architecture. Unlike the power systems, which stay relatively static over long periods of time during the life of the machine and should be transparent to the user, the LLRF and beam control requirements may change several times as the machine evolves, so the design must be flexible. To this end a digital architecture is used.

An ultra stable Master Oscillator at the fundamental RF frequency is distributed to the storage ring, booster and linac RF stations as well as other systems such as bunch feedback systems and beam diagnostics. The Master Oscillator is software tunable to allow for a radial (frequency) loop to stabilize the beam orbit against slow drifts caused by diurnal or annual variations in machine circumference. The RF frequency is nominally 499.68 MHz ± 20kHz to cover seasonal variations, machine studies (measurement of chromaticity, etc). For the sake of clarity in the description of the low level RF it will be assumed to be 500 MHz. The Master Oscillator is mixed with an IF frequency generated from the same master oscillator. The (RF+IF) frequency is used as a local oscillator for the up/down conversion of the 500 MHz RF signals. An example of such a system is shown in Figure 4.6.6. An IF frequency of 50 MHz is chosen resulting in a 550 MHz LO frequency. This has the advantage of having a common subharmonic in the ring revolution frequency (F_{rev}) of 379KHz for both the RF (÷1320) and LO (÷1452). Thus, the F_{rev} can serve as a synchronization clock on system power-up for all of the ring, booster, and linac controllers as well as serve as a bunch zero clock for timing. The 10 MHz frequency standard for the Master Oscillator will be available as an external time base for other systems.

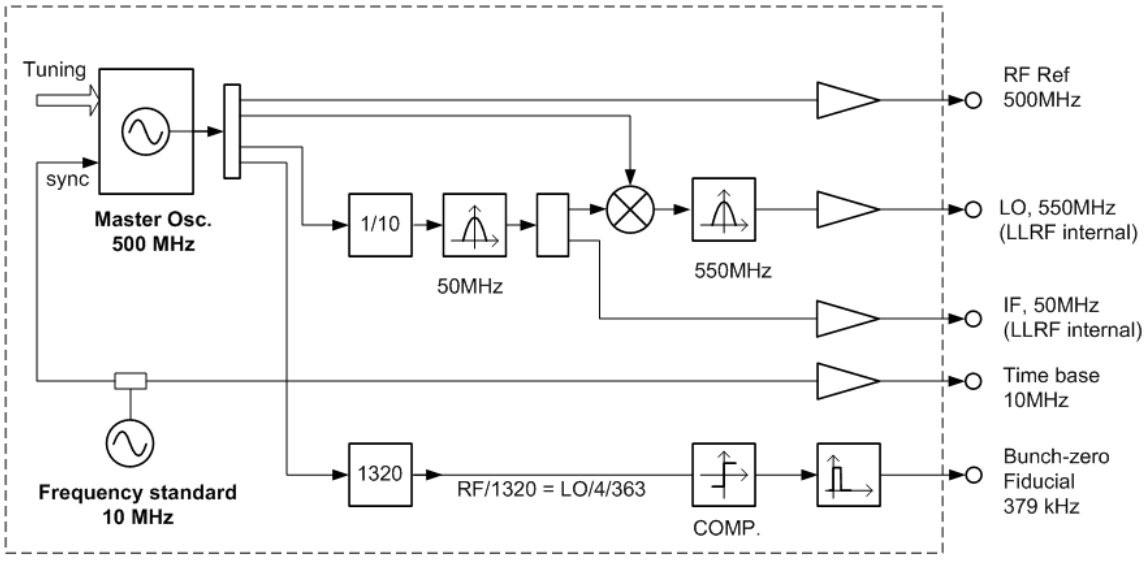

Figure 4.6.6 Master oscillator.

4.6.4.3 Cavity Controllers

The cavity-amplifier system has several nested feedback loops to control the amplitude and phase of the RF cavity fields in the presence of beam-loading, mechanical perturbations to the cavity, and residual klystron noise due to power line/DC power supply ripple. The innermost loop is the tuner loop, which tunes the cavity resonance in order to present a purely resistive impedance to the klystron, thus minimizing klystron power. This loop, which is closed around a mechanical tuner, is slow—on the order of 1 Hz. Next is an RF feedback loop that is used to adjust the impedance of the main-cavity accelerating mode. In order to stabilize the cavity fields against fast perturbations, an amplitude and phase loop around the klystron-cavity chain is implemented. Although these can be independent loops, it is more effective to combine them in a common In-phase and Quadrature (I/Q) modulation loop, due to the coupling of the loops by cavity detuning for beam loading.

In addition to the above RF, amplitude, phase, and tuner loops, it may be necessary to implement other loops. A loop for zero-order coupled-bunch-mode feedback from the beam to the RF system to damp Robinson or higher-order longitudinal instabilities may be necessary. A klystron scalar phase loop to reduce the DC power supply induced the klystron, and possibly a feed-forward loop on the anode modulation of the klystron for maximizing klystron efficiency under different operating conditions, may also prove useful.

With the exception of direct RF feedback, the above loops can be implemented in either analog or digital hardware. Analog systems have the advantage of being simpler and less expensive to produce, and have higher speed and bandwidth. Their disadvantages include the lack of flexibility in changing loop characteristics for varying beam loading, slightly less phase and amplitude accuracy, and DC shifts that are more difficult to control. Digital implementation has the advantage of flexibility, in particular of being able to synthesize the loop filters digitally so that the feedback loops can be programmed for different machine states. Higher accuracy can be achieved, and DC drifts are easier to control. This comes at the price of higher complexity, and requires an additional skill set in high-speed digital design. Careful attention must be paid during the design stage to design in “digital probes” and other debugging tools to monitor and allow trouble shooting of the digital feedback loops.

To maximize the performance of the RF system and allow simple optimization and upgrades over the life of the machine, a digital implementation is our choice for NSLS-II.

The low-level RF cavity field control will be via a digital I/Q modulator-demodulator incorporating up and down conversion, ADCs and digital-to-analog converters (DACs) interfaced to the digital baseband signal processing, a Field Programmable Gate Array (FPGA) state machine, and interface to the control system. Similar systems have been designed for both hadron and electron machines in recent years [4.6.18, 4.6.19].

Although the booster and linac RF systems are simpler since they do not have the tight RF specifications of the storage ring, and harmonic cavities are easier because they are passive with only tuner control, we will use identical ring controllers throughout, with up and down conversion from 500 to 1500 and 3000 MHz. The only difference will be how the control loops are programmed and their control system graphical user interfaces. This makes the control system integration easier to manage with I/O, yet memory buffers for fault analysis, development tools, and maintenance identical.

The controller is derived from the LBNL LLRF4 design [4.6.20]. Five RF input channels support measurement of the forward, reflected, transmitted, and reference phase RF signals plus a beam pickup signal. The 14-bit input ADCs are clocked at 68.75 MS/s derived by a divide by eight from the 550 MHz LO. Two Direct Digital Synthesizers (DDS) built into the FPGA provide two output IF frequencies via DACs clocked at 137.5 MHz (LO divide by four). These are up-converted to the cavity drive and an RF calibration signal.

A conceptual design of the digital controller is shown below in Figure 4.6.7.

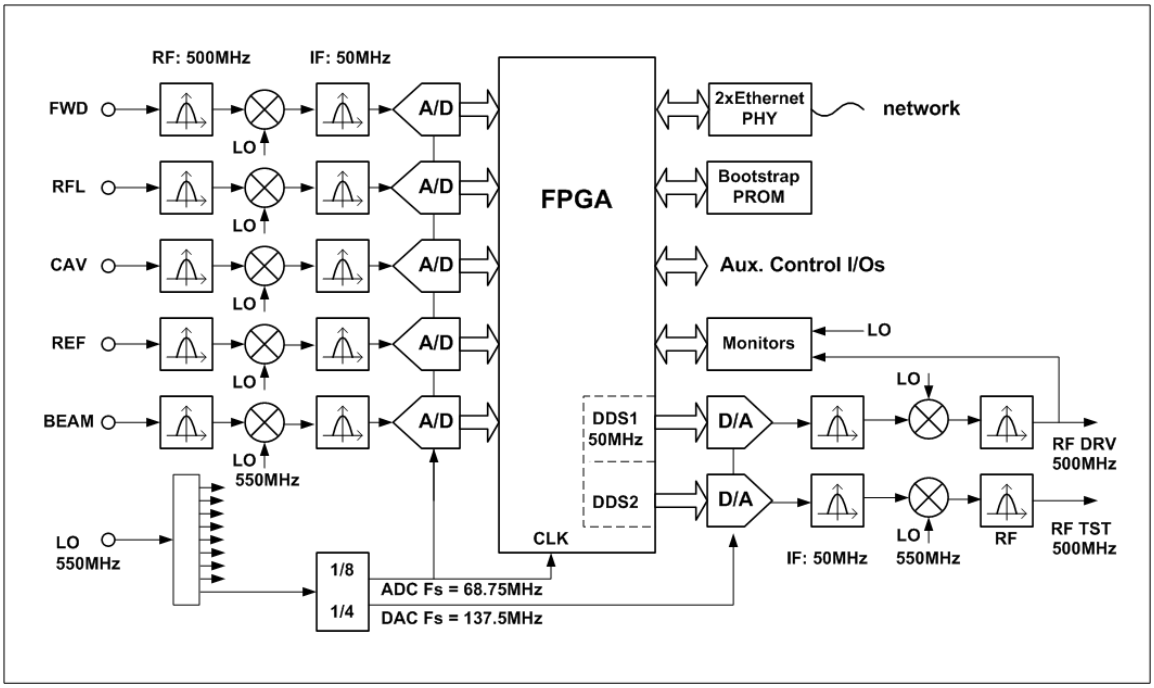

Figure 4.6.7 500 MHz Cavity controller.

Feedback algorithms within the FPGA logic will provide low frequency stabilization of the RF fields., with the phase auto-zeroed to the phase reference line. It will also adjust the fundamental RF cavity dynamic impedance for maximum stability, using information from a beam phase pickup and from the landau cavity fields.

In addition to the fast RF loops, a slower cavity tuning loop measures the phase shift between the cavity input and output, and adjusts the cavity tuner for optimum phase (usually coinciding with minimum reflected RF power). The landau cavity, since it is a passive cavity, has only this tuner loop. In order to use the same cavity controller, an additional LO frequency of 1000 MHz (2x RF frequency) will be used to down-convert

from 1500 to 500 MHz, from which point the hardware will be identical to the fundamental system. A fully built-out RF straight is shown in Figure 4.6.8 below.

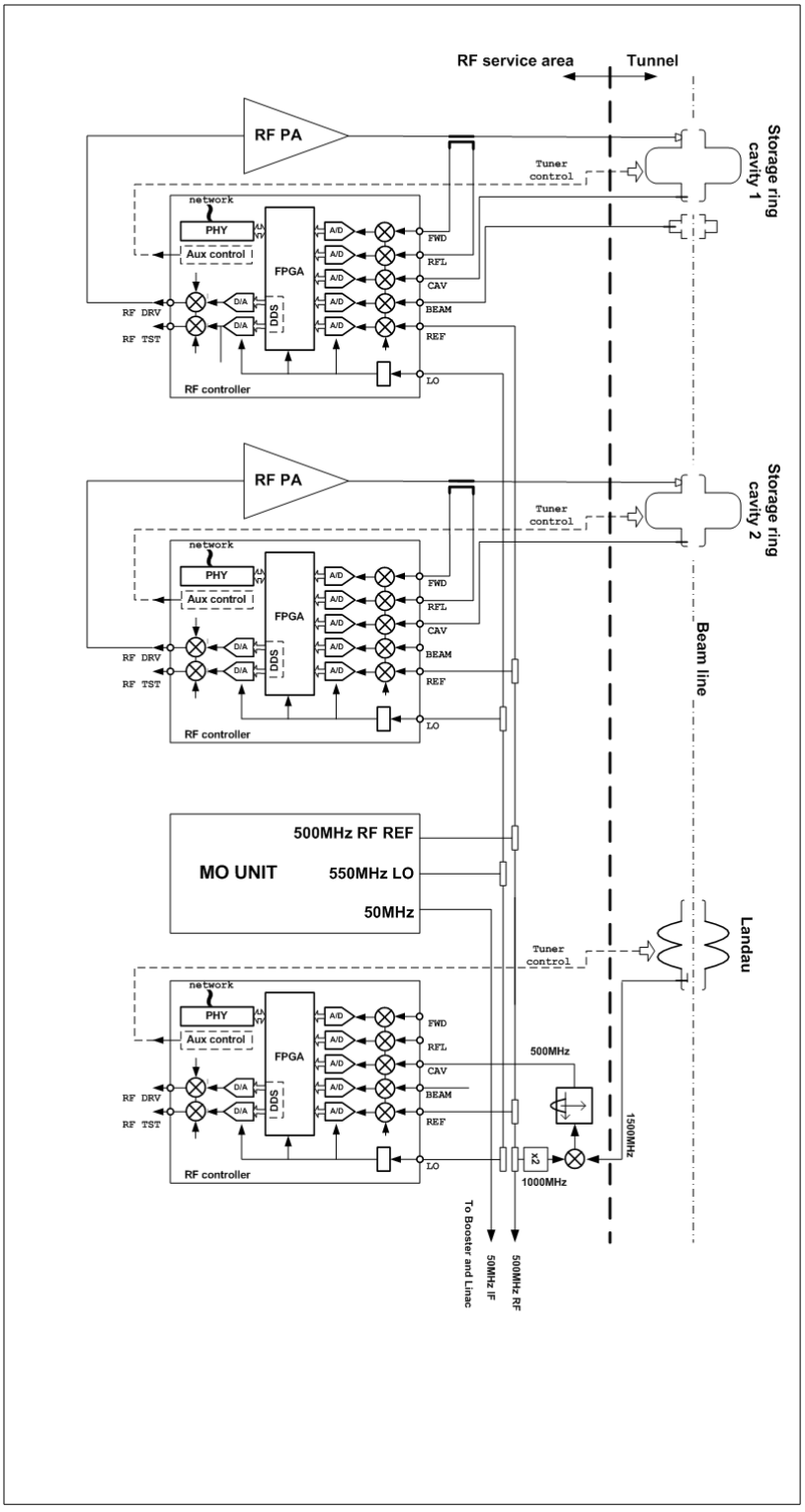

Figure 4.6.8 Storage ring system configuration.

The booster RF is very similar to the ring RF, with the exception that beam phase feedback is not expected to be included. Since the 500 MHz RF reference and the 50 MHz LO are distributed from point to point, the 550 MHz LO must be generated at the booster. It is shown in Figure 4.6.9. Identical up/down conversion from 50 MHz IF to 500 MHz RF will be used, as in the storage ring.

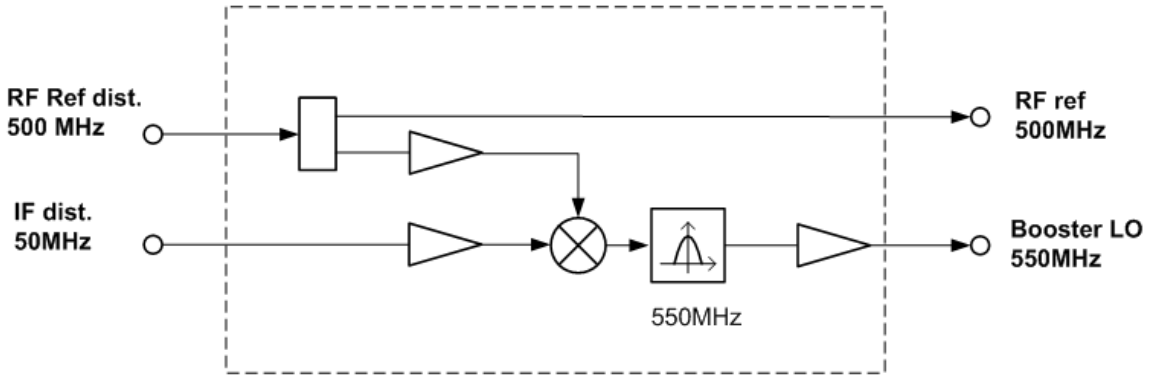

Figure 4.6.9 Booster LO generation.

The linac consists of a 500 MHz subharmonic buncher, a 3000 MHz pre-buncher with independent amplifier (and hence controller), and three klystron amplifiers. The first klystron output is split and drives a final buncher through a high-power attenuator/phase shifter and the first accelerating structure directly. The second and third klystrons drive their respective accelerating structures directly. Thus, one 500 MHz and four 3000 MHz systems need RF control. Again, to use identical RF cavity controllers the 3000,MHz signals are up/down-converted with a double conversion using 2500 MHz and 550 MHz LO frequencies. The LO generation is shown in Figure 4.6.10.

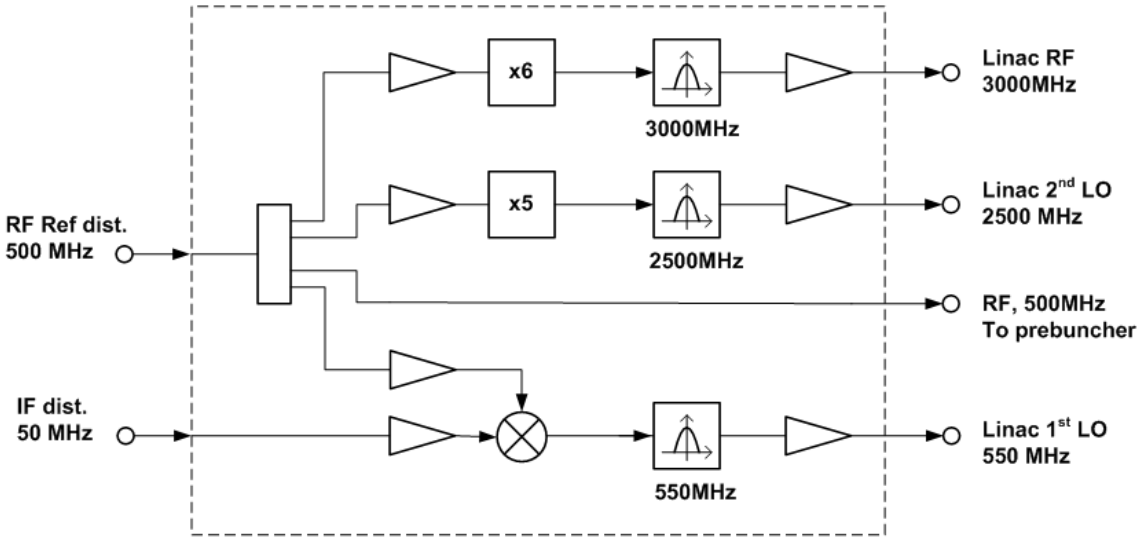

Figure 4.6.10 Frequency synthesis at the linac.

The controllers' 50 MHz IF frequency is first up-converted to 500 MHz using the 550 MHz LO, as in the 500 MHz systems. Then it is up-converted to 3000 MHz using the 2500 MHz LO. A system schematic is shown in Figure 4.6.11.

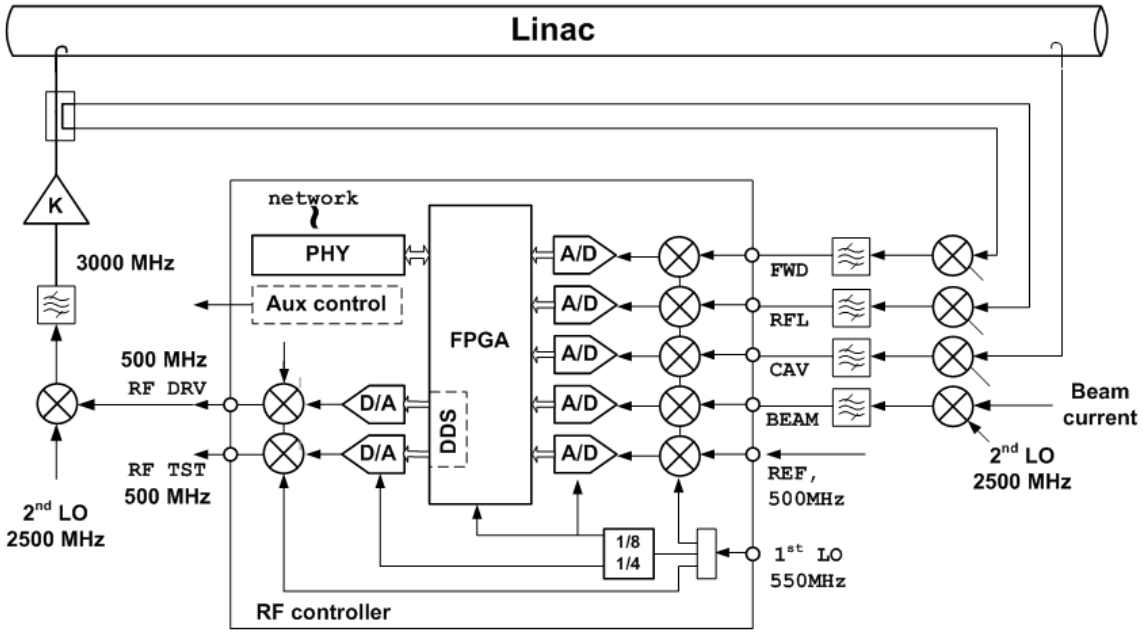

Figure 4.6.11 Linac up/down conversion and controller architecture.

References

[4.6.1] W. Brauns, www.gdfidl.de

[4.6.2] K. Halbach and R. F. Holsinger, "SUPERFISH - A Computer Program for Evaluation of RF Cavities with Cylindrical Symmetry," Particle Accelerators **7** (1976) 213-222.

[4.6.3] D. Myakishev, "CLANS2 - A Code for Calculation of Multipole Modes in Axisymmetric Cavities with Absorber Ferrites," Proceedings of the 1999 Particle Accelerator Conference, NYC.

[4.6.4] R. A. Rimmer et al., "An RF Cavity for the NLC Damping Rings," Proceedings of the 2001 Particle Accelerator Conference.

[4.6.5] S. Mitsunobu et al., "Status and Development of Superconducting Cavity for KEK-B," Proceedings of the 1997 Particle Accelerator Conference.

[4.6.6] J. Kirchgessner, Part. Accel. 46(1):151 1995.

[4.6.7] K.W. Robinson, CEAL-1010, Cambridge Electron Accelerator, Cambridge, MA (1964).

[4.6.8] Y. Miyahara et al., "Equilibrium Phase Instability in the Double RF System for Landau Damping," NIM A-260 (1987 p 518-528.

[4.6.9] R.A. Bosch et al., "Robinson Instabilities with a Higher-Harmonic Cavity," Phys Rev ST-AB **4**, p. 74401 (2001).

[4.6.10] M. de Jong et al., J. Microwave Power Electromagnetic Energy, **27**:136-142, 1992.

[4.6.11] M. Jensen et al., "First Results of the IOT Based 300 kW 500 MHz amplifier for the Diamond Light Source," PAC 2005, Knoxville, TN.

[4.6.12] F. Perez et al., "New Developments for the RF System of the ALBA Storage Ring," EPAC 2006, Edinburgh, Scotland.

[4.6.13] P. Marchand, et al., "High Power (35 kW and 190 kW) 352 MHz Solid State Amplifiers for the SOLEIL Synchrotron," PAC 2005, Knoxville, TN.

[4.6.14] Hanspeter Vogel, ACCEL. Private communication.

[4.6.15] M. Svandrlik, et al., "The Super-3HC Project: An Idle Superconducting Harmonic Cavity for Bunch Length Manipulation," EPAC 2000.

[4.6.16] S. Simrock, "Digital Low-Level RF Controls for the Future Superconducting Linear Colliders," PAC 2005, Knoxville, TN.

[4.6.17] C.W. Horrabin, and D.M. Dykes, "Diamond Low Power RF System," EPAC 96.

[4.6.18] J.M. Brennan et al., "RHIC RF beam control," EPAC-2001.

[4.6.19] M. Liepe, S. Belomestnykh, et al., "A New Digital Control System for CESR-C and the Cornell ERL," PAC 2003, Portland, OR.

[4.6.20] http://recycle.lbl.gov/llrf4/

4.7 Cryogenic Systems

4.7.1 Cryogenics System Overview

A helium closed-cycle cryogenic system is necessary to provide liquid helium to the Superconducting Radio Frequency (SRF) cavities. Baseline operation will require two 500 MHz (fundamental) and one double cell, 1500 MHz (harmonic) SRF modules which must be maintained at approximately 4.5K during operation of the storage ring. An identical configuration will be required for full operation at later date. Therefore, the cryogenic plant is sized versatile to accommodate sufficient cooling capacity for eventual full operation, four 500 MHz and two 1500 MHz SRF modules. The cryogenic system includes a refrigerator/liquefier cold box, a main compressor and a recovery compressor with oil removal systems, One LHe dewar, one valve box, liquid helium (LHe) and liquid nitrogen (LN2) transfer lines, gaseous helium (GHe) storage tanks, and a GHe management system, instrumentation, controls, and safety devices. Each 500 MHz and 1500 MHz module has 500L and 60L storage capacities, respectively, and runs with 400L and 50L He during operation.

4.7.2 Factors Influencing Cryogenic System Design

4.7.2.1 Single versus Multiple Refrigerators

The refrigeration system needs to have high reliability with near-zero unscheduled downtime. Using risk and failure analysis criteria, a study to determine the source of unavailability was undertaken in the past by the TESLA collaboration at DESY, with results shown in Table 4.7.1 in the order of their occurrence frequency.

Table 4.7.1. Rating of refrigerator system unavailability.

Rating	Topic	Example	Multiple Refrigerators
1	External Utility Failure	Electrical power, cooling water, instrument failure	No advantage
2	Blockage by frozen gas or impurities	Air and/or water vapor	Somewhat larger risk tolerance provided
3	Operational problems	Operators, controls, instrumentation,	Greater risk due to more system complexity
4	Single component failure not leading to total plant shutdown	Electrical motor burnout, compressor bearings, leaking oil pump seal, turbine bearing trouble	No advantage over component redundancy within a single refrigerator
5	Catastrophic component failure leading to plant shutdown	Loss of insulation vacuum, rupture of heat exchanger, oil spill into cold process piping	Would have a positive effect

The information in this table suggests that major downtimes are likely to occur as a result of catastrophic component failure; the effect of any of the other four occurrences is relatively negligible. Therefore, we selected a single refrigerator with a full inventory of spare critical components. Also, we will develop procedures that follow the manufacturer's recommended maintenance schedule.

4.7.2.2 Partial versus Full Loads

The reliability factor is increased by designing refrigerators that are capable of operating efficiently at partial load. When the accelerator is operated at reduced load, or when all modules are not in use, the electrical power and utility usage will be proportionally reduced. This could be achieved in two ways, operating the cold box (CB) without a LN2 pre-cooler during the baseline operation and by automatically

varying the speed of the compressor (and therefore mass flow rate of the main compressors) by incorporating a variable frequency driver (VFD) system.

4.7.2.3 With or Without Gas Purity Monitoring System

Gas impurities have an adverse effect on R/L efficiency. Air, for instance, solidifies at approximately 50K. Small solidified air particles can damage the expansion turbine, which runs at a high rotational speed; thus the concentration of impurities in the helium gas must be maintained at less than 10 ppm. The R/L internal dual 80K absorbers, coupled with a constant gas purity monitoring system, will serve as the main source of purification and as the feedback system. No external purifier has been considered, since a redundant internal adsorber with automatic reactivation and switch-over features is judged to be cost effective and the reliability is not compromised.

4.7.2.4 Heat Load Budget

There are two types of heat loads: static which come from thermal conduction and radiation, and dynamic which result from beam operation. The static heat loads of the SRF cavity cryostats are based on measured values of similar cryostats in other synchrotron facilities. The dynamic heat loads are calculated based on physics requirements. Heat loads associated with transfer lines, valve boxes, dewar losses, and other components are combination of estimated values based on information provided by vendors, engineering calculations, and professional judgment. Table 2 itemizes the estimated static and dynamic heat loads of the superconducting cavities and associated cryogenic components at 4.5K for both baseline and full operation.

The projected LN2 required by the R/L pre-cooler heat exchanger and other components heat shields is listed in Table 4.7.2 for both the initial and full system.

Table 4.7.2 Liquid nitrogen consumption estimates.

Component(s)	Per Cavity [L/hr]	Two Cavities + 1 Harmonic [L/hr]	Four Cavities + 2 Harmonic [L/hr]
500 MHz cavity	10	20	40
Harmonic cavities	10	10	20
Cold Box		23	45
RF valve box	_	12	24
Transfer lines (1 W/m), 50 m	-	2	4
Subtotal		67	133
Margin (20% of subtotal)		14	27
Total		81	160

The waveguides of each 500 MHz and 1500 MHz cavity require 0.134 g/s and 0.174 g/s of cold helium for cooling, respectively (Table 4.7.3). These are the liquefaction load to the R/L, and are equivalent to 4 L/hr and 5.2 L/hr of liquid helium. Therefore the liquefaction loads for the baseline and full operation are 13.2 L/hr and 26.5, L/hr, respectively.

Table 4.7.3 Heat loads budget and refrigeration sizing.

Cryo-Plant Heat Load Baseline Budget	Per Cavity	2 Cav. + 1 harm	4 Cav. + 2 harm
		(Baseline)	(Full Operation)
Number of Harmonic 1500MHz RF (X)	1	1.00	2
Number of 500MHz RF (Y)	1	2.00	4
Total Number (Z)	1	3.00	6
500MHZ Cavity Operation		3.3MV/2	5MV/4
Q (*10^9)		0.75	0.75
Background Heat Load			
Cavity beamtubes (RBT + FBT)*Y	13.8	27.60	55.2
Cavity Waveguide (conduction)*X	5.3	10.60	21.2
Waveguide cooling (0.134 g/s)*X	13.4	26.80	53.6
Cavity Rad. LN2 to Lhe (No MLI)*X	8.1	16.20	32.4
Harmonic (17.0W + 0.171 g/s)*Y	34.1	34.10	68.2
40, 80m Xfer Lines *(0.2W/m)*	*8.0*	*8.00*	*16.0*
2*1.6*Y*5m Xfer Line *(1.6W/m)*	*16.0*	*48.00*	*96.0*
Dewar Loss (static, Dynamic)	5.0	10.00	10.0
(Z*5W) SRF Valve Box; He only	5	15.00	30
Background TOTAL	108.7	196.30	382.6
150% background TOTAL	163.1	294.50	573.9
Dynamic Heat Leak			
V^2/(89*Qo), 10^9)		81.60	93.6
Harmonic Cavity	*22.0*	*22.00*	*44.0*
TOTAL	22	103.60	137.6
150% TOTAL	33	155.40	206.4
Standby/CD, Beam-off Load, W	108.7	196.30	382.6
Margin, 900 W R/L OP. W	791.3	703.70	517.4
Margin, 900 W R/L OP. Percent (%)	728.0	358.50	135.2
Available Liquefaction, LPH	197.8	175.90	129.4
Recover 400 Litters, Hours	2.0	2.30	3.1
Standby/CD, 150% Beam-off Load, W	163.1	294.50	573.9
Margin, 900 W R/L OP. W	737.0	605.60	326.1
Margin, 900 W R/L OP. Percent (%)	452.0	205.70	56.8
Available Liquefaction, LPH	184.2	151.40	81.5
Recover 400 Litters, Hours	2.2	2.70	4.2
Beam-on Grand Total Load, W	130.7	299.90	520.2
Margin, 900 W R/L OP. W	769.3	600.10	379.8
Margin, 900 W R/L OP. Persent (%)	588.6	200.10	73.0
Available Liquefaction, LPH	192.3	150.00	95.0
Recover 400 Litters, Hours	2.1	2.70	4.2
Beam-on, 150% Grand Total Load, W	196.1	449.90	780.3
Margin, 900 W R/L OP. W	704.0	450.20	119.7
Margin, 900 W R/L OP. Persent (%)	78.2	50.00	13.3
Available Liquefaction, LPH	176.0	112.50	29.9
Recover 400 Litters, Hours	2.3	3.60	13.4
100% Refrigeration, W	900.0		
100% Liguefaction, g/s (Linde)	7.5		
100% Liquefaction, 1ph (Linde)	225.0		

4.7.4 Design Approach

The main storage ring RF systems will initially consist of two 500 MHz (fundamental) cavities and one 1500 MHz (harmonic) Superconducting RF cavity. The cryogenic system must operate continuously for at least a full year before scheduled downtime. The design goal, therefore, was to provide a highly reliable and stable cryogenic system supported with required monitoring, alarms, interlocks, safety devices, and control system. As the cryogenic system must supply LHe to all of the RF cavities, redundancy of vulnerable components was considered, to ensure that continuous operations can be maintained effectively.

Total refrigeration cooling requirements were based on two sets of operating conditions: an initial baseline, and eventual full operations. Note that the cooling requirements for the full operation condition is approximately doubled compared with the baseline, since identical static loads are the dominant factor (Table 4.7.2). Therefore, the cryogenic system must minimally provide refrigeration power of 299.9W during baseline operation and 520.2W for the eventual full operating conditions. The Refrigerator–Liquefier (R/L) is oversized (150% margin) to enhance reliability and account for contingencies on additional heat loads that may develop during detail design.

The SCRF modules are planned to be situated in two neighboring straight sections of the storage ring, 50 m apart in two groups of three SRF cavities: two 500 MHz fundamental cavities and one 1500 Mhz harmonic cavity.

The SRF cryogenic system General Arrangement (GA) shown in Figure 4.7.1 depicts the full operating condition with capability to run at baseline. The design approach is primarily based on commercial helium R/L CB, main and recovery compressors, Variable Frequency Drivers, oil removals, helium dewars, and gas management systems. The design of the transfer lines, warm pipes, valve box, and control system will be defined during detailed system design.

General Arrangement considerations define distribution lines of equal length, locating the source LHe dewar at the approximate center of the 50 m (i.e., 25 m laterally from each module group). The distribution/return lines are listed in Table 4.7.4.

Table 4.7.4 Distribution of Source/Return Lines

Lines Description	Source/Return
Liquid Helium, 4.4K saturated	LHe dewar
Helium Vapor Return	Cold Box
Liquid Nitrogen, saturated at 25 psig	Phase Separator
Cool-down/Recovery:	
Warm-up, power failure	Cold Box or Ambient Vapr
W Pump and Purge, utility vacuum	Utility Vacuum System
LP Warm Return, e.g., vapor cooled	Compressor Suction
Nitrogen exhaust, vents to atmosphere	Valve Box Vent

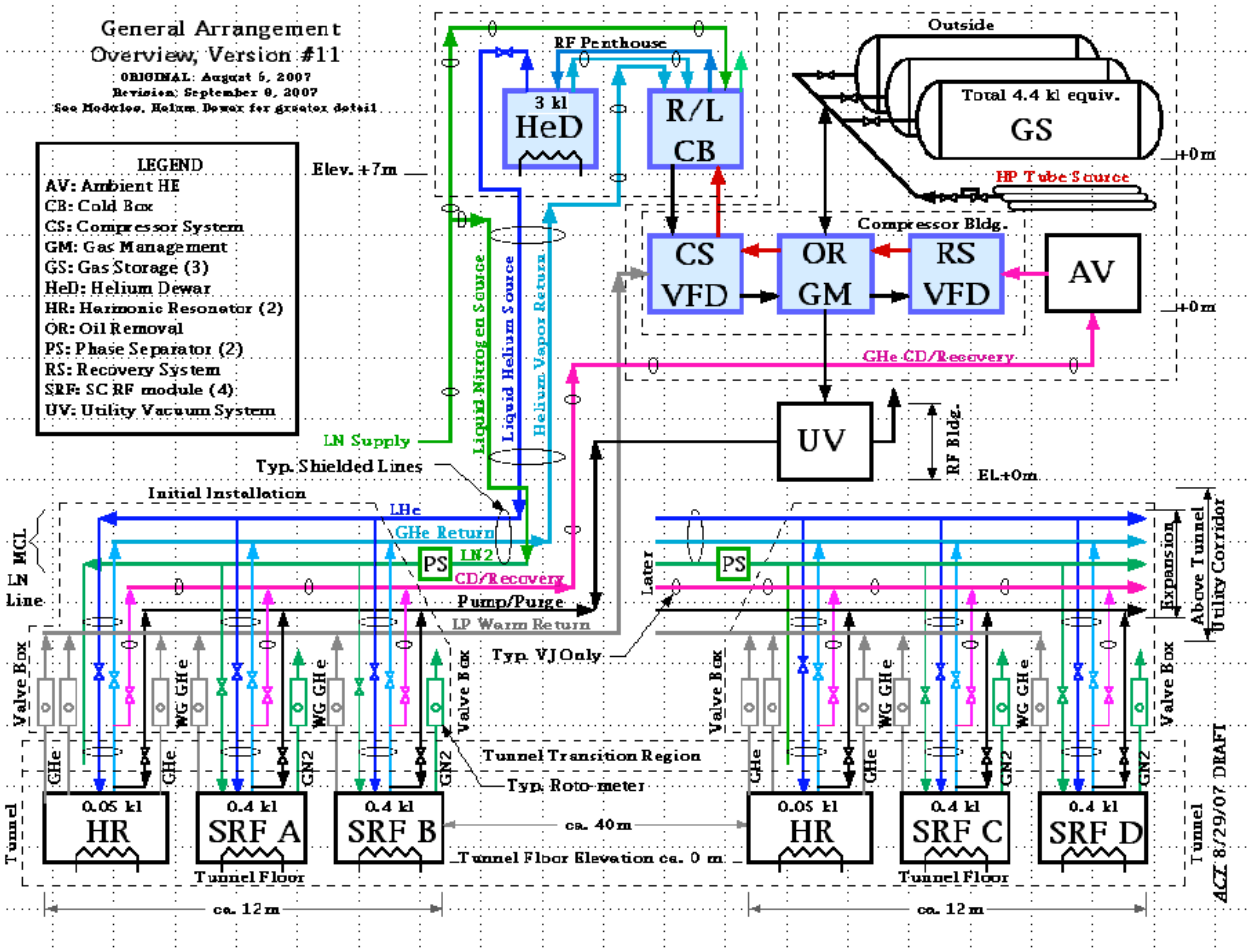

Figure 4.7.1 SRF Cryogenic, General Arrangement (GA)

Lines a, b, and c are arranged so the liquid nitrogen flow radiation-shields the He lines, and all are contained in a common insulating vacuum jacket. The CESR creators of this arrangement have dubbed this configuration, as implemented with VCR and Conflat fittings at the ends of each section, the Multi-Channel Line (MCL).

The Cool-down and Recovery line, d, provides for temporary flows and may be efficiently provided as a standard, standalone, and relatively inexpensive vacuum-jacketed transfer line commonly used for liquid nitrogen. The recovery flows (loss of power, rapid warm-up), are diverted from the cold box to an ambient vaporizer (which may be augmented with an electrical heater for extreme cold weather conditions) to assure that the recovery compressor suction stays sufficiently warm.

The Pump and Purge line, e, will be sized for efficient pumping speed with the specified Utility Vacuum System pumping speed. The Utility Vacuum System vacuum pump will be, for line size considerations and costs, located in the RF building near the tunnel straight section middle.

The Low Pressure (LP) return line, f, collects and returns GHe from the waveguide and other warm-return flows to the compressor suction.

The cryostats' LN2 shield is vented to the outside tunnel with a gaseous nitrogen exit temperature sensor and a modest flow control.

Isolation and removal of a warmed module from an otherwise cold system in standby situation will requires absolutely tight shutoff valves and the necessary procedures to verify their tightness. The safe

installation and operation procedure will be developed during detail design. However, clearly, all of the Valve Box valves will be normally in closed position, i.e., “fails closed” in the event of loss of signal or power. The operation of all essential components (such as control valve signals) will be hooked to the emergency power system in case of main power failure. Full descriptions of each subsystem are given in the following sections.

4.7.5 SRF Modules, System Layout

The two 500 MHz (fundamental) and one double-cell 1500 MHz (harmonic) SRF modules will occupy a single straight section. A designated space in the adjacent long straight section is planned for identical configuration for the fully built-out machine. These two neighboring straight sections are near the linac and the control room.

The cold box and the LHe dewar is planned to be located in a mezzanine deliberately placed almost at equal distance from each straight section. The valve box(es) will be located on the tunnel’s roof, connected to the LHe via MCL and the modules via single VJ lines.

The compressor room, gas management buffer tanks, and LN2 dewar will be in a area detached from the main building to isolate induced vibration and noise.

Another room adjacent to the cryogenic and power supply rooms is planned for testing SRF modules prior to installation, for troubleshooting, and for R&D purposes.

Currently, four rooms are dedicated to the RF power supplies and cryogenic systems. These rooms will be adjacent to the RF straight sections, minimizing the waveguide length and heat load from the helium transfer lines between the cryogenic room and SRF modules. Two power supply rooms are directly adjacent to each RF straight section. The cryogenic room houses the refrigerator, LHe dewar, inter-connecting transfer lines, multi-channel distributing manifolds, and local control system. The adjacent RF test room is dedicated for pre-installation testing and R&D purposes.

4.7.6 Refrigerator-Liquefier (R/L) Cold Box

For long term reliability with minimum maintenance, commercial R/L with gas bearing turbines will be used. Furthermore, the R/L shall be capable of operating over a large range of loads as required by the project. Comprehensive interaction with the potential vendors during this design stage has been conducted to insure best match between the system performance and operation requirements. The Linde LR280 R/L, shown in Figure 4.7.2, together with a variable frequency driven compressor (ESD441), is found to meet the present application and is used for illustration. Other potential vendors also have R/Ls of very similar characteristics.

As shown in Table 4.7.2, the expected heat load is 520 W for eventual full operation, to run four 500MHz and two 1,500MHz cavities simultaneously (with a 1.5 safety factor, the load could be 780 W). Thus, a 900W refrigerator is considered the best commercially available R/L system. For baseline operation, the expected heat load is 300 W (450 W with a 1.5 safety factor). The 900W refrigerator must be turned down to 450 W during baseline operation and to preferably to as low as 300 W in order to minimize operating costs. The excess refrigeration that can’t be turned down must be “burned” by a heater added to the LHe dewar to provide an artificial load; this is admittedly an inefficient solution.

Figure 4.7.2. Typical R/L cold box.

The Linde LR280/ESD441 is a 900W cooler at 4.4K, with three-turbines whose refrigeration can be turned down to 640 W by turning off the LN2, and by another 50% to 320 W by the use of a Variable Frequency Drive (VFD). The capacity curve for refrigeration vs. liquefaction is given in Figure 4.7.3. That almost meets the refrigeration requirements outlined above and seems an acceptable refrigeration turndown solution. However, a serious consideration has been made for the liquefaction component of the load, and especially in any case without LN2 (elaborated below). Note that the large, single R/L system solution is the most cost effective of all those considered, provided that it can demonstrate a successful (operational and cost effective) turndown capability.

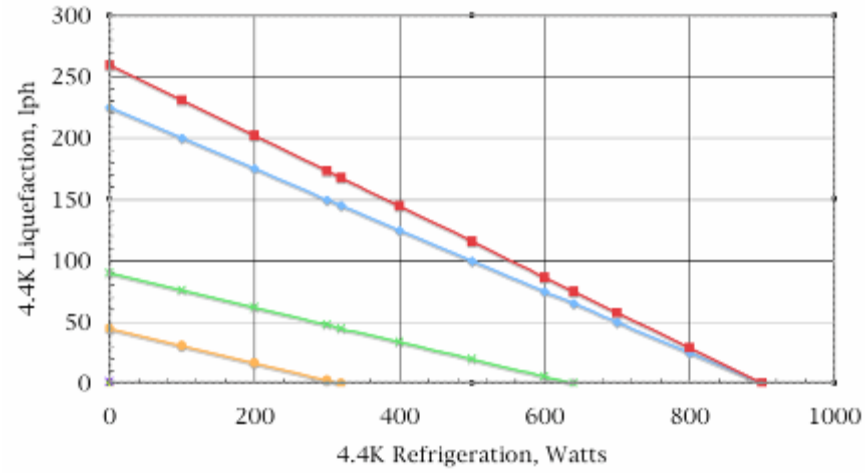

Figure 4.7.3 Liquefaction vs. refrigeration for LR280.

Red represents R/L with LN2 and assumed 100 W/g/s.

Blue represents R/L with LN2 and supplied data by Linde.

Green represents R/L without LN2 and data supplied by Linde.

Orange represents R/L without LN2 at 50% VFD, estimated by Linde.

4.7.6.1 Special Turndown Consideration

The turndown refrigeration capability of the R/L is very desirable in the current application to efficiently address the initial half-system operation. Unfortunately, a major turndown mechanism, the removal of the LN2, seriously cripples the liquefaction capability in the face of a small yet substantial liquefaction load. That means that the sum of the liquefaction loads presented to the R/L operating without LN2 is a far greater burden than that operating with LN2.

A possible solution of modulating (load tracks) of the LN2 pre-cooling with the load for turndown (rather than just turn it "off"), will be examined during the detailed design. The first order approach to modulated LN2 cooling would be to leave the LN2 "on" while turning the VFD down. the 900W unit should be able to turn down to ~450 W (VFD to 50% speed/flow) in that way. A similar VFD turndown to 40% (assuming it is possible to turn down from 60 Hz to 24 Hz) speed/flow might get close to 360 W. At the 360W level, the excess refrigeration available in the half-system will be quite small in full operation, and the excess power costs too small to be of concern.

4.7.6.2 Main Compressor System

All potential suppliers of the R/L use an oil screw compressor manufactured by Kaeser (Figure 4.7.4). Two ESD441 type compressors (one as hot standby) will provide the required 80 g/s flow at 15 bar absolute for the 900W R/L. The compressor skid consists of a bulk oil separator, a gas cooler, two stages of coalescers, an adsorber, and an oil cooler. The oil cooler is used to cool oil from the bulk oil separator for re-injection to the compressor.

Each compressor will be equipped with a Variable Frequency Driver (VFD), housed in an external cabinet. The drive motor of the compressor package is capable of varying speed between 20 Hz to 60 Hz (corresponding to one-third to full flow).

The screw compressors are low-vibration machines that normally do not require massive foundations. Vibration dampers, however, will be identified and implemented at the time of installation. All compressors will be housed in a separate building away from the main building to eliminate any possible vibration transmittal.

4.7.6.3 Recovery Compressor System

A smaller screw compressor, 12 g/s mass flow, will be used to pump boil-off helium to storage tanks in case of a power failure. This recovery compressor is to be equipped with uninterrupted power supply and automatically start. This compressor will have same pressure characteristics as the main compressor. The start time of emergency power will be about 20 s, to avoid the difficulty of starting at high suction pressure.

Figure 4.7.4 Typical Kaeser helium compressor.

4.7.7 Liquid Helium Dewar

The LHe dewar is the repository of the stored LHe heat of vaporization and concurrently the cooling source for the LHe cooled loads. Most of the R/L load is a refrigeration load; the condensed liquid is evaporated at the load and the returned cold vapor is utilized to create new liquid in a continuous R/L loop. A small portion of the R/L load, the waveguide heat intercept of the 500 MHz cavities and all the beam tube conduction and radiation cooling of the 1500 MHz cavities are in liquefaction loads (i.e., LHe is evaporated, warmed to room temperature and returned directly to the compressor suction).

The He dewar capacity has been set at 3,000 liters to 1) contain liquid inventory needed at any one time; 2) store liquid for limited period deficit (loads larger than the available refrigeration of rapid filling) operations; and 3) as a repository for recondensed and accumulated liquid in anticipation of its protracted, excessive, use. Helium operating inventory is 400 liters per SCRF CESR-B and an assumed 50 liters per Harmonic Resonator module, for a total of 1,600+2(50) = 1,700 L. An operating storage level of 500 to 1,000 L would provide the space for a 3,000L dewar to recover the entire cavity inventory as liquid (desirable in a short-term scenario), with a margin for the significant mass of saturated He vapor in a mostly empty dewar. See Table 4.7.4 for the system inventory.

Table 4.7.4 Helium system inventory.

Nominal inventory, liquid helium (liters equiv.)	250 psig ASME gas storage	3,000 liter 1% LHe dewar	4+2 cryostats cap. = 1.7 kl	HP Source, standby trailer
Warm	>3,500	0	0	$\geq$1,200
Standby	1,000	2,500	0	$\geq$1,200
Operate	1,000	800	1,700	$\geq$1,200
Shutdown	>3,500	0	0	$\geq$1,200

The He dewar will be specified as a required part of the R/L vendor supply to include the R/L connecting lines, an auxiliary inlet/outlet(s) (for feeding the dewar from an external source, should this be necessary), the dewar's heat leak rate, heaters, and instrumentation and control system. See Figure 4.7.5 for a schematic of a LHe dewar.

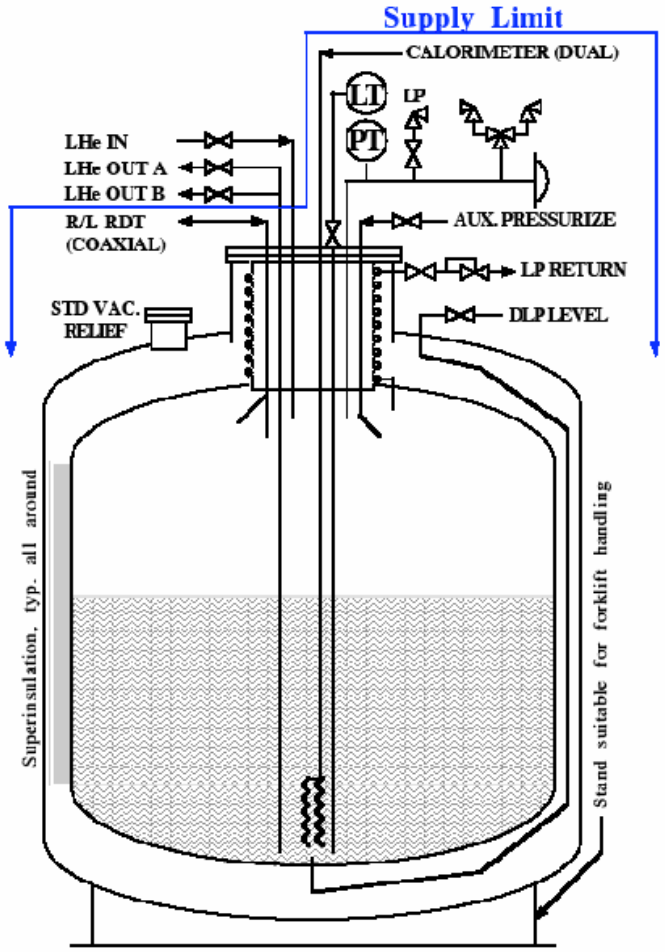

Figure 4.7.5 Schematic of the LHe dewar.

4.7.8 Liquid Nitrogen Dewar

A 10,000-gal LN2 dewar will supply LN2 to the SRF cryogenic plant. This dewar will be filled from the facility's LN2 storage tank via a vacuum-jacketed line with automatic fill control system. A LN2 Phase Separator will assure a single-phase flow to the SRF module at a constant pre-set pressure to support steady SCRF module shield and intercept cooling flows. The single phase and isothermal cooling at a constant (phase separator regulator controlled) pressure will contribute to predictable and reliable module liquid nitrogen cooling performance.

4.7.9 Gaseous Helium Storage Tanks

The warm gas storage water volume of about 6,250 scf (46,875 gal) will be sufficient to provide storage for an equivalent of 3,500 LHe to 14 bar pressure. Two 30,000 or three 20,000-gal tanks will have sufficient volume with room to spare. The total capacity of either these options is 14*60k/7.5/25 = 4,480 liquid liters equivalent.

These tanks will be designed for an internal pressure of 20 bar and external pressure of 1 bar. The maximum operating pressure is about 15 bar and the minimum operating pressure is estimated at 2 bar. The design specifications will include all appropriate ASME Boiler and Pressure Vessel Codes, Section VIII,

Divisions I (Unfired Pressure Vessels) and IX (Welding and Brazing Qualification), and Safety Relief Valves. Material and other geometric features will be detailed before purchasing.

One 30,000-scf HP gas trailer (capacity ~1,200 liquid liter equivalent) can serve as a continuous warm (no maintenance) standby storage.

4.7.10 Gas Management

Helium inventory in the refrigeration system is automatically adjusted by the gas management system as the refrigeration/ liquefaction load changes. The gas management system will consist of typically two control valves. One valve automatically sends excess helium to the buffers (for example, during quenches or warm-ups) One valve adds helium to the system from the buffer tank when the liquefaction capacity is higher than flow recovered from loads.

These two valves work in concert with the bypass recycle valve, which automatically recycles excess flow from compressor discharge to suction. These two valves maintains proper amount of helium in the system according to variation in liquefaction or refrigeration rate of the R/L. A frequency driver will reduce the total cycle mass flow rate in case of excess flow from the compressors.

Pressure transmitters and indicators with analog or digital output will be installed on both the discharge and suction lines near the main compressors. Similar transmitters will be installed near the suction side of the distribution valves boxes. Safety relief valves shall be installed in both the suction and discharge line of the compressor.

Sufficient instrumentation ports with shut-off valves will be placed on both the discharge and suction lines in the compressor room and also on the high-pressure line near the refrigerators/liquefiers. The makeup/recovery control valves will be in the compressor room. Several other smaller ports will be located on both the discharge and suction lines of the compressors and oil removals for gauges, sensors, and gas sampling purposes.

4.7.10.1 Vacuum-Jacketed (VJ) Liquid Helium Transfer Lines

Single Channel Line (SCL) and Multi-Channel Lines (MCL) vacuum-jacketed cryogenic transfer lines will be used to transfer liquid or cold GHe among various components such as to/from the main LHe dewar, SRF distribution valve box, and SRF modules. These vacuum-jacketed lines will be constructed of high-quality seamless stainless steel tubing. The lines and mating connections will have minimum heat leak and will resist damage from thermal expansion and contraction.. The use of copper tubing to carry LN2 for cooling radiation shields will be permitted, provided the design conforms to all applicable codes.

In addition to combined pump-out/burst ports, the line will have pressure and temperature transmitters with digital or analog output signals for monitoring and interlock purposes.

4.7.10.2 Vacuum-Jacketed Liquid Nitrogen Transfer Lines

Different sizes of the LN2 transfer lines will require transferring appropriate flow rate among inter-connecting components. The fill line between the outside main LN2 tank and the SRF LN2 dewar located near cryogenic plant will be vacuum jacketed (reduce the cool-down consumption and added enhance safety) capable of handling large flow rate of 400 L/hr at 4 bar head pressure. The interconnecting lines between the SRF LN2 dewar and cryogenic equipment (L/R, valve box, LHe transfer lines, heat shields, SRF modules) will be designed as rigid and flexible lines with heat leak to be less than 0.5 W/m at 80K (exclusive of valves

and bayonets). The insulating vacuum space of the lines will take into account the relative humidity factor, dew point, and seasonal temperature variations to ensure it is condensation free at all times.

Suitable keep-full valves will be installed along the fixed lines to ensure single-phase liquid flow to designated components when pressure stability is essential (e.g., SRF modules). An insertion of a LN2 phase separator before the SRF modules will insure pressure stability requirements of cavities. Similar to LHe transfer lines, these lines will also have pressure and temperature transmitters with digital or analog output signals for monitoring and interlock.

4.7.10.3 Warm Piping

In addition to vacuum jacketed lines, there are three sets of piping for warm helium:

- One suction line to transfer low-pressure helium gas from SRF modules (waveguides), valve boxes, to compressor's suction.
- one discharge line to transfer high-pressure helium gas from the main/recovery compressors to oil removals, and to either the refrigerators/liquefiers cold box or gaseous storage tanks
- one makeup/recovery line between suction/discharge of the compressors and GHe storage tanks.

These lines will be sized and designed according to the flow rate, allowable pressure drop and operating pressure and temperature conditions. Seamless Stainless Steel tubing/pipes, 304 or 304 L, will be used and constructed in conformance with all applicable codes.

4.7.10.4 Power Failure Considerations

Cryogenic systems are susceptible to damage from abrupt power losses. Loss of electrical power could cause an unexpected system shutdown which would require continuous operation of the recovery compressor to recover generated boiled-off GHe to the helium storage tanks. The recovery compressor, main helium dewars, cryogenic distribution valve box, and the cryogenic electronics of the SRF modules require a sufficient source of emergency power, as does the Oxygen Deficiency Monitoring systems, which must have an Uninterruptible Power Supply (UPS) system. A 50 KW emergency power generator is dedicated to the cryogenic system.

The demands of He inventory recovery in the case of a protracted (greater than 10 minutes) power failure is shown in Table 4.7.5.

Table 4.7.5 He inventory recovery demand during protracted (>10 min.) power failure.

LHe, Cool Time	Units	500 MHz	1500 MHz	LHe dewar
Operating Volume	Liters	400	50	800
Quant. LHe liters	Liters	1600	100	800
HOV Available	Joules	3.65E+06	2.28E+05	1.82E+06
Unit LHe Load	Watts	40.6	34.1	5.0
LHe Load, total	Watts	162.4	68.2	5
Self Cooled	Hours	6.24	0.93	101.33

4.7.10.5 Ambient Vaporizer

Power outages are most likely to create the largest recovery flow rates. An Ambient Vaporizer (AV), capable of handling ~288 l/h (~10 g/s) cold GHe flow to warm-up the temperatures for safe operation of the compressors will be used.

4.7.10.6 Valve Boxes

Two valve boxes are eventually required for full operation condition. One located near each RF straight sector location. One MCL (two total) will transfer both LHe and LN2 to each of the two VB(s) (one for the baseline condition). Individual transfer lines, most likely flexible type, will be provided between each VB and the individual SRF modules.

A tentative 15 valve-arrangement package in a horizontal rectangular enclosure is shown in Figure 4.7.6. A total of 12 valves, three LHe feeds, three GHe returns, three helium cool-downs, and three LN2s is required per GA at this stage.

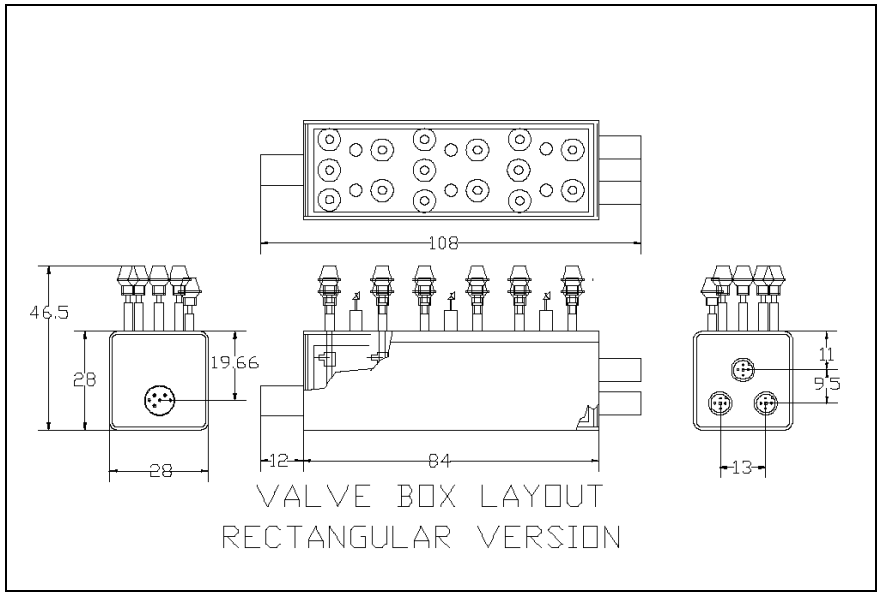

Figure 4.7.6 Tentative valve box arrangements.

4.7.10.7 Operating Modes

Process provisions for the complete installation/operation cycle must support the SCRF module operating modes as follows:

1. Independent Module Connection
2. Independent Pressure Test and Leak Check
3. Independent Pump and purge
4. Independent Liquid Nitrogen Cool-down
5. Independent Liquid Helium Cool-down and Fill
6. Independently Establish Readiness for Stable Operation
7. Independent Isolation and/or Warm up

4.7.10.8 Independent Module Connection

Although the SCRF modules have common feed and return manifolds, their inline isolation valves within the valve box (fully closed and secured) can create a complete isolation from all other modules. All transfer lines between the modules and the valve box will have separate vacuum with mating bayonets for installation.

4.7.10.9 Pressure Test and Leak Check

Each module upon complete connection shall be pressure tested and leak checked for safe operation. Only when these operations are successfully accomplished can a module considered ready for pump and purge.

4.7.10.10 Pump and Purge

Each module shall be pumped and purged to strict criteria to protect the system from impurities. System contamination can dramatically undermine and/or preclude the designed performance of an otherwise reliable system.

4.7.10.11 Liquid Nitrogen Cool-down (To about 200K)

The LHe cool-down is accomplished by activating the module's liquid nitrogen shield and intercept flows. The radiation shield isolates, and the intercepts reduce, the conduction to the He temperature cold mass from the ambient world, providing cooling. After ~48 hours (in the case of routine CESR operation of a similar system), the module can be cooled to 200K by this arrangement. The cooling progress slows dramatically below 200K. That temperature value is the suggested benchmark to initiate the second and final stage He cool-down to 4K. Finally, the module is filled with liquid helium and the operating level is established and continuously maintained in automatic mode.

4.7.10.12 Liquid Helium Cool-down to 4.5K and Fill

The standard cool-down procedure accumulates liquid using the available liquefaction capacity and then consumes the liquid heat of vaporization and sensible heat (where appropriate) to cool the load. If the cool-down rate consumes liquid at a rate greater than liquid can be produced by the R/L, the main compressor pumps the excess mass to warm gas storage for later liquefaction. To put the issue in quantitative terms, the excess consumption over liquefaction could easily reach as high as 200 L/h, or about 6.7 g/sec, well within the recovery compressor's capability.

The recovery compressor can be seen to connect to provide cool-down and recovery directly via the CD/Recovery line and an ambient vaporizer outside of the gray dotted lines, as shown in the Figure 4.7.7 block diagram.

If the recovery compressor is to do a lot of standby or variable flow pumping it should be fitted with a VFD that simply reduces the RPM whenever the bypass valve opens and increases the RPM when it is closed. Supervisory logic can decide when it is useful to turn it on and off outside of the hard-wired power failure recovery function.

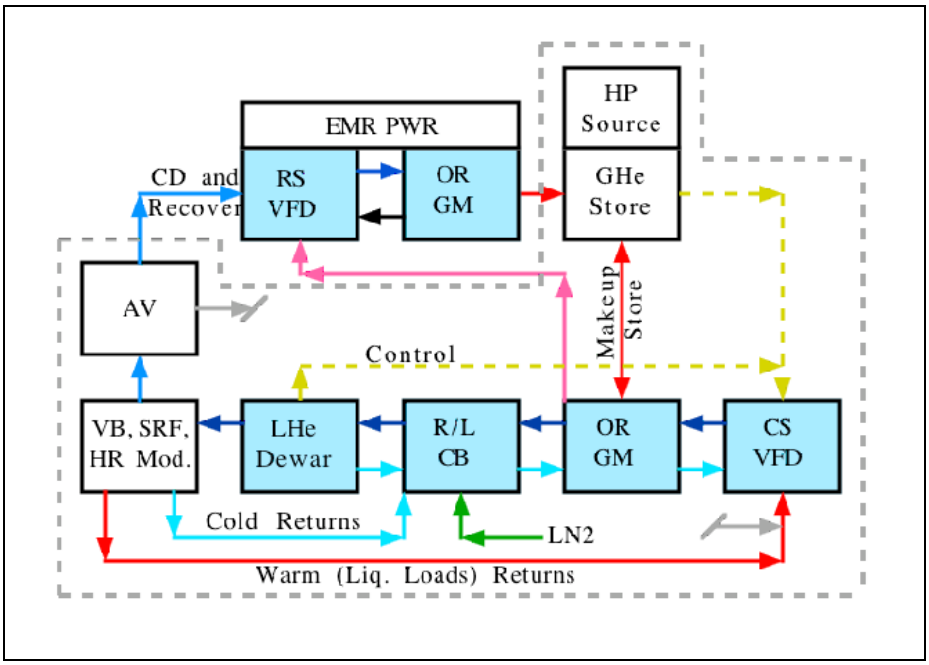

Figure 4.7.7 Compressors and gas management block diagram.

4.7.11 Establish Readiness for Stable Operation

Upon completion of cool-down to 4.5 K, each module is filled with 400 L of liquid helium or 80% of total volumetric capacity. The helium vessel's pressure, temperature and liquid level will be maintained at operating values and controlled by the local control system with monitoring and set-points accessible from the EPICS accelerator control system. The system is ready for operation when all pre-set parameters have been met and all safety interlocks are fully operational.

4.7.11.1 Independent Isolation and/or Warm up

300 K main SRF modules warm-up

This process isolates and warms-up the main SRF modules to ambient temperature, while the Main Cryogenic plant is cold. The liquid helium of the main SRF modules will boil-off by using cryostats DC (within 3 hrs) and recovered to the cold return line via the cryogenic distribution valve box and R/L cold box back to the compressor suction and gaseous helium tanks. The warm-up may include the cryogenic distribution valve box and main modules feed lines.

10-20 K main SRF modules warm-up

The main SRF modules is warmed in the same manner as the 300K warm-up, but only up to 10K to get rid of the magnetic flux trapping in the superconducting state by warming the niobium bulk cavity temperature higher than its critical temperature or up to 20K for RF window conditioning. The liquid nitrogen in the radiation shield flows continuously.

300 K Main Cryogenic Plan and main SRF modules warm-up

The main SRF module and Main Cryogenic Plant are both warmed to room temperature. The LHe dewar will, in general, continue to store liquid helium, but may be warmed as well.

300 K Main Cryogenic Plan awarm-up, cold main SRF modules

The Main Cryogenic Plant may be quickly warmed and then colled down to operating temperature again while the main SRF module is kept cold by liquid transfer from the liquid helium dewar.

4.7.12 Equipment Elevations

A study of He System Head vs. Location for locating the R/L,d LHe dewar and the valve box either at floor level or elevated to the tunnel roof was conducted, with results shown in Table 4.7.6.

Table 4.6.7 Various Equipment Location options.

Item/Case	Cold Box	LHe dewar	Valve Box	SRF Cryostat
Case A	HB Floor	HB Floor	HB Floor	Beam
Case B	HB Floor	HB Floor	Tunnel Roof	Beam
Case C	Tunnel Roof	Tunnel Roof	Tunnel Roof	Beam
Case D	Penthouse	Penthouse	Tunnel Roof	Beam

In the first case, A, the equipment is located on the High Bay (HB) floor. The second case, B, puts only the valve box on the tunnel roof. The third case, C, puts the cold box and the He dewar on the tunnel roof along with the valve box. The last case, D, puts the cold box and the LHe dewar on the penthouse level and keeps the valve box on the tunnel roof.

The cold box and LHe dewar can be at an elevated level, centralized between two straight sections, to provide a large (in LHe terms) LHe dewar liquid head (Figure 4.7.8). The elevated location allows gravity to help transfer LHe from the dewar to the valve box and cryostat below, without the need to significantly pressurize the dewar, as would otherwise be required.

The valve boxes will be located on the tunnel roof directly above each straight section joined to the LHe dewar independently, by independent MCL(s).

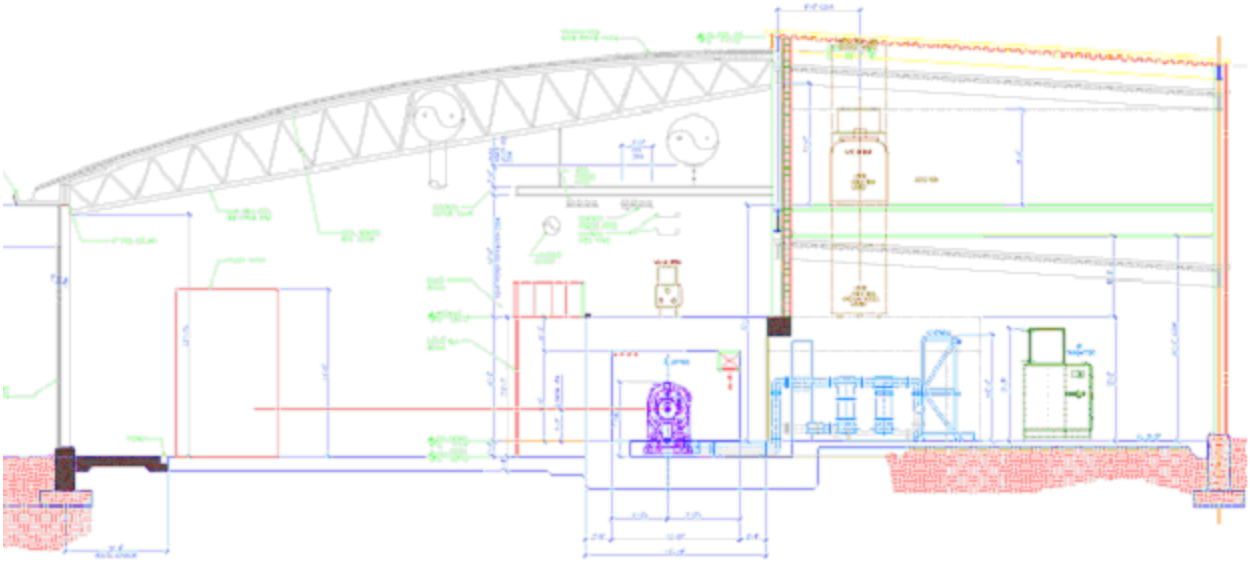

Figure 4.7.8. SRF Cryogenic system, elevation view.

The He dewar system head vs. different locations possibilities are tabulated in Figure 4.7.9. As a case in point, the dewar liquid head (see last entry in the first data column) of 1.531 psi is reduced by the cryostat liquid head (see the last entry in the cryostat column) of 0.240 psi, to provide the dewar-to-cryostat head of 1.291 psi. This is a respectable and constant LHe transfer pressure difference. Consequently, the R/L, LHe dewar, and valve box are planned to be on an elevated mezzanine with (sufficient overhead clearance), due to the highly technical advantage that case D represents. An alternative to this elevated equipment arrangement is to use a subcooler for stable LHe transfer throughout the system.

NSLS-II He System Head vs. Locations

Reference	Units	Dewar L	Dewar G	Cold Box	Cold Box	Valve Box	Cryostat
Helium		4.424K	4.424	313K GHe	300K GHe	4.424K	4.424K
Pressure		1.2	1.2	1.05 atm	13 atm	1.2	1.2
Density	g/cc	0.12080	0.02053	0.00016	0.00210	0.12080	0.12080
Density	kg/m^3	120.800	20.530	0.164	2.101	120.800	120.800
Normalized		738.665	125.536	1.000	12.847	738.665	738.665
Location		HB Flr	HB Flr	HB Flr	HB Flr	HB Flr	Beam
Service El.	m	1.500	1.500	2.600	2.600	1.500	1.397
Ref. Head	kg/m^2	181.200	30.795	0.425	5.463	181.200	168.758
Ref. Head	psi	0.257	0.044	0.001	0.008	0.257	0.240
Location		HB Flr	HB Flr	HB Flr	HB Flr	Roof	Beam
Service El.	m	1.500	1.500	2.600	2.600	5.640	1.397
Ref. Head	kg/m^2	181.200	30.795	0.425	5.463	681.337	168.758
Ref. Head	psi	0.257	0.044	0.001	0.008	0.968	0.240
		Tunnel	Tunnel	Tunnel	Tunnel	Tunnel	Beam
Location		Roof	Roof	Roof	Roof	Roof	Tunnel
Service El.	m	5.640	5.640	6.740	6.740	5.640	1.397
Ref. Head	kg/m^2	681.337	115.793	1.102	14.161	681.337	168.758
Ref. Head	psi	0.968	0.165	0.002	0.020	0.968	0.240
		Pent	Pent	Pent	Pent	Tunnel	Beam
Location		House	House	House	House	Roof	Tunnel
Service El.	m	8.917	8.917	10.017	10.017	5.640	1.397
Ref. Head	kg/m^2	1077.151	183.062	1.638	21.045	681.337	168.758
Ref. Head	psi	1.531	0.260	0.002	0.030	0.968	0.240

Figure 4.7.7. Helium system head vs different locations.

4.7.13 Instrumentation and Control

The functional analysis, consisting of the startup, shutdown, and regular and exceptional operating modes of the refrigerator will be written by the cryogenics engineer and then translated into the PLC logic for control of the refrigerator. This PLC must communicate with the PLCs embedded in the cold box, compressor, and cryo-module systems. In addition, there must be a seamless integration with the EPICS control system, allowing full control, monitoring, and history logging.

4.7.13.1 Oxygen Deficiency Hazard Monitoring and Control System

Oxygen Deficiency Hazards are present when atmospheric oxygen content falls below 19.5% by volume. The BNL Standard Based Management System has strict guidelines in compliance with the Occupational Safety and Health Administration Respiratory Protection Standard 29CRF1910.134, Table 4.7.8.

The main potential sources of reduced oxygen are from unplanned discharge of cryogens into confined spaces. Liquefied gases such as helium and nitrogen have the potential to cause ODH conditions, since expanded gases can displace air rapidly when released to the atmosphere.

For NSLS-II, a complete ODH analysis is required for each area (tunnel, cryogenic room, and compressor room), for all possible scenarios, in order to plan and put appropriate controls and measures in place. For the purpose of this report, an ODH classification of 1 is assumed, which among several requirements mandates the implementation of personal oxygen monitoring systems.

Table 4.7.8. ODH Control Measures.

	ODH Class				
Environmental Controls	**0**	**1**	**2**	**3**	**4**
1. Warning signs	■	■	■	■	■
2. Ventilation			■	■	■
3. ODH-Qualified Personnel Controls					
4. Medical approval as ODH-qualified		■	■	■	■
5. ODH training	■	■	■	■	■
6. Personal oxygen monitor		■	■	■	■
7. Self-rescue supplied atmosphere respirator		■	■	■	
8. Multiple personnel in communication			■		
9. Unexposed observer				■	■
10. Self-contained breathing apparatus					■

Gas monitoring systems, such as Safe T Net 410 (up to four channels), have been considered for installation in each area. These microprocessor-based controllers are designed to accept up to four combustible oxygen transmitters. Features include digital readout display, LED alarm indication, 4 to 20 mA output, individual low and high alarm, and relay signals for interlock purposes.

4.7.14 Preventive Maintenance Programs

The overall availability of the cryogenic system is defined as the ratio of the actual delivery time to the scheduled operating time. Synchrotron light source facilities are normally operated continuously, 24 hours per day, seven days a week, excluding short studies or maintenance periods and one or two extended periods of machine maintenance per year when the facility is shut down for preventative maintenance, upgrades, and repairs. This is necessary to decrease the number of unscheduled breakdowns. Routine preventive maintenance must therefore be conducted according to the manufacturers'

4.8 Beam Scrapers and Photon Absorbers

4.8.1 Beam Scrapers

Two pairs of electron beam scrapers will be used for accelerator physics measurements of the aperture and beam lifetime limits. The thickness must be ~$5X_o$ (radiation lengths) for the electron beam. The horizontal blades must be in the same plane and adjustable from full open (vacuum chamber width) to the chamber centerline with a resolution of ~1 μm and a reproducibility of ~5 μm. One location for the horizontal scrapers is in one of the dispersion regions next to the BPM and the SF2 sextupole, where there is high β_x and dispersion. The second location for horizontal scrapers is in the SID between the QL2 and SL2 sextupoles, the maximum β_x for the ring. The two vertical scrapers will be placed near the high β_y in the dispersion region (drift space at $\Delta\mu_y \sim\pi/2$ from the injection septum) and the LID (drift space at $\Delta\mu_y \sim 2\pi$ from the injection septum). These scrapers will provide controlled physical apertures to prevent large-amplitude particles (from the injector) from hitting the small-gap undulators, later in the ring. The scrapers will also provide defined apertures for understanding the dynamic aperture and lifetime in the ring.

4.8.1.1 Preliminary Design

To maximize their effectiveness as well as to simplify their engineering design, the two pairs of beam scrapers required will actually consist of four separate units: two horizontal and two vertical scrapers. These scrapers will serve as protective devices for the IDs. They will also be used as diagnostic tools during the commissioning phase and during machine studies.

Previous reports [4.8.1] have indicated that Touschek scattering is the dominant source of ID damage. Work done at APS has shown that scrapers should be located in a low-emittance lattice to effectively protect the IDs. This suggests that the horizontal scrapers should be installed where there is adequate dispersion at the scrapers as well as a large horizontal beta function. Touschek scattering presumably not only imparts a large energy deviation, but also induces large betatron oscillations for the scattered particles. A significant concern, however, is that the scrapers may compromise injection efficiency—or worst yet, may even produce more ID damage if the injected beam hits the scrapers, creating a shower that propagates to the IDs. To address this concern, we will carefully study the development work done at APS.

All four units planned for NSLS-II will share the same engineering design and be built identically—the horizontal and vertical scrapers differing only in the final mounting and installation. Each unit will have two jaws or blades that can move independently from one another, each being driven by precisely controlled stepping motors. The blades will be made of Glidcop, a dispersion-strengthened copper with excellent thermal and electrical properties at elevated temperatures. Each of the blade assemblies will have a water-cooling circuit to minimize thermal expansion of the blades when they are hit by the dipole radiation fan.

Furthermore, to minimize impedance problems, the shape of the blades will be determined by detailed numerical simulation. These studies are still in progress and the results are preliminary. Figures 4.8.1 and 4.8.2 show two views of the design of an existing scraper at APS. The NSLS-II scraper design will be based on this APS design, with appropriate modifications to match the chamber geometry. Figure 4.8.3 shows a preliminary layout of the possible NSLS-II scraper.

Each scraper unit will be mounted directly on the vacuum chamber and the adjustable blades can be repositioned remotely. Once they are in the desired position, however, they must stay in place within the required tolerance.

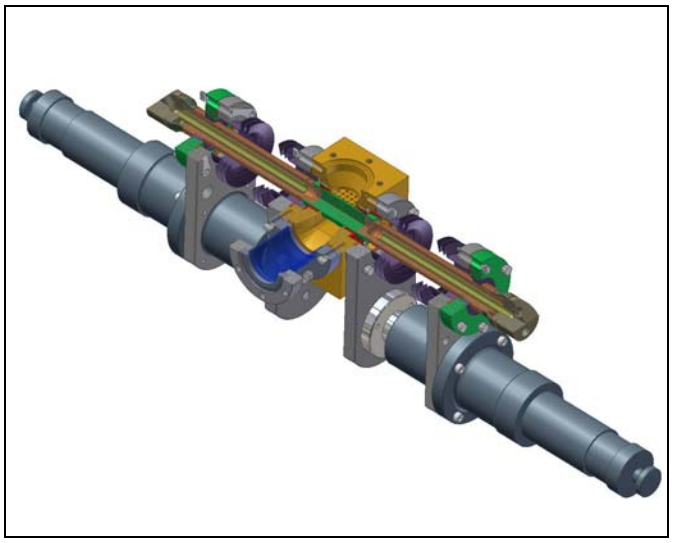

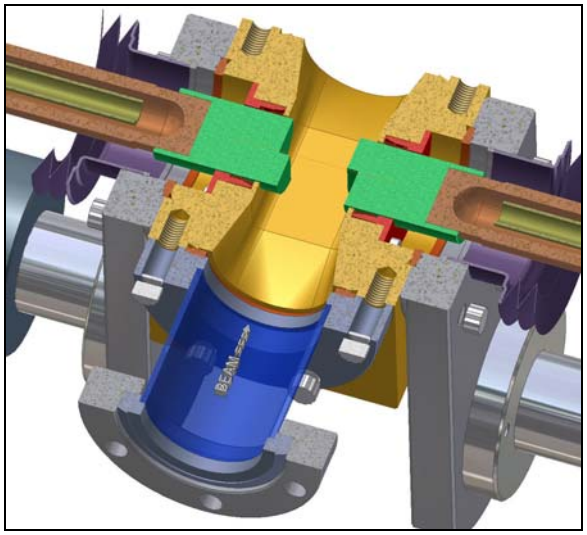

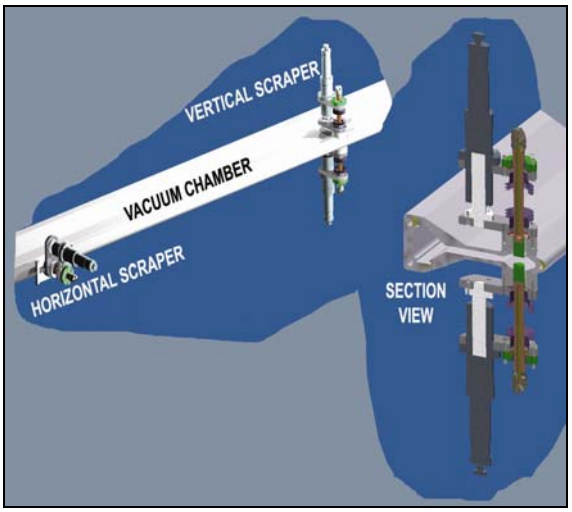

Figure 4.8.1 (top left) Sectional view of APS scraper assembly, round blades (closed).

Figure 4.8.2 (top right) Sectional view of APS scraper assembly, blades partially opened.

Figure 4.8.3 (right) Preliminary layout of NSLS-II scraper (two views)

4.8.2 Photon Absorbers

Discrete photon absorbers will be installed in the vacuum chambers to protect their uncooled surfaces from the radiation fans of the bending magnets and IDs. Shielding the vacuum chambers from radiation fans also minimizes their thermal distortions and leads to better thermal stability of the BPMs attached to the chambers. To protect the chambers from exposure to unintentional beam deviations, BPM interlocks at insertion devices will be set at ± 0.25 mrad [4.8.2]. The positional error budgets consisting of orbit error, mechanical, and survey tolerances will be set at ±2 mm.

The peak power densities of the bending magnets, damping wigglers, and the in-vacuum undulators (IVU) are 0.088 kW/mrad^2, 55.30 kW/mrad^2, and 62.33 kW/mrad^2, respectively, for a 500 mA beam at 3 GeV. The power density of the BM is uniform in its horizontal fan of 104.7 mrad (6º) except at the edges. For the DW and IVU devices, the vertical and the horizontal power density profiles are shown in Figure 4.8.4 and Figure 4.8.5 respectively.

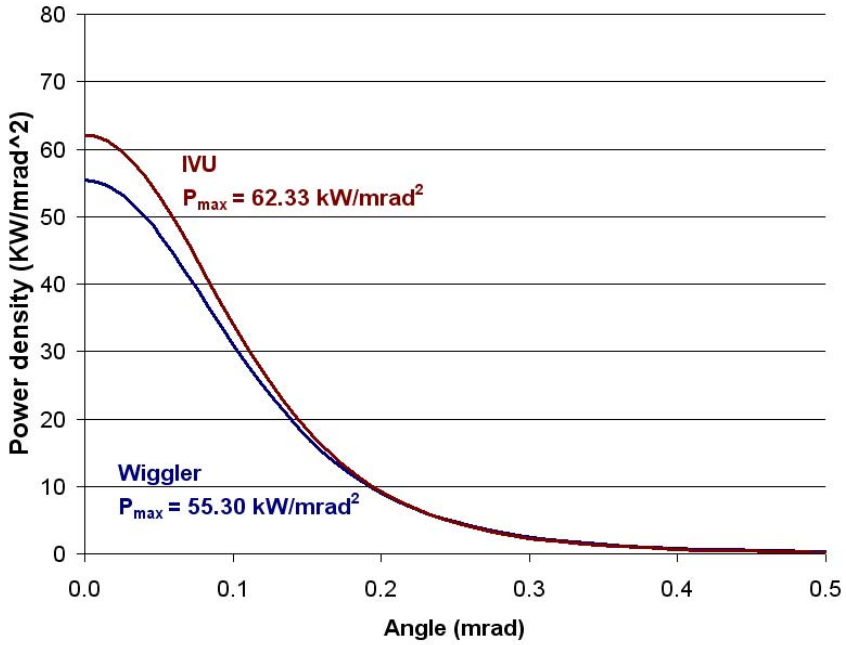

Figure 4.8.4 Vertical power density profiles, P/P_{max}, of damping wiggler and IVU. P_{max} is obtained at 500 mA beam current.

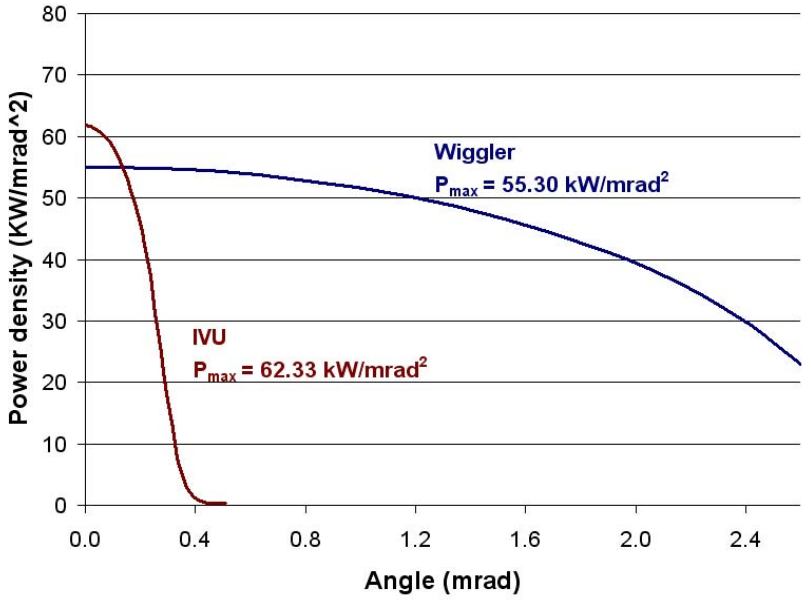

Figure 4.8.5 Horizontal power density profile, P/P_{max} for damping wiggler and IVU.

The IVU radiation fan is narrow in both directions and can be extracted with adequate clearance through the 76 mm (H) × 25 mm (V) apertures of the straight vacuum chamber in Section 2 and the 15 mm slot of the dipole chamber in Section 3. The BM and DW radiation fans in at the downstream end of Section 3 dipole chamber, however, require clipping by two absorbers, namely, a crotch absorber and a wiggler absorber (see Figure 4.8.6). Because of the high power density of the DW radiation, these absorbers clip the outer edges of the DW horizontal fan just enough to allow the clipped fan to be extracted to the front end.

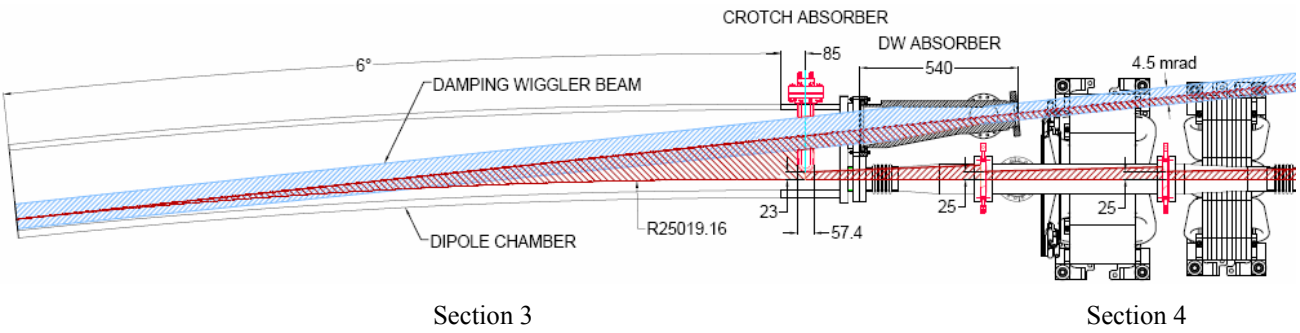

Figure 4.8.6 Clipping of BM and DW x-ray fans by crotch and wiggler absorbers in at the downstream end of the Section 3 dipole chamber. The BM radiation fan (blue color) partially overlaps the DW radiation fan (red color).

4.8.2.1 Preliminary Designs of Photon Absorbers

Figure 4.8.7a shows a 3D model of the crotch absorber inside the vacuum chamber. The absorber is made from a Glidcop® block with brazed water-cooling channels of OFHC copper. Also brazed to the Glidcop block are a stainless-steel flange and a water manifold. A rectangular slot in the center of this block allows DW or IVU radiation fans to pass through without interception.. The crotch absorber is inserted into the downstream aperture of the dipole vacuum chamber in Section 3 such that its nose tip is 5 mm inside the aperture (i.e., 30 mm outboard from the center of the aperture). The tip intercepts a total of 840 W of beam power with a maximum power density of 12 W/mm^2. A thermal analysis of the crotch absorber was carried out using ANSYS software. The results, plotted in Figure 4.8.7.b, show a peak temperature of 200ºC, which is lower than the maximum allowable temperature of 400ºC for Glidcop.

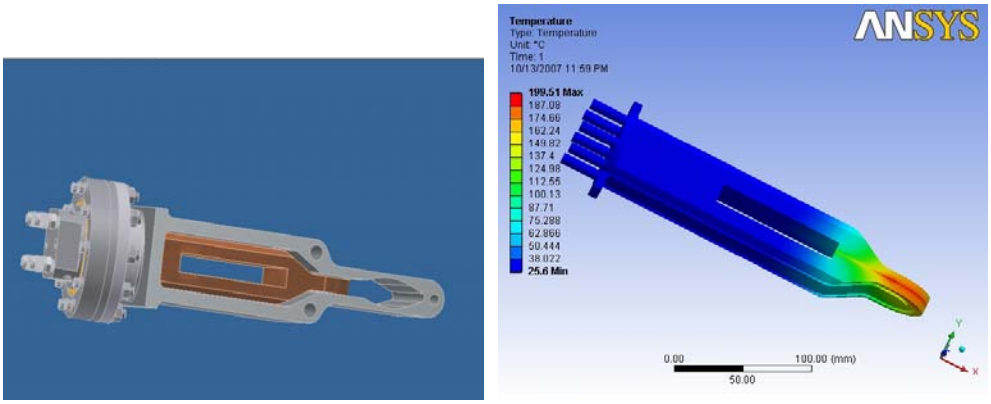

Figure 4.8.7 Crotch absorber. **a**) a 3-D section inside the vacuum chamber. **b**) temperature contours from an ANSYS FE analysis with a peak temperature of 200ºC.

The damping wiggler absorber, shown in Figure 4.8.8a, fits in the ~ 600 mm space between Section 3 and 4 on the outboard side. The upstream end of the absorber is brazed to a flange that mates with the flange of the chamber in Section 3. The downstream end is cantilevered inside a bellows assembly to allow for thermal expansions of the chambers during bakeout. Two water cooling channels are provided on each vertical side of the Glidcop block to absorb power from the outer extents (0.35x2 mrad) of the horizontal DW x-ray fan (5.2

mrad) at a grazing incidence of 6º. The total power intercepted by the two vertical sides is 4 kW, with a peak power density of 22 W/mm^2.

An ANSYS FE thermal analysis of the wiggler absorber predicted a peak surface temperature of 214ºC. The temperature profile, plotted in Figure 4.8.7b, shows high temperatures directly under the beam footprint.

Assuming a water flow of 2 GPM in each of the cooling channels, the average bulk water temperature rise will be 5.5ºC.

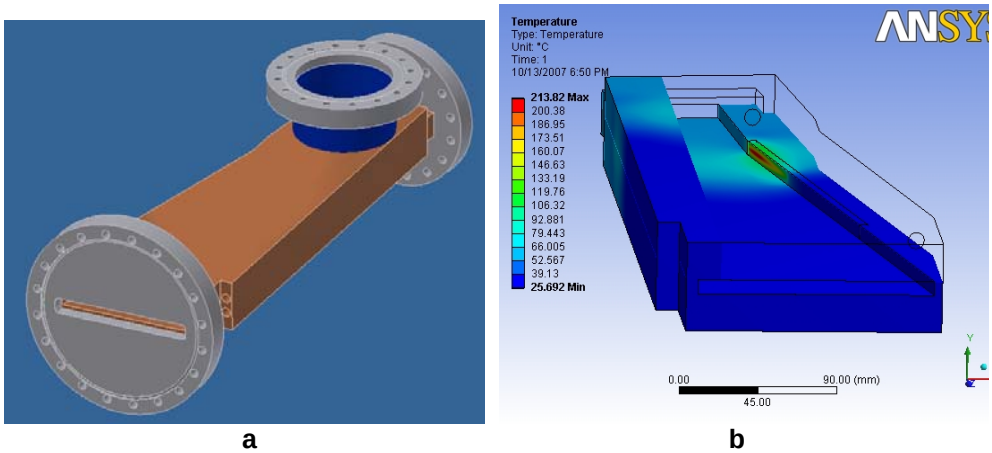

Figure 4.8.8 Damping wiggler absorber. **a**) 3D model showing Glidcop block and flanges. **b**) Temperature contours from an ANSYS FE analysis with a peak temperature of 214ºC.

Another crotch absorber will be used in Section 5 with a slot width that will allow the user-specified width of the dipole radiation fan to exit to the front end. Additionally, counter-flow and flange absorbers (Figure 4.8.9) will be used in Sections 2, 4, and 6 to intercept unused dipole radiation fans.

Figure 4.8.9 Counter-flow and flange absorbers for the storage ring vacuum chambers.

References

[4.8.1] Borland, M. "ID Protection with Fast-Moving Scrapers," OAG-TN-2004-050, November 11, 2004.

[4.8.2] V. Ravindranath, S. Sharma, B. Rusthoven, M Gosz, L. Zhang, and J. Biasci, "Thermal Fatigue Life Prediction of Al-15," proceedings, MEDSI-2006 Workshop, SPring-8, Himeji, Japan, May 24-26, 2006.

4.9 Storage Ring Diagnostics and Instrumentation

4.9.1 Introduction

State-of-the-art advanced diagnostics and instrumentation systems are required for a smooth and rapid commissioning and for productive and successful operation of the NSLS-II storage ring. This section provides a list of the monitored parameters, technical solutions with some alternative variants, and the required specifications to achieve these goals. Table 4.9.1 shows a summary of these various instrumentation components.

Table 4.9.1 Beam Diagnostics and Instrumentation for Storage Ring.

Monitor	Quantity	Function
4-button pick-ups	188	Beam position, dispersion, response matrix, turn-by-turn dynamics
Photon BPMs	1 per installed undulator	Photon beam position
DC current transformer	1	Beam current, lifetime
Emittance monitor	1	Transverse emittances
Fast current transformer	1	Filling pattern, beam current
Transverse feedback system	1	Suppress beam instabilities, tune monitoring
Pinhole camera	1	Transverse beam size, energy spread
Optical ports for visible radiation	2	To provide light for streak camera, FireWire camera, fill pattern and beam current
Streak-camera	1	Bunch length, beam dynamics
FireWire camera	1	Transverse beam characteristics
Fluorescent screen	1	Injection position, profile
RF-drive stripline and amplifier	1	Betatron tune
Beam oscillations monitor	1	Frequency components of longitudinal and transverse beam motion
P-i-n diodes loss monitors	60	Beam loss pattern
Scintillator loss monitors	10	Beam loss
X and Y beam scrapers	2	Machine studies, halo
Diagnostics undulator	1	Energy spread, beam divergence, momentum compaction factor

As a basic policy, whenever possible, we will pursue the utilization of commercial off-the-shelf devices to reduce cost as well to achieve better reliability. Most of the existing diagnostics equipment today already satisfies the basic requirements for NSLS-II and only a few, if any, need further development.

Full utilization of the micron-size electron beam requires sub-micron resolution of the orbit monitoring system, to provide the required position stability. Priority consideration will be given at the earliest stages of design to provide instruments for the detection and remedy of factors that affect beam quality.

4.9.2 Physics Design and Parameters

The following beam parameters will be monitored during regular operations:

- closed orbit (accuracy better than 10% of beam size)
- working point (tune for both planes with 10^{-4} resolution)
- circulating current (0.1% accuracy) and beam lifetime (1% accuracy)
- injection efficiency
- filling pattern (1% of maximal bunch charge)
- emittance for both planes (10% relative accuracy)

- energy spread
- individual bunch length (2 psec resolution)
- position of the photon beam for the insertion devices
- coherent bunch instabilities
- distribution of beam losses around the ring

During beam studies the following parameters will be measured:

- linear optics, including β-functions (1% accuracy) and betatron phase advance ($2\pi \times 10^{-3}$ or better)
- dispersion for both planes (1 mm accuracy)
- chromaticity for both planes (with accuracy 0.1
- coupling (0.05% absolute accuracy)
- momentum compaction (1% relative accuracy)
- beam-based alignment of quadrupoles and sextupoles (30 microns or better)
- synchrotron frequency
- RF system parameters (cavity voltages and phasing)
- vacuum chamber impedances

4.9.3 Intercepting Diagnostics

A fluorescent screen in the injection straight will provide information on the shape and position of the injected beam and will assure proper matching of the beam optics. It is included in the baseline design. The screen will have two positions. The first position will be used to observe the incoming beam from the booster. In the second position, a special hole will allow the injected beam to enter the storage ring, and the beam shape will be observed after one turn. The screen material will be cerium-doped yttrium aluminum garnet (YAG:Ce), which has excellent resolution (about 30 μm) and radiation stability [4.9.1]. The estimated horizontal beam size coming from the booster is $\sigma_x = 360$ μm, and vertical size for 10% coupling is $\sigma_y = 95$ μm. If the spatial resolution of the YAG:Ce flag is found to be inadequate, then optical transition radiation can be used.

To avoid impedance problems, the screen assembly will be designed to ensure a smooth vacuum chamber wall when the screen is fully retracted. Spring-loaded RF-fingers will be used to provide electrical contact in order to avoid trapped modes for the wake fields. A typical screen assembly used at APS is shown in Figure 4.9.1, and the RF fingers are shown in Figure 4.9.2. To use this design we will need only to modify the vacuum chamber aperture to match the NSLS-II geometry.

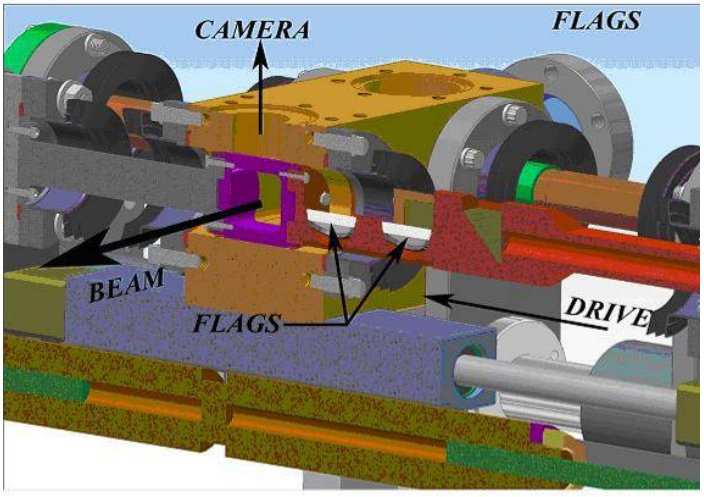

Figure 4.9.1 Design of the screen used for the diagnostic of the electron beam injected into the storage ring at APS. We will modify the vacuum chamber aperture to match the NSLS-II geometry.

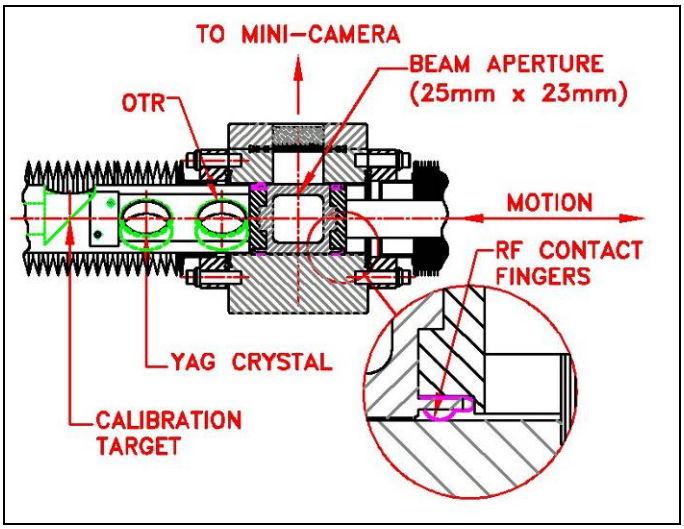

Figure 4.9.2 Spring-loaded RF fingers (see detail) provide smoothness in the vacuum chamber. Electrical contact avoids trapped modes for the wake fields.

4.9.4 Circulating Current

4.9.4.1 Filling Pattern Measurement

To maintain uniform fill and to mitigate dependence of the BPM receivers on the filling pattern, a fast current transformer (FCT), included in the baseline design, will provide electrical signal proportional to the charge of individual bunches. Figure 4.9.3 shows a typical FCT that can be directly mounted on the beam chamber with a ceramic break. FCT-WB-082-20:1 model by Bergoz has 1.75 GHz bandwidth with a 200 psec rise time [4.9.2]. The FCT will be placed over a ceramic break and provided with RF-shielded housing. Fast ADC sampling of the voltage with 500 MHz on the top of each pulse will make charge distribution available to the control system. The information obtained will be used in the top-off algorithm. The signal from the FCT can be used as input for the top-off safety interlock, based on the monitoring of circulating current. Summing found charges for all bunches will provide an alternative means for measuring total beam current.

Figure 4.9.3 Bergoz Fast Current Transformer.

4.9.4.2 Measurement of Circulating Current

A DC current transformer will monitor the stored current in the baseline design. The Bergoz New Parametric Current Transformer (NPCT) is the latest evolution of the Unser transformer [4.9.2], commonly known as DCCT, developed at CERN in 1966 by Klaus B. Unser. It is shown in Figure 4.9.4.

NPCT has large dynamic range and high bandwidth, making it a versatile device for measuring lifetime and injection efficiency. It is insensitive to a synchrotron revolution frequency and bunch fill pattern, with residual modulator ripple being eliminated, thus enabling full bandwidth operation down to a very low current.

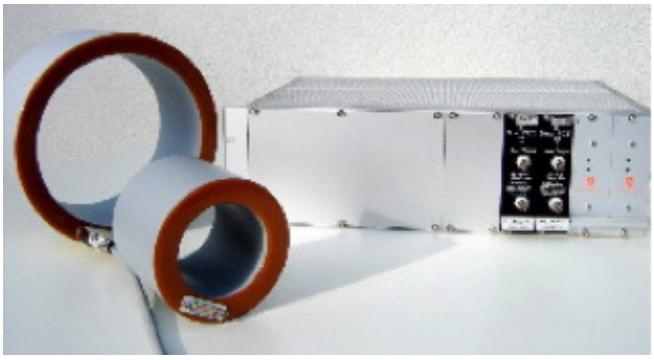

Figure 4.9.4 Bergoz NPCT (New Parametric Current Transformer).

The NPCT-115-C30-HR-H model has a radiation-hardened sensor and four ranges (±20 mA, ±200 mA, ±2 A, ±20 A) with remote control by TTL signals. Wide operational range allows utilization of NPCT starting at commissioning and during regular operations without compromising the requirements for accuracy. Its resolution is better than 1 $\mu A/Hz^{1/2}$. Such a small noise will allow measurement of the expected 60 hours lifetime for 25 mA circulating in one minute with 2% accuracy (assuming a 1 Hz sampling rate). The high bandwidth of the DCCT will allow measurements of the steps in the current after injection, and therefore provide a means of continuously monitoring injection efficiency.

The DCCT will be placed in the dedicated enclosure, providing shielding for RF noise as well as magnetic fields. The microwave absorbers and ferrite will be placed inside in order to suppress wake fields produced by the circulating electron beam.

4.9.5 RF Diagnostics

4.9.5.1 RF Beam Position Monitors

The optics of the NSLS-II storage ring are shown in Figure 4.9.5. In the baseline design there will be six beam position monitors (BPMs) equipped with receivers for each cell. Straights with insertion devices, however, will be provided with two additional instrumented BPMs.

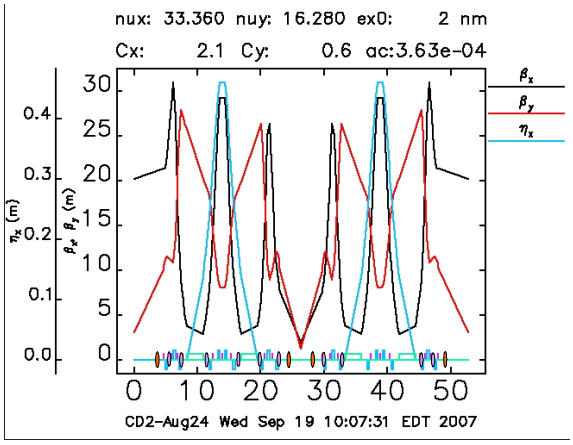

Figure 4.9.5 NSLS-II superperiod. Baseline BPMs are shown as lavender ellipses and user BPMs as orange ellipses.

The high-precision pick-up electrodes will utilize button design and will be diagonally incorporated into the aluminum extrusion vacuum chamber. Figure 4.9.6 shows the cross-section of the basic construction of the four-button pick-up electrodes. An average current of 500 mA circulating in the storage ring is expected to produce –1.1 dBm signal into 50 Ω load at 500 MHz. This estimate is done for a button, shown in Figure 4.9.7, with 5 mm radius and capacitance of 4 pF. The buttons are spaced with a distance to the beam of 20 mm. The scaling parameters for both vertical and horizontal directions are estimated to be around 10 mm for the present geometry; more precise sensitivities will be established during preliminary design.

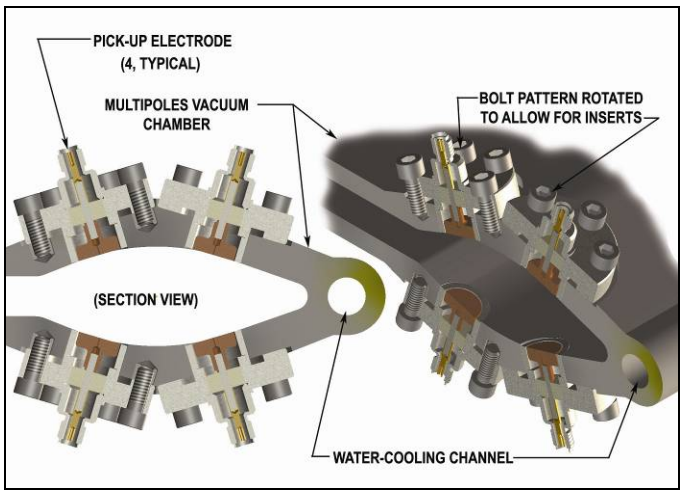

Figure 4.9.6 Four-button, two-plane pick-up electrodes mounted on the vacuum chamber.

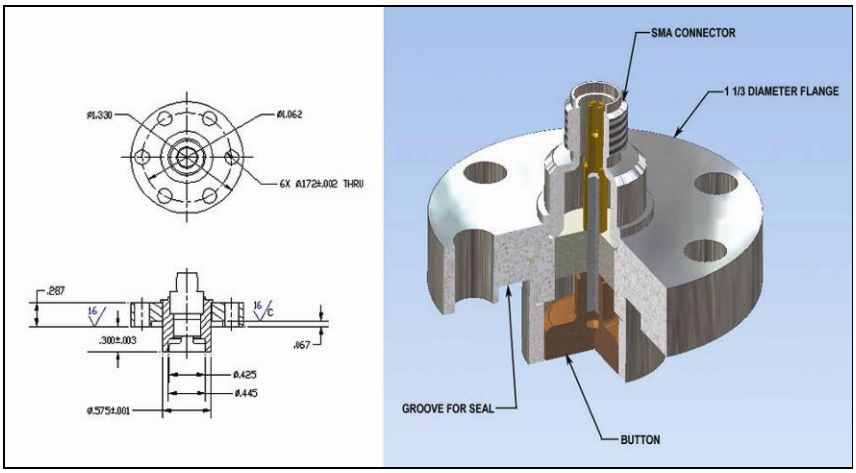

Figure 4.9.7 Design of the BPM button for the storage ring.

Libera Brilliance modules, manufactured by Instrumentation Technologies [4.9.3, 4.9.4] and shown in Figure 4.9.8, can be used to process the signal from the BPM buttons. The RMS uncertainty of the beam position is expected to be below 0.2 μm in 1 kHz bandwidth for the geometry shown. The digital design of the receivers provides the possibility of turn-to-turn beam position measurements with 1 μm accuracy. The chamber with BPM buttons will be mounted on a girder by precisely machined supports, to provide high stability. Small alignment errors, as well as electrical offsets and errors in the BPM system, will be accounted for at the commissioning using beam-based alignment, which will be straightforward, thanks to the individual power supplies.

Figure 4.9.9 Libera Brilliance by Instrumentation Technologies.

The NSLS-II storage ring utilizes very strong sextupoles. This makes it very important to have the orbit of the circulating beam as close as possible to the magnetic centers of the sextupoles. We will rely on highly accurate relative alignment of the sextupoles and quadrupoles on the same girder. In addition, a beam-based alignment procedure will be used for the sextupoles.

To provide the necessary beam stability, not only electrical noise in the BPM electronics should be considered but also mechanical motion of the vacuum chamber. For the most demanding beamlines, the high-stability BPMs will be placed on special, extra-stable posts (Figure 4.9.9), which will minimize positional changes of the vacuum chamber caused by changes in the ambient temperature. Shielded bellows will relieve the tension from the adjacent vacuum ducts. A more detailed description can be found in Section 4.3.2.

Figure 4.9.9 Design of the high-stability BPM support.

4.9.5.2 Tune Monitor

In the baseline design, the vertical and horizontal betatron tunes will be monitored using a network analyzer [4.9.5, 4.9.6]. The analyzer's source will be connected to the excitation striplines through the buffer amplifiers. The signal from the receiver pick-up electrodes will be combined with hybrids to produce vertical or horizontal signals, which will be down-converted below the revolution frequency and fed to the input of the network analyzer (Figure 4.9.10). Such an approach allows utilization of the maximal driving strength of the striplines and makes measurement of the tunes less sensitive to changes in the revolution frequency.

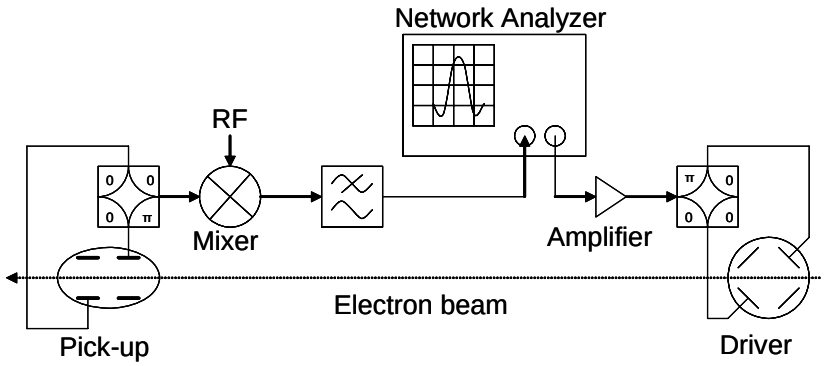

Figure 4.9.10 Layout of the tune measurement system.

As a back-up, we can use the turn-by-turn data provided by the orbit monitoring system with electron beam being excited by the pingers located in the injection straight. Another solution that can be implemented after ring commissioning is utilizing the phase-locked loop.

The tune monitor should provide betatron frequency resolution of 10^{-4} (or better) to obtain 1% accuracy in the β-functions, with up to five-fold difference in the β-functions for different planes with 0.05 allowable tune change. High precision of the tune measurements will facilitate beam-based alignment of the sextupoles, as well. Such parameters need to be reached even with chromaticities as high as 5.

4.9.5.3 Beam Oscillations Monitor

The signal from a dedicated set of pick-up electrodes will be connected to an RF spectrum analyzer (Figure 4.9.11). The sidebands observed can be used to analyze electron beam motion. Summing the signal from opposite electrodes helps to eliminate components with transverse oscillations, while maintaining the signal with phase motion of the electron bunches, which allows measurement of the synchrotron frequency. The difference signal will be used to observe transverse oscillations of the electron beam. This diagnostic instrument is included in the baseline design due to its usefulness during commissioning.

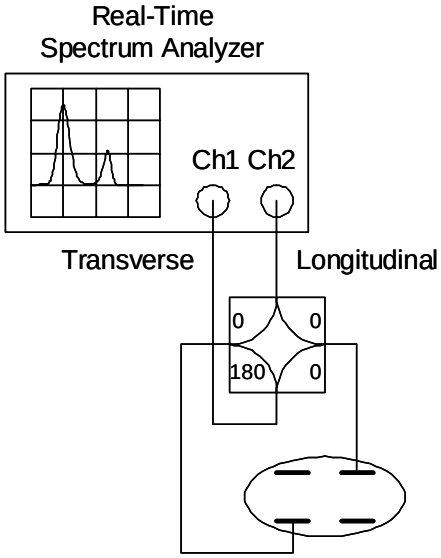

Figure 4.9.11 System for the observation of beam oscillations.

4.9.5.4 Transverse Feedback System

The resistive wall wake can destabilize the electron beam in the storage ring. Increasing the chromaticity may not be sufficient, due to limitations on sextupole strength resulting from loss of the dynamic aperture required for beam lifetime and injection. The required stability can be provided by a digital bunch-by-bunch transverse feedback system [4.9.7, 4.9.8]. A broadband signal measuring the position of the individual bunches will be provided by the button-shaped pick-up electrodes. It will be sampled with a fast ADC (sampling rate 500 MHz). A digital filter will calculate the desired correction signal, which is generated by a DAC. The correction kicks are fed through a broadband amplifier and drive the electron beam using the second stripline. We are considering using a Libera Bunch-by-bunch system as an integrated unit, which provides all necessary analog-to-digital and digital-to-analog conversion with FPGA processing [4.9.8] (Table 4.9.2). In the baseline design the transverse feedback will be employed only for the vertical plane. However, the design can be easily expanded for the horizontal plane by the addition of another processing module.

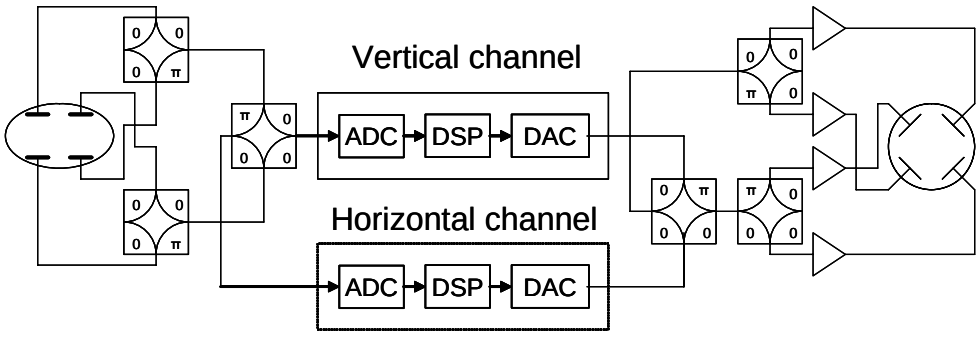

Figure 4.9.10 Conceptual layout of the transverse feedback system.

Table 4.9.2 Parameters of the transverse feedback.

Feedback parameters	vertical	horizontal
Measurement range	±0.15 mm	±1.5 mm
Resolution	0.3 micron	0.5 micron
Kick strength per turn	0.5 microrad	0.3 microrad
Minimal damping time τ_{min}	90 microsec	2.6 msec
Added noise for $\tau=\tau_{min}$	0.01 microns	0.09 microns

The length of the 50 Ω striplines will be 15 cm (one-quarter of the RF wavelength). The striplines will be installed in the drift space on the arc where β_x=4.6 m and β_y=19.1 m. 100 W amplifiers will produce and electric field of 5 kV/m on the 38 mm vertical gap. Together with the magnetic field, the stripline will produce a deflection angle of 0.5 microradians for 3.0 GeV electron beam.

4.9.6 Synchrotron Radiation Diagnostics

4.9.6.1 Overview

This section describes diagnostics for the NSLS-II storage ring that utilize visible and x-ray synchrotron radiation generated in a bending magnet and an x-ray undulator. Table 4.9.3 shows the types and quantities of diagnostics for the storage ring.

Table 4.9.3 Complement of the Optical Diagnostics for the NSLS-II Storage Ring.

Monitor type	Quantity	Function	Range	Resolution	Bandwidth
Emittance monitor	1	Horizontal emittance Vertical emittance	0.5-2.5 nm-rad 8 pm-rad	5 pm-rad 1 pm-rad	100 Hz
Streak-camera	1	Bunch length	10 – 50 ps	2 ps	8 Hz
Pinhole camera	1	Beam size Energy spread	10x30 microns 0.2 – 2%	4 microns 0.01%	30 Hz
Photon BPM	1 per beamline	Position of ID radiation	10 mm	0.001 mm	2 kHz
Diagnostics undulator with pinhole camera	1	Horizontal emittance energy spread momentum compaction factor	0.5 – 2.5 nm-rad 0.2 – 2% 10^{-4}		
FireWire camera	1	Beam profile		640x480	120 fps

4.9.6.2 Emittance monitor

For measuring the ultra low vertical emittance of the storage ring, we included in the baseline design the direct imaging of the electron beam with two zone plates. This method was developed at KEK [4.9.9] for measuring ultra small beam sizes. A double crystal monochromator selects the observation wavelength, λ. The first zone plate focuses the monochromatic beam to small spot, while the second zone plate magnifies the image, making it suitable to observe by X-ray CCD camera. The optical setup is shown in Figure 4.9.11.

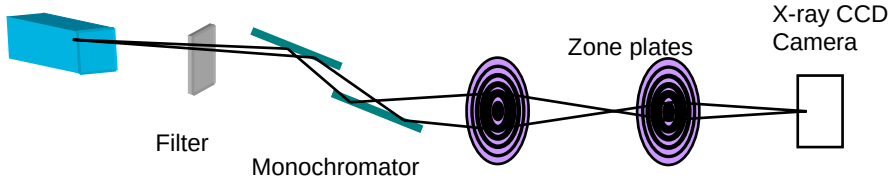

Figure 4.9.11 Layout of emittance monitor utilizing two zone plates.

4.9.6.3 Bunch Length Measurement

A double-sweep streak-camera Optronis model SC-10 [4.9.10], shown in Figure 4.9.12, will be used to measure the longitudinal beam dynamics. Its versatility and high sensitivity make it an excellent choice for monitoring the bunch length with high resolution and studying beam instabilities. The streak camera will be equipped with IOV-10 input optics. The bialkali photocathode with 8 mm × 2 mm area provides low dark noise (below 50 $e^-/cm^2/s$). The parameters of the streak camera are shown in Table 4.9.3. The synchroscan feature provides low-phase jitter for synchronous summing of signals and tracking phase dynamics. The dual sweep is also available. The readout will be performed with a fiber optically coupled CCD camera (ANIMA-PX/25).

The OptoControl software will enable us to access all streak camera parameters and to control the camera operation. A 100 MHz Ethernet (TCP/IP) interface is integrated with the control system. For additional image analysis, the OptoAnalyse software is available. This program allows the use of sophisticated image acquisition algorithms and provides various tools for temporal or spatial analysis. The photon counting combined with drift and jitter correction makes possible long-term measurements with high sensitivity and high temporal resolution.

Table 4.9.3 Optronis SC-10 Streak Camera Parameters.

Spectral response characteristics [nm]	350 to 700
Synchroscan frequency (factory setting) [MHz]	40 – 250
Temporal resolution (FWMH) [ps]	2
Sweep range	300 ps to 4 ns
Camera resolution [pixels]	1360x1024
Frame rate [Hz]	8
Dynamic range [bit]	12

The streak camera will be shared with the booster. An optical beamline from the booster will be used to transport a beam of synchrotron radiation from the booster bending magnet to the streak camera. An alternative solution is to use C5680 synchroscan streak camera by Hamamatsu.

Figure 4.9.12 View of the SC streak camera family.

4.9.6.4 Photon Beam Position Monitors

Photon beam position monitors (PhBPMs) manufactured by FMB-Berlin (shown in Figure 4.9.13) are being considered for monitoring radiation from the insertion devices [4.9.11]; the blades, of course, will be designed and optimized to suit the requirements of NSLS-II. The PhBPMs are based on a development by Dr. Karsten Holldack at BESSY. The information obtained on the position of the photon beam will be incorporated into the orbit feedback system to provide the beam stability required for user applications. In the baseline design we have one PhBPM per beamline. The PhBPM assembly will be mounted on a stable post and its location (elevation and transverse position) will be adjusted with 2D translation stages (Figure 4.9.14). Similar devices at APS enable pointing stability of the photon beam with peak-to-peak drift of less than 2 μrad over six days [4.9.12].

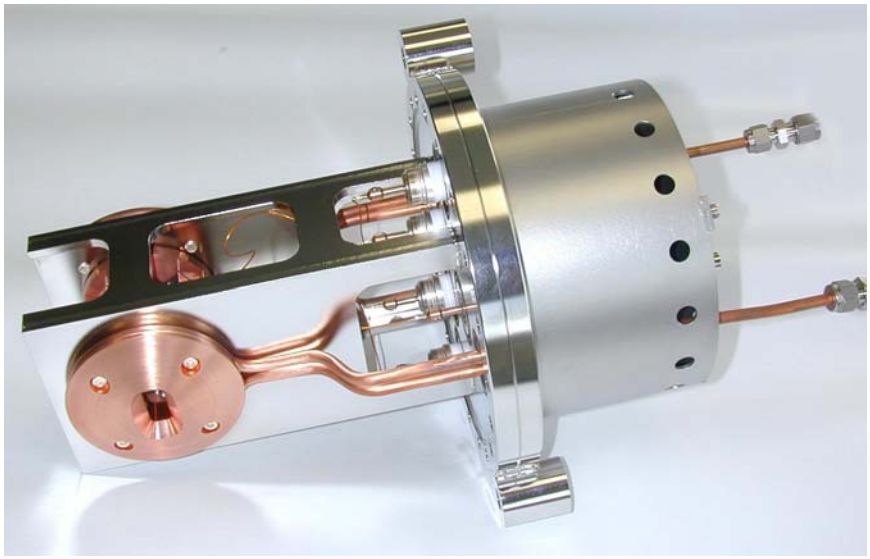

Figure 4.9.13 Photon beam position monitor.

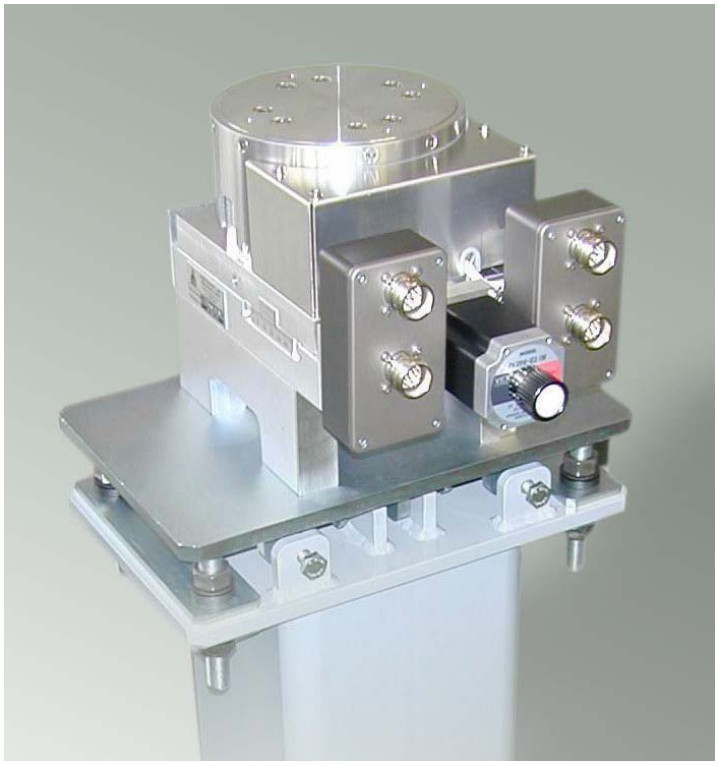

Figure 4.9.14 Photon beam position monitor on the support column with motorized stage.

4.9.6.5 Diagnostics with Visible Synchrotron Radiation

An IEEE1394 camera will be used to observe the visible radiation from the electron beam. Such an approach eliminates the need for a frame-grabber and makes display of the beam on the control computer straightforward. The camera has an external trigger capability and exposure control from 10 μsec to 5 sec.

Position-sensitive photodiodes which provide signal based on the location of the center of gravity of the optical beam can be incorporated into the orbit feedback system to monitor beam stability for IR users, as well as results of image processing. The model S2044 (the smallest object in Figure 4.9.15) has 0.6 μm sensitivity and 0.3 μsec rise time.

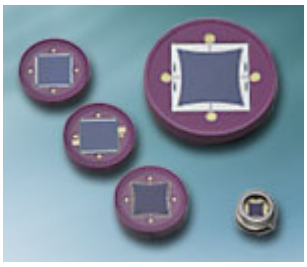

Figure 4.9.15 Position-sensitive diodes by Hamamatsu.

4.9.6.6 Diagnostics Undulator

The diagnostics undulator will allow independent measurement of the energy spread and horizontal emittance. The momentum compaction factor can be also measured. We plan to utilize one of the user beamline undulators in a 5m straight; therefore, this tool is not included in the baseline design.. This beamline will be equipped with an additional high-resolution fluorescent screen and a retractable pinhole (Figure 4.9.16). Use of the radiation from the undulator for diagnostic purposes will be restricted to periods when it is not needed by the users.

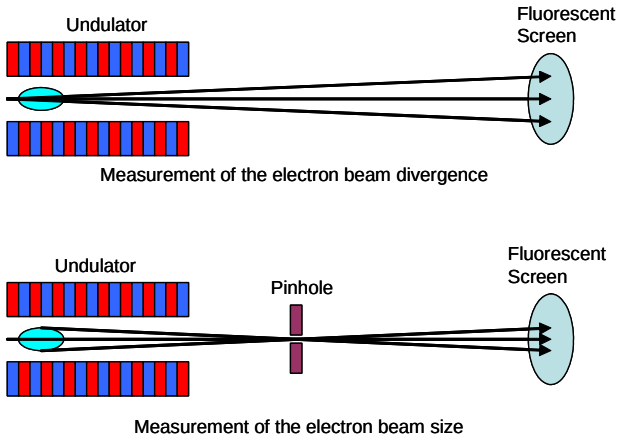

Figure 4.9.16 Beam diagnostics with undulator radiation.

The β-functions in the straight are $\beta_{xmin} = 2.5$ m and $\beta_{ymin} = 1.2$ m. The U20 undulator that we propose to use has a 20 mm period and 3 m length. To measure the divergence of the electron beam, the transverse profile of the undulator radiation will be monitored. To increase system resolution, small undulator K values will be utilized. These will also help to minimize the power from higher harmonics and avoid distorting the power profile. For $K = 0.3$, the power density of the 3rd harmonic is two orders of magnitude below the power density of the main harmonic. For this value of K, the fundamental wavelength of the undulator radiation will be 0.29 nm and the divergence due to a diffraction will be $\sigma'_{ph} = \sqrt{\lambda / L} = 9.8\,\mu\text{rad}$, which compares favorably with the horizontal divergence of the electron beam: $\sigma'_e = \sqrt{\varepsilon_x / \beta_x} = 14.1\,\mu\text{rad}$ for 0.5 nm-rad emittance.

Inserting a pinhole, which can be realized as a slit, will enable measurement of the horizontal beam size. Knowing the divergence and beam size will enable us to directly measure the beam emittance, independent of the β-function.

Analysis of the width of the undulator spectrum provides information on the energy spread of the electron beam. It is also possible to measure the momentum compaction factor by observing the shift of the undulator spectrum with revolution frequency [4.9.12].

4.9.7 Other Diagnostics

4.9.7.1 Beam Loss Monitors

NSLS-II will utilize a distributed beam loss monitoring system based on p-i-n diodes, which are commercially available from Bergoz [4.9.2] (Figure 4.9.17). Two beam loss monitors per cell will be used for monitoring the spatial distribution of beam losses.

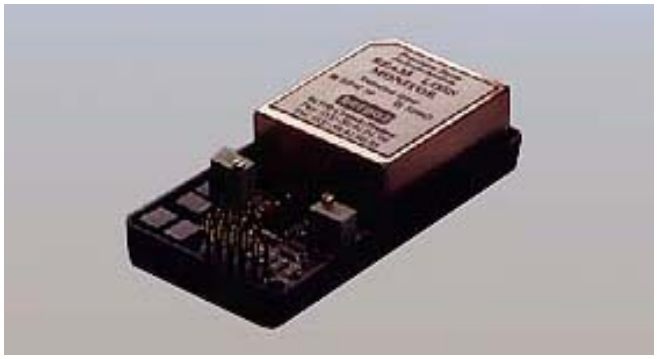

Figure 4.9.17 Beam loss monitor by Bergoz.

The loss monitors have a pulse output (one pulse per lost particle) and are insensitive to the synchrotron radiation photons. The monitors are small and can be easily relocated to the region of interest. CosyLab has developed interfaces for easy integration with the control system [4.9.13].

For the temporal distribution of the lost particles (on the scale of one turn) we plan to use ten scintillation detectors (Figure 4.9.18). They can be also be used for monitoring the losses of injected electrons near the injection and RF straights.

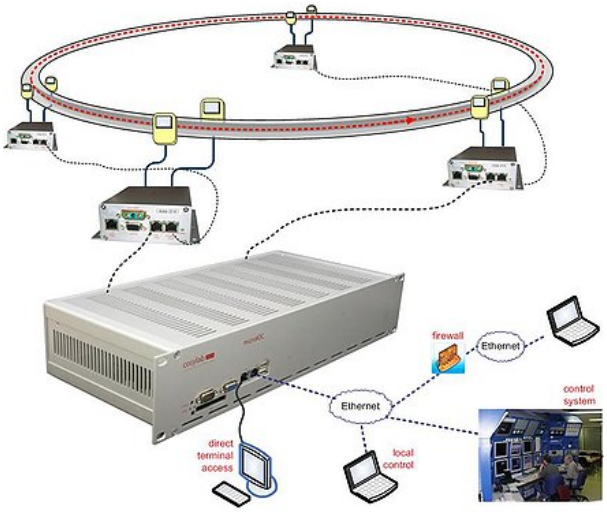

Figure 4.9.18 MicroIOC with signal conditioners for Bergoz beam loss monitors.

4.9.7.2 Scrapers

Two pairs of two-plane adjustable-position scrapers will be installed on the ring to be used both as protective devices as well as diagnostic instruments for accelerator studies. More details are described in Section 4.7. One set of scrapers (horizontal and vertical) will be installed in the dispersive section to measure the energy distribution of the electron beam. Another set will be installed in a straight section with zero dispersion in order to have information on the transverse size of the electron beam, and to eliminate possible beam halos capable of affecting the insertion devices.

4.9.7.3 High-Level Accelerator Modeling

Extracting data on the storage ring lattice from the experimental data [4.9.14] requires high-level accelerator modeling, described in the control system section. High-level accelerator modeling will also be used in the development of a real-time orbit feedback system and for coupling correction. Such high-level applications will necessitate a storage ring simulator for the offline testing and debugging of the software being developed.

A procedure was developed and experimentally verified for measuring accelerating voltage in the RF cavity [4.9.15]. The method is based on the observation of a phase shift between the electron beam and electrical field in the cavity when amplitude of the field varies. This procedure also makes it possible to measure relative phases between multiple cavities installed on the storage ring.

References

[4.9.1] E.D. Johnson, W.S. Graves, and K.E. Robinson, "Periscope Pop-In Beam Monitor," Proc. of Beam Instrumentation Workshop 1998, AIP Conf. Proc. 451, pp. 479–484.

[4.9.2] http://www.bergoz.com

[4.9.3] R. Ursic et al., "Holy Trinity of the Instrumentation Development," Proc. of the 11th Beam Instrumentation Workshop, Knoxville 2004.

[4.9.4] U. Mavric, "Innovative RF Design Unites Benefits of Multiplexed and Multichannel System," Proc. of the 11th Beam Instrumentation Workshop, Knoxville, 2004.

[4.9.5] A.S. Fisher, "Instrumentation and Diagnostics for PEP-II," Proc. Beam Instrumentation Workshop 1998, AIP Conf. Proc. 451, pp. 95–109.

[4.9.6] A. S. Fisher, M. Petree, U. Wienands, S. Allison, M. Laznovsky, M. Seeman, and J. Robin, "Upgrades to PEP-II Tune Measurements," Proc. of Beam Instrumentation Workshop 2002, AIP Conf. Proc. 648, pp. 267–274.

[4.9.7] M. Dehler, R. Kramert, P. Pollet, and T. Schilcher, "Commissioning Results of the Multi Bunch Feedback System at SLS," Proc. of EPAC 2004, pp. 2508–2510.

[4.9.8] J.M. Koch, G. Naylor, E. Plouviez, and F. Epaud, "Beam Diagnostic Features of the ESRF Multibunch Feedback," Proc. DIPAC 2007.

[4.9.9] K. Iida, et al., "Measurement of an Electron-Beam Size with a Beam Profile Monitor Using Fresnel Zone Plates," Nucl. Instr. and Meth. A506 (2003), pp. 41-49.

[4.9.10] http://www.optronis.com

[4.9.11] G. Decker and O. Singh, "Beam Stability at the Advanced Photon Source," Proc. of PAC 2005, pp. 3268–3270.

[4.9.12] B. Yang, M. Borland, and L. Emery, "High Accuracy Momentum Compaction Measurement for the APS Storage Ring with Undulator Radiation," CP546, Beam Instrumentation Workshop 2000, American Institute of Physics, pp. 235–241.

[4.9.13] http://www.CosyLab.com

[4.9.14] J.A. Safranek, "Beam-based Accelerator Modeling and Control," Proc. of Beam Instrumentation Workshop 2000, AIP Conf. Proc. 546, pp. 23–5.

[4.9.15] I. Pinayev, Characterization of the RF System of NSLS X-ray Ring, Proceedings of PAC'07.